UNIVERSIDADE FEDERAL DE MINAS GERAIS
Escola de Engenharia
Programa de Pós-Graduação em Engenharia Elétrica

Lucas Saraiva Teixeira

Modelling Lithium-Ion Battery Degradation for Second Life Stationary Applications

Belo Horizonte

2024

Lucas Saraiva Teixeira

Modelling Lithium-Ion Battery Degradation for Second Life Stationary Applications

Dissertation presented to the Graduate Program in Electrical Engineering (PPGEE) of the School of Engineering of the Federal University of Minas Gerais (UFMG) in partial fulfillment of the requirements for the Master's Degree in Electrical Engineering.

Orientador: Prof. Dr. Sidelmo Magalhães Silva

Belo Horizonte

2024

UNIVERSIDADE FEDERAL DE MINAS GERAIS
ESCOLA DE ENGENHARIA
PÓS-GRADUAÇÃO EM ENGENHARIA ELÉTRICA

"Modeling Lithium-ion Battery Degradation For Second Life Stationary Applications"

Lucas Saraiva Teixeira

Dissertação de Mestrado submetida à Banca Examinadora designada pelo Colegiado do Programa de Pós-Graduação em Engenharia Elétrica da Escola de Engenharia da Universidade Federal de Minas Gerais, como requisito para obtenção do grau de Mestre em Engenharia Elétrica.

Aprovada em 14 de agosto de 2024.

Por:

Prof. Dr. Sidelmo Magalhães Silva
DEE (UFMG) - Orientador

Prof. Dr. Igor Amariz Pires
DELT (UFMG)

Prof. Dr. Thales Alexandre Carvalho Maia
DEE (UFMG)

Profa. Dr. Wadaed Uturbey da Costa
DEE (UFMG)

Referência: Processo nº 23072.244866/2024-68   SEI nº 3454485

Agradecimentos

Ao meu orientador Prof. Sidelmo Magalhães da Silva, por ter me guiado nesse momento de aprendizado e incerteza.

Ao time do Laboratório Tesla pela troca de experiência e conhecimento. Pelo suporte, privacidade e o café que me deu foco, paz, e o espaço para eu pensar e crescer.

Ao CAPES, UFMG, e PPGEE pelo suporte, estrutura, oportunidade e recursos necessários para conclusão do trabalho.

Aos meus pais, Angélica e Carlos Renato, e irmã, Ana Luísa, pelo apoio e estabilidade que me possibilitaram focar, enfrentar e vencer qualquer desafio.

Ao meu tio, José Cléber. Sempre um grande companheiro, conselheiro e inspiração. Uma referência importante no meu desenvolvimento intelectual desde o começo.

Muito obrigado.

[T]ell anyone from before the long twentieth century about the wealth, productivity, technology, and sophisticated productive organizations of the world today, and their likely response [...] would be that with such enormous power and wealth in our collective hands we must have built a utopia.

J. Bradford DeLong, Slouching Towards Utopia (2022)

Abstract

Fast improvements in lithium-ion battery technology have accelerated the transition towards electrification in the transportation sector. As electric vehicles grow as a share of the market, precautions should be made with regards to the proper handling and disposal of the battery cells as they age. After around 8 to 10 years – or about 100,000 km – of use, it is typically recommended that the EV battery storage system be replaced. Though these discarded batteries are no longer adequate for continued vehicular use (which has high power and energy storage demands), there is potential for use in other less intensive application; particularly grid-supporting stationary applications.

This dissertation discusses these repurposed batteries, known as "Second-Life Batteries"; in particular, this works focuses on the battery degradation modelling. Being able to model, predict, and estimate the internal capacity loss and impedance gain for a battery is important for control and forecasting purposes; even more so in second-life applications due to the additional safety considerations necessary when handling an aged cell and the eventual transition from linear to exponential rate of capacity loss (aging knee-point). Given these requirements, physics-based models are the most accurate and robust kind of battery model. When properly tuned, they have the potential of simulating long-term degradation – including forecasting the aging knee-point – which a lot of precision.

This dissertation serves as an introduction of physics-based models for the purposes of Electric Vehicle simulation and Second-Life simulation. It includes an accessible explanation and literature review of the logic behind the physics-based mathematical models. In addition to that, this work showcases an illustrative example of an Electric Vehicle simulation (implemented in Simulink) using a physics-based battery model by way of PyBaMM – an open-source battery simulation library for Python.

Keywords: Second-Life Batteries, Lithium-ion Batteries, Degradation modelling, Electric-Vehicles, PyBaMM.

Resumo

Rápidos avanços na tecnologia de baterias de íons de lítio têm acelerado a transição para a eletrificação no setor de transporte. À medida que os veículos elétricos crescem como uma parcela do mercado, devem ser tomadas precauções em relação ao manuseio e descarte adequados das células da bateria à medida que envelhecem. Após cerca de 8 a 10 anos – ou cerca de 100.000 km – de uso, é tipicamente recomendado que o sistema de armazenamento da bateria do veículo elétrico seja substituído. Embora essas baterias descartadas não sejam mais adequadas para continuar em uso veícular (que têm altas demandas de potência e armazenamento de energia), há potencial para uso em outras aplicações menos intensivas; particularmente em aplicações estacionárias de suporte à rede.

Esta dissertação discute essas baterias reaproveitadas, conhecidas como "Baterias de Segunda Vida"; em particular, este trabalho foca na modelagem da degradação da bateria. Ser capaz de modelar, simular e estimar a perda de capacidade interna e o ganho de impedância de uma bateria é importante para fins de controle e previsão; ainda mais em aplicações de segunda vida devido às considerações adicionais de segurança necessárias ao manusear uma célula envelhecida e a eventual transição de uma taxa linear para exponencial de perda de capacidade (ponto *knee-point* de envelhecimento). Dadas essas exigências, modelos baseados em física são o tipo mais preciso e robusto de modelo de bateria. Quando devidamente ajustados, eles têm o potencial de simular a degradação a longo prazo – incluindo a previsão do ponto de *knee-point* de envelhecimento – com muita precisão.

Esta dissertação serve como uma introdução aos modelos baseados em física para fins de simulação de Veículos Elétricos e simulação de Segunda Vida. Inclui uma explicação acessível e uma revisão da literatura sobre a lógica por trás dos modelos matemáticos baseados em física. Além disso, este trabalho apresenta um exemplo ilustrativo de uma simulação de Veículo Elétrico (implementada em Simulink) utilizando um modelo de bateria baseado em física por meio do PyBaMM – uma biblioteca de simulação de baterias de código aberto para Python.

Palavras-chave: Segunda Vida das Baterias, Baterias de íons de lítio, Modelagem de degradação, Veículos Elétricos, PyBaMM.

List of Figures

List of Tables

Contents

1 Introduction

1.1 Context and Relevance

As the world commits to transitioning away from carbon generating fossil fuels towards a greener more sustainable energy mix, each sector is urged to decarbonize. Transportation is one of the biggest, most polluting sectors. It accounts for 21% of the total greenhouse gases emission, 75% of which originates from road vehicles (RITCHIE, 2020). Replacing such a huge component of the energy sector with clean alternatives represents a massive challenge.

As late as 2007, the most viable path towards a net-zero transportation seemed to be extensive use of biofuels such as ethanol (ROBERTS; LASHOF, 2023). This would be a hugely inefficient solution that would require a large percentage of all the available land to power a full biofuel fleet. However, thanks to significant technological advancements in batteries and renewable energy sources (particularly solar), electrification has emerged as the best, cheapest, most plausible way to decarbonize a whole range of industries – including transportation.

The advancements in battery technology which have enabled electric vehicles (EVs) to become a more viable and competitive alternative are the significant increases in battery energy density and lower prices. Energy densities have nearly tripled between 2010 and 2020 (FIELD, 2020) while prices have fallen an average of 14% per year between 2007 and 2014 (NYKVIST; NILSSON, 2015), going from US$$1000/kWh$ in 2008 to around US$$150/kWh$ today (REID; JULVE, 2016; BLOOMBERGNEF, 2022).

As the issues of driving-range and price are addressed, Electric Vehicle become a growing share of the market. In 2022, 23% of new vehicle registration in Europe were electric (KANE, 2023b). In China, a middle-income country and the biggest car market in the world, EVs and Hybrids have already captured significant market-share and are still quickly growing: going from 15% of new sales in 2021 to 30% in 2022 – a dramatic increase (KANE, 2023a; PONTES, 2023). These trends are expected to continue as the industry continues to grow causing more research to be directed towards this area and economy-of-scale benefits start to take effect. The World Economic Forum predicted a 14-fold increase in the demand for batteries between 2018 and 2030; this sharp rise is led primarily by the transportation sector, which is expected to account

for 88% of that demand (WEF, 2019). Another study attempts to forecast capacity demand by 2040 for three different scenarios, it finds an yearly EV capacity demand of 6700 GWh per year in the most optimistic scenario, and 930 GWh per year in the most pessimistic (MAISEL et al., 2023).

In addition to these trends, many countries and auto-makers have made commitments to support EVs and phase-out internal combustion engine vehicles (ICEVs).

- Multiple auto-makers have made vows to invest in the electrification of their products. Some, like Volkswagen, expect EV sales to represent up to 60% of all new vehicles by 2030 (WHITE, 2021).

- California, the richest and most populous of the U.S. states, aims to ban the commercializing of greenhouse gases (GHG) emitting vehicles by 2035. More than a dozen other states typically follow California's lead when setting their own auto emissions standards (DAVENPORT; FRIEDMAN; PLUMER, 2022).

- In August 2022, the U.S. Government signed the "Inflation Reduction Act" into law, a major piece of climate legislation which awards big investments towards green infrastructure with the aim of achieving net-zero by 2050. This legislation awards billions in subsidies and tax benefits towards the EV sector and all stages of battery development: manufacturing, recycling and repurposing (WHITE HOUSE, 2023; BADLAM et al., 2022).

- The European Union (E.U.) has also introduced a plan to ban the sale of new gasoline cars by 2035 (EDDY, 2023).

As technology trends and regulatory pressures continue and intensify, the transition away from ICEVs and towards EVs should continue to accelerate. Electric vehicles, however, have their own environmental and waste issues which need to be addressed, particularly with regards to batteries. Due to degradation, the lithium batteries have a limited useful life; once a battery reaches 80% of its original capacity, it is no longer deemed adequate for vehicular use and should, ideally, be replaced (USABC; HUNT, 1996; MARTINEZ-LASERNA; GANDIAGA, et al., 2018; CASALS; GARCÍA; CANAL, 2019). The aged cells that are removed from electric vehicles contain traces of rare-earth metals and chemicals which can be both valuable and toxic to humans and nature. A proper disposal system should be able to safely isolate and dispose

off the dangerous materials while recycling the useful metals and returning them back to the manufacturing process (DIEKMANN; KWADE, 2018; HARPER et al., 2019).

Before that, however, most batteries at their first-life end-of-life (FL-EOL) can still be repurposed and reused in other less demanding stationary applications like providing some types of ancillary services to the grid like peak-shaving, load-shifting, supporting renewable generation, among others (HU; DENG, et al., 2022). These batteries which see use after their first End-of-Life are known as "**Second-Life Batteries**" (CANALS CASALS; AMANTE GARCÍA; GONZÁLEZ BENÍTEZ, 2016; LACAP; PARK; BESLOW, 2021), they could be a promising, cheap and sustainable alternative for a lot of storage use-cases – all the while also helping to reduce the cost of the first-life batteries in EVs themselves (SATHRE et al., 2015).

1.2   Motivation and Objectives

In anticipation of the rise in Electric Vehicles and the subsequent wave of discarded batteries, it is important to study Second-Life Batteries and its challenges, limitations, economic viability, safety risks, and sustainability. This work is part of a larger project which plans to eventually create a SLB system case-study within the Oasis-UFMG microgrid using the batteries from a not yet operational fleet of electric buses which will service the university campus.

This end-goal is still a long time away. For now, this current work has a more narrow focus on the issue of battery degradation. The plan for this work is to create a MATLAB/Simulink model for the electric bus which accounts for battery degradation. Using this e-bus model and the drive cycle from the planned bus route described and measured in (ALCANTARA, 2022), the first life of the battery will be simulated. Then, using the resulting battery degradation state from the battery model, a second-life battery simulation is to be run. Eventually, future work will use the simulation techniques presented within this thesis to conduct a more sophisticated lifelong techno-economic assessment which takes into account the battery's first and second life.

In summary, this work focuses on:

- Lithium-ion battery degradation

- Electric vehicle simulation

- Microgrid applications of Energy Storage Systems

1.3   Structure of Dissertation

Chapter 2 presents a literature review. It is a general overview on a wide range of topics related to the question of Second-Life Batteries and should be thought of as a guide for the rest of the larger SLB project.

Chapter 3 is an overview of physics-based battery models. This is an approach which is derived from electrochemistry, it represents the battery by modelling the internal physical and chemical state of each battery cell. This family of models is the most complex and computationally expensive, it is also the most accurate depiction of li-ion batteries and has a lot of potential particularly for Rest of Useful Life estimation in Second-Life applications.

Chapter 4 describes the battery simulation experiment set-up used to run the first-life electric vehicle degradation experiment. It details how the EV Simulink model was built, the program used to run the physics-based battery simulation, and how these two separate simulation software programs were combined.

Chapter 5 discusses the results obtained from this simulation, both the first and second life degradation trajectories.

Chapter 6 concludes the dissertation. It looks back on the work as a whole and discusses its successes and limitations of this approach. It also looks towards the future and suggests future projects which build on the results obtained here.

2 State of the Art

This chapter provides a generalized overview on a range of topics relevant to the questions of stationary battery second-life and long term battery degradation simulation.

Section 2.1 discusses the mathematical modelling of an electric vehicle power-train. This shall serve as the basis for the EV Simulink model in the First-Life battery simulation later on.

Section 2.2 speaks on the topic lithium-ion batteries. Section 2.2.1 serves as a short introduction to the concept, Section 2.2.2 discusses the different types of battery cell models, and Section 2.2.3 discusses the main causes of li-ion battery degradation and some of the ways in which it can be modelled.

Lastly, Section 2.3 discusses issues related to Second-Life Batteries (SLB) more specifically. From the logistics and economic viability of SLBs (Section 2.3.1) to the diagnostic process of an aged cell (Section 2.3.2).

2.1   Modelling an Electric Vehicle Powertrain

When studying a complicated machine, it is often useful to break the problem down into its component parts and systems. In the case of a vehicle – be it electric or combustion driven – the single most important component system is the *powertrain*, which is tasked with converting stored chemical energy into kinetic energy and delivering it to the propulsion system (ALCANTARA, 2022). In the case of a Battery Electric Vehicle, the powertrain can be further disassembled into four main components. These are listed bellow, ordered in accordance with the direction of power flow during acceleration, from source to destination:

- Battery Storage System

- Electronic Power Converter (Inverter)

- Electric Motor

- Propulsion System

The powertrain can thus be represented as a chain of components, as illustrated in Figure 2.1 (MIRI; FOTOUHI; EWIN, 2021). During acceleration, when power is flowing from the battery to the transmission system, each component can be thought of as providing something to the component which immediately proceeds it. The battery pack provides current to the inverter, which powers the electric motor, which in turns delivers torque to the transmission systems (ZHOU, 2007); this hierarchy is shown in Figure 2.1. The present section will focus on the final three components from the preceding list. The battery storage module – the singular most important component within an Electric Vehicle, making up as much as 40% of the total cost of the whole vehicle (LUTSEY; NICHOLAS, 2019) – will be discussed in more detail in Section 2.2 and in Chapter 3. For now, the battery storage system is to be treated as a black box.
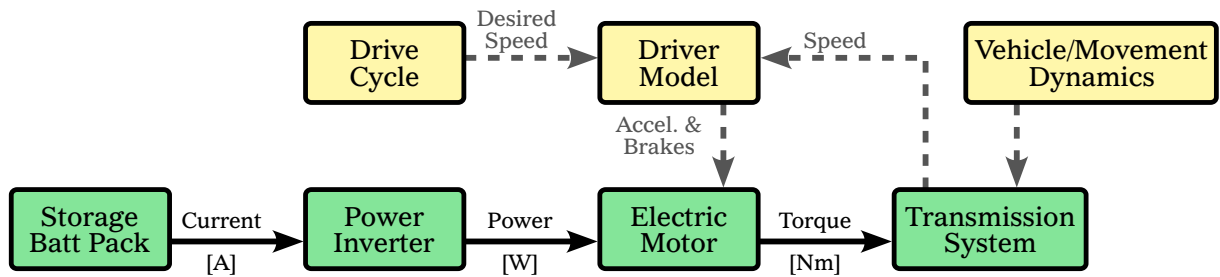
Figure 2.1 – Simplified Battery Electric Vehicle powertrain. Adapted from (MIRI; FOTOUHI; EWIN, 2021).

2.1.1 Propulsion System

The propulsion system is the one ultimately responsible for the movement of the vehicle. The acceleration is described by (2.1), where M represents the overall mass of the vehicle, k_m represents the rotational inertial factor (typically around 1.3) (EHSANI et al., 2018), and ΣF represents the sum of forces acting up the vehicle. The sum of forces can be broken up in its component parts as presented in (2.2).

$$\frac{\partial}{\partial t} v = \frac{\Sigma F}{k_m M},$$ (2.1)

$$\Sigma F = F_{pr} - F_G - F_{drag} - F_{rr}.$$ (2.2)

Here, F_{pr} represents the propelling force – this is the component which originates from the motor or brakes and is the one variable the driver has control over. The term F_G represents the effect of gravity on forwards movement, this force may help or hinder acceleration depending primarily on road inclination. The two others components – drag force (F_{drag}) and rolling

resistance force (F_{rr}) – are both 'resistive forces' which always act against the direction of velocity (OLIVEIRA et al., 2023; ALCANTARA, 2022). Figure 2.2 shows a simple diagram of these forces acting upon the vehicle.
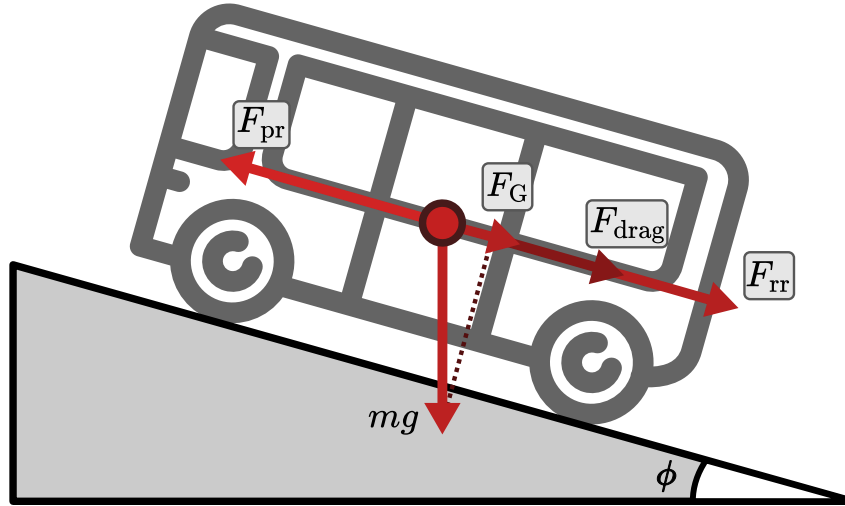
Figure 2.2 – Diagram of forces acting on a vehicular chasis. Adapted from (ALCANTARA, 2022)

The gravitational force (F_G) is the component of the weight of the vehicle which is parallel to the velocity vector, it depends on the angle of the ground slope and so it may be complementary or contrary to the direction of speed. It is defined by (2.3), where g is the gravitational acceleration (approximately 9.81 m/s^2) and ϕ is the angle of the incline in which the vehicle finds itself.

The aerodynamic drag force (F_{drag}) represents the resistance created by the air. In this model, it is represented as always going against the direction of velocity and is described by (2.4), where ρ is air density (approximately 1.2 kg/m^3), A is the frontal area of the vehicle, and C_d is the air drag coefficient (OLIVEIRA et al., 2023).

Rolling resistance force (F_{rr}) is caused by tire deformation and the friction between tire and road. It always acts in opposition to the direction of velocity. Some models, including (ALCANTARA, 2022), represent the rolling force as independent of velocity, as shown in (2.5) – where the rolling resistance coefficient (C_r) is a parameter which depends on tire and road conditions. Other more complete rolling resistance models, like the one in (OLIVEIRA et al.,

2023), account for velocity dependency, as shown in (2.6).

$$F_G = k_m M g \cdot \sin(\phi) \tag{2.3}$$

$$F_{drag} = \tfrac{1}{2} \cdot \rho A C_d \cdot v^2 \tag{2.4}$$

$$F_{rr1} = M g \cdot C_r \cdot \cos(\phi) \tag{2.5}$$

$$F_{rr2} = M g \cdot (C_{r1} + C_{r2} \, v^2) \cdot \cos(\phi) \tag{2.6}$$

2.1.2 Motor and Brakes System

The motor and the inverter are intermediate components between the battery storage system and the propulsion system. During acceleration, a given amount of power is delivered from the battery storage system (P_{batt}), a fraction of which reaches the propulsion system (P_{pr}). This direction of powerflow is depicted in Figure 2.3. Propulsion power is derived from the previously described vehicular movement dynamics, more specifically, it depends on propulsion force (F_{pr}) and the vehicle velocity (v), as described by (2.7).

$$P_{pr} = F_{pr} \times v \tag{2.7}$$

The motor introduces operational limits to the vehicle, these can be best represented by the torque curve, shown in Figure 2.4. This graph shows the maximum amount of torque the motor can deliver (measured in Nm) for a given motor rotational speed (measured in rpm); these variables are proportional to the propulsion force (F_{pr}) and vehicular velocity (v), respectively, as described by (2.8) and (2.9). In these equations, r_w represents the wheel radius, η_t represents the transmission efficiency, and G represents gear ratio from motor to wheel (OLIVEIRA et al., 2023). Note that the overwhelming majority of EVs have a single speed transmission, meaning G is constant. The absence of a gearbox (used to change gear ratios in ICEVs) greatly simplifies the transmission system and is one of the inherit advantages of electric vehicles.

$$F_{pr} = \left(\frac{G}{r_w}\right) \cdot \eta_t \cdot T_m \tag{2.8}$$

$$v = \left(\frac{r_w}{G}\right) \cdot \omega_m \tag{2.9}$$

The motor and the inverter are a source of losses which need to be considered. The relationship between power delivered to and from the battery (P_{batt}) and the power used by the
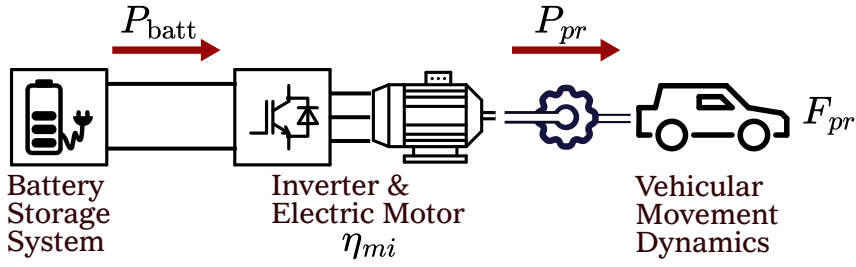
Figure 2.3 – Efficiency relationship between battery power (P_{batt}) and propulsion power (P_{pr}).
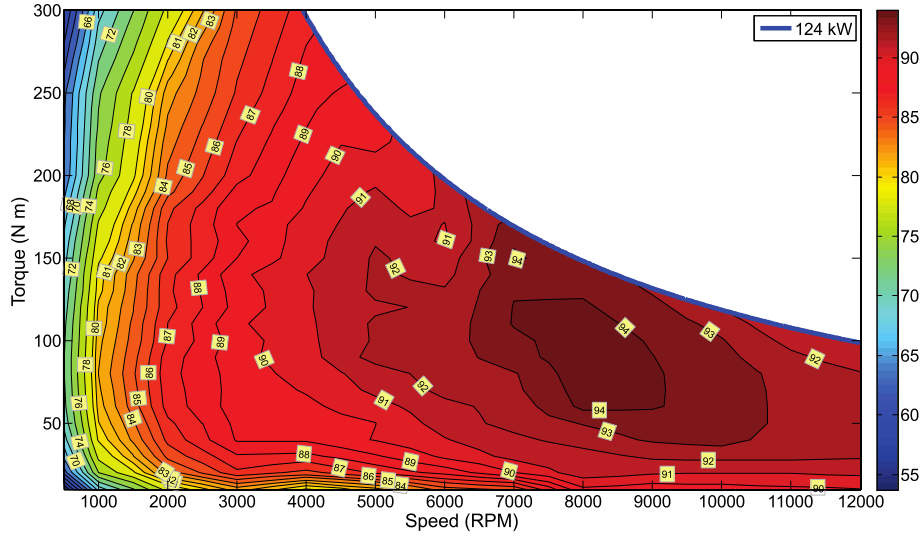
Figure 2.4 – Torque curve from Honda Accord 2014 Motor and Inverter. The Figure includes shaded contour lines that indicate motor-inverter efficiency for every combination of torque-speed the system can provide. Figure originally from (OZPINECI, 2015).

propulsion system (P_{pr}) – shown in Figure 2.3 – is described in (2.10). The coefficient η_{mi} is a value between 0 and 1 which represents the electrical efficiency of the motor and inverter system. One could model this value as a constant, though more commonly, it is a variable that depends on motor torque and speed, as shown in the contour map in Figure 2.4. In simulation, η_{mi} is modelled as a look-up table.

$$P_{batt} = \begin{cases} P_{pr} \cdot \eta_{mi}^{-1}, & \text{if } P_{pr} > 0 & \text{(2.10a)} \\ P_{pr} \cdot \alpha \cdot \eta_{mi}, & \text{otherwise if } |\alpha \cdot P_{pr}| < |P_{\text{reg}}^{\max}| & \text{(2.10b)} \\ P_{\text{reg}}^{\max} \cdot \eta_{mi}, & \text{otherwise} & \text{(2.10c)} \end{cases}$$

The equations in (2.10) correspond to three different scenarios. The first case (2.10a) depicts the scenario when the vehicle is actively accelerating; here, the energy goes from the battery storage system to the propulsion system such that $P_{batt} > P_{pr}$. The two other cases occur

when the vehicle is actively decelerating, i.e. braking. In these cases, propulsion power – which is negative as per (2.7) – is either being dissipated as heat by way of friction braking or is used to charge the battery by way of regenerative braking. Only the regenerative fraction of the braking makes its way back to the battery (P_{batt}) in (2.10) such that P_{batt}<P_{regen}. Case (2.10b) describes the power flow charging the battery when regenerative braking is under its threshold limit, here α represents the fraction of total braking which is regenerative (regenerative factor). Finally, case (2.10c) depicts the scenario when regenerative braking is at its limit. Maximum regenerative braking power (P_{br}^{max}) is value property of the braking and motor system which is typically smaller than the "forward" max power the motor can apply when accelerating (MIRI; FOTOUHI; EWIN, 2021).

The ability to charge the battery by braking can significantly increase the range capacity of an EV. However, regenerative braking is inefficient when speeds are too low, unsafe when deceleration is too high, and unnecessary if the battery is nearly full. In these situation, friction braking is used. This behaviour is modelled in (2.10) using a variable α which varies from 1 (fully regenerative) and 0 (fully friction) as exemplified by the graphs in Figure 2.5.
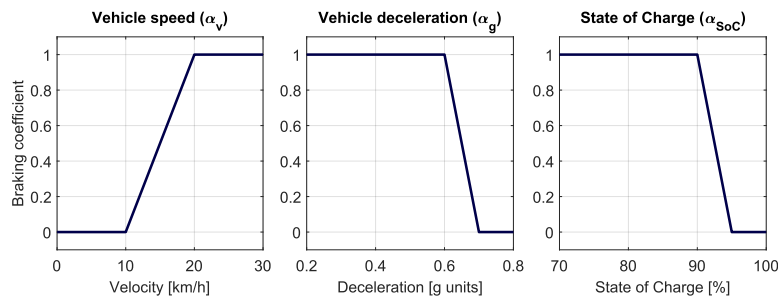
Figure 2.5 – Regenerative factor as a function of speed, deceleration and battery SoC. The final α is equal to the product of all these factors. Adapted from (MIRI; FOTOUHI; EWIN, 2021).

2.1.3 Driver Model

A drive cycle is a dataset of longitudinal vehicular speeds as a function of time. It's most often used by regulatory agencies to standardize fuel consumption and pollutant emissions assessments. Most modern drive cycles are 'transient drive cycles', meaning they are supposed to be a realistic representation of real driving behaviour for a given set of circumstances (urban, rural, highway driving). This is in contrast to 'modal drive cycles' which are sequences of periods

of constant speeds interspersed by periods of constant acceleration/deceleration (NICOLAS, 2013).

Despite not being representative of realistic driving behaviour, modal drive cycles are simpler and more malleable, this can be used to test the effects of particular interventions. For example, (ALVAREZ; LÓPEZ; DE LA TORRE, 2015) uses the now obsolete NEDC drive cycle and changes the intensity of the acceleration slopes to represent the effects of driving aggression (propensity to accelerate aggressively and/or brake abruptly). It finds significant impact on degradation and available range. By contrast, a realistic (transient) drive cycle contains within it assumptions about the driver behaviour which are hard to modify for testing purposes, even though driver behaviour can be a significant battery stress factor (NEUBAUER; WOOD, 2014).

The two most common drive cycle sets are the FTP-75 (used in the United States) and the WLTP (used in the European Union). These and others are available in MATLAB/Simulink using the 'Drive Cycle Source' block included in the Powertrain Blockset and Vehicle Scenario Builder (MATHWORKS, 2017). Alternatively, one could create a custom drive cycle by measuring it experimentally or crafting an artificial one.

Once a drive cycle is decided upon, the driver can be modelled as a simple PI controller which takes as input velocity error (difference between drive cycle reference and the measured velocity) and outputs accelerator and brake pedal commands (a_{acc} and a_{brk}). This can be done by splitting a single output variable which ranges between -1 and 1 into two variables which range from -1 to 0 and 0 to 1, as shown in Figure 2.6. The gain values for the PI controller are chosen through trial and error with the aim to minimize the speed error (MIRI; FOTOUHI; EWIN, 2021).

If the accelerator pedal is being pressed, the motor outputs a fraction of the maximum available torque, which is a function of the current velocity as defined by the torque curve – as seen in (2.11). If the brake is being pressed, a force equal to a fraction of the maximum available braking force (F_{Bmax}) is applied in the opposite direction direction of vehicle velocity, this force includes both regenerative and friction braking – as seen in (2.12). The maximum braking force depends on the normal load acting on the vehicle and the adhesion between tires and the road, it can be approximated by (2.13) where k_{ad} is the adhesion coefficient (around 0.8 for dry asphalt conditions), M is the vehicle mass and g is the gravitational acceleration (MIRI; FOTOUHI;
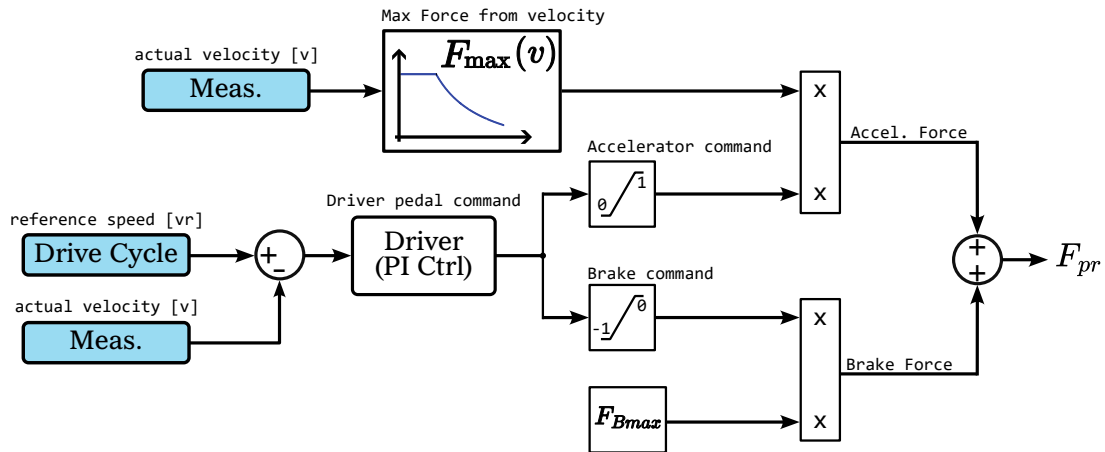
Figure 2.6 – Diagram representation of the PI controller driver model and the acceleration and brake system. Adapted from (MIRI; FOTOUHI; EWIN, 2021).

$$T_{pr} = a_{acc} \cdot T_{m,max}(\omega_m) \tag{2.11}$$

$$F_{br} = a_{brk} \cdot F_{Bmax} \tag{2.12}$$

$$F_{Bmax} = k_{ad} \cdot Mg \tag{2.13}$$

2.2 Lithium-Ion Batteries

The battery storage system is the most important and most expensive single component in an Electric Vehicle. It is only thanks to recent technological improvements and cost reductions that EVs are at all viable. Until recently they were a very small niche of the market, but it's now a exponentially growing sector. This is despite the fact that electric motors themselves are smaller, simpler, quieter, more efficient than combustion engines.

Lithium based batteries have been at the center of this remarkable transformation. This type of battery started being developed commercially in the work of John Goodenough (GOODE-NOUGH, 2018). It quickly came to be used to power small electronics due to being a rechargeable option with higher energy and power density – as is shown in the ragone plot of Figure 2.7 (GARCHE et al., 2013) – and longer life cycles and lower self-discharge rates as compared to the alternatives (WARNER, 2015). This work will focus primarily on the Lithium based chemistries and its challenges. This section serves as a basic introduction to Lithium-Ion Batteries and discusses some of the difficulties related to modelling and degradation.
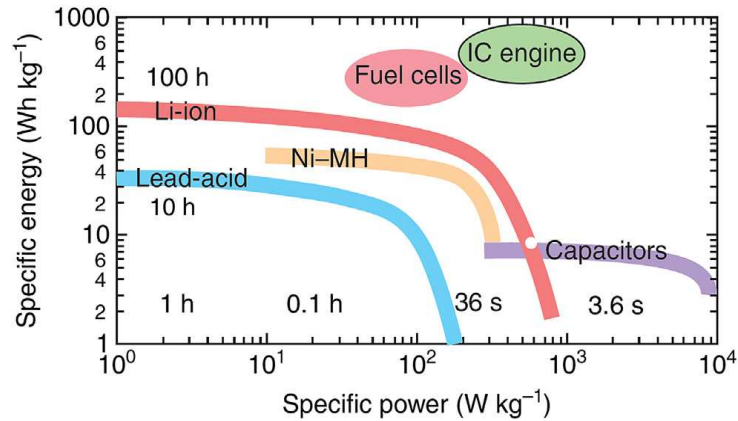
Figure 2.7 – Illustrative ragone plot (energy and power density) for various energy storage devices. Figure originally from (GARCHE et al., 2013).

2.2.1 Battery Fundamentals

The cell is the most basic unit of a battery storage system. Inside each li-ion cell are three very thin sheets of material corresponding to the three electrochemically relevant regions of a battery: anode, separator, and cathode. These strips are placed in series and folded in layers inside the cell case, the inside of which is permeated by a liquid electrolyte solution. Structurally, commercial battery cells are constructed in one of three geometries: cylindrical, prismatic, and pouch cells – shown in Figure 2.8 (PREGER; TORRES-CASTRO; MCDOWALL, et al., 2023). These geometries each have their own advantages and disadvantages, listed in Table 2.1, adapted from (LI, 2022).

There can be different variants of Lithium-ion batteries, meaning the anode and cathode films themselves may be made with different materials. The anode region typically contains
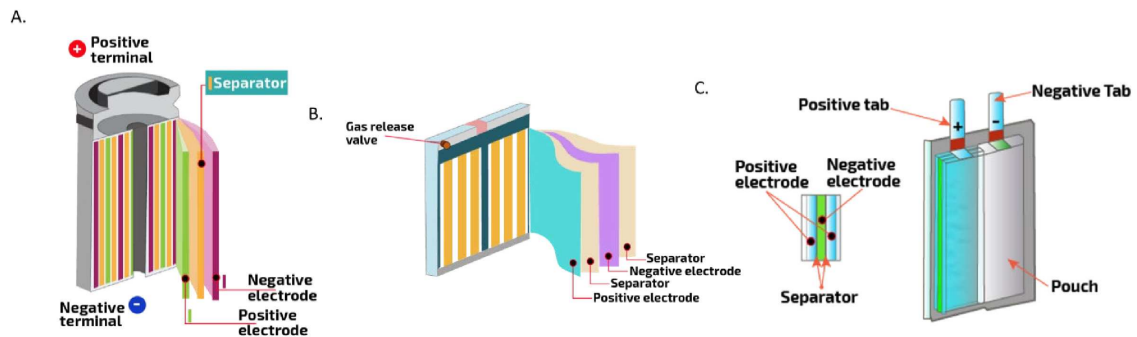
Figure 2.8 – Schematic drawings of three of the most common battery structural configurations. a) Cylindrical; b) Prismatic; c) Pouch. Figure originally from (PREGER; TORRES-CASTRO; MCDOWALL, et al., 2023).

graphite as the negative electrode active material, though lithium-titanate (LTO) is an alternative which allows for faster charging and longer cycle lives though it greatly decreases power and energy density. In contrast, there are many options for cathode material, various alternatives are utilized in different contexts (MARQUIS, 2020; NEWMAN; BALSARA, 2021). Table 2.2 presents a summary of the properties of some of the more prominent battery chemistries, adapted from (WARNER, 2015). Of these, Lithium-Iron-Phosphate (LFP) based cathodes have been growing significantly in prominence for electric vehicles (KANE, 2022; IEA, 2024).

During discharge, lithium atoms held within the graphite (or equivalent anode material) are released into the electrolyte as ions (process refered to as 'deintercalation') while the newly free electrons flow out the cell and are used to do "work" (provide power). The graphite anode oxidation and reduction (redox) reactions which allow for battery use are shown in (2.14). From there, the lithium ions are transported through the electrolyte and across the separator into the positive electrode. There, they combine with free electrons (brought in from outside the cell)

Table 2.1 – Advantages and disadvantages of different kinds of battery cell geometric structures. Table originally from (LI, 2022).

	Advantages	**Disadvantages**
Cylindrical	Mainly steel shell, low manufacturing cost, high process maturity and high production efficiency. High yield and consistency.	High quality required for large-scale grouping, high grouping cost, and relatively short cycle life. High power limitation of mechanical structure.
Prismatic	High structural reliability. Long cycle life of battery cell.	Heavy case, low energy density High cost of mechanical components.
Pouch	High mass and volume energy density, customizable.	Weak mechanical properties, easy to leak, high requirements for external module protection structure, and relatively difficult design for heat dissipation.

Table 2.2 – Properties of some of the main lithium-ion based chemistries. Adapted from (WARNER, 2015).

	Lithium Iron Phophate	Lithium Titanate	Lithium Nickel Cobalt Aluminum	Lithium Nickel Manganese Cobalt
Cathode chemistry descriptor	LFP	LTO	NCA	NMC
Specific energy (Wh/kg)	80-130	70	80-220	140-180
Energy density (Wh/L)	220-250	130	210-600	325
Specific power (W/kg)	1400-2400	750	1500-1900	500-3000
Power density (W/L)	4500	1400	4000-5000	6500
Volts per cell (V)	3.2-3.3	2.2-2.3	3.6	3.6-3.7
Cycle life	1000-2000	>4000	>1000	1000-4000
Self-discharge (% per month)	<1%	2-10%	2-10%	1%

and settle into the positive active material (the insertion of lithium-ion into the active material is known as 'intercalation'). The whole process is depicted in Figure 2.9 – adapted from (FULLER; DOYLE; NEWMAN, 1994). During charging, the opposite occurs: lithium deintercalates from the positive electrode and intercalates into the negative electrode (NEWMAN; BALSARA, 2021; OGUMI; INABA, 2002; WANG, S. et al., 2021). A more detailed explanation of the inner working of an lithium-ion cell is found in Chapter 3.
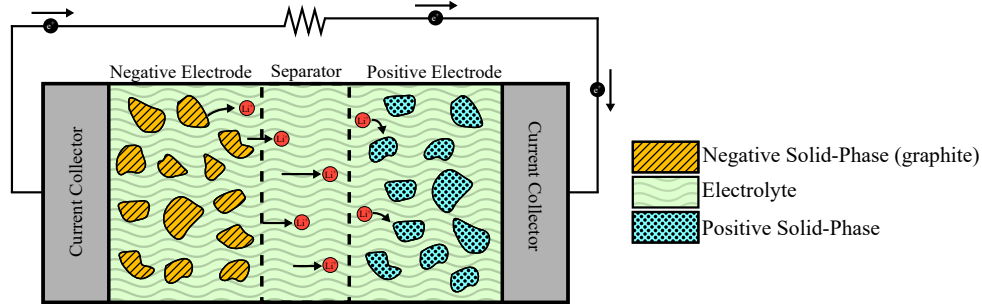
Figure 2.9 – Schematic of battery cell during discharge. Adapted from (FULLER; DOYLE; NEWMAN, 1994).

$$C_6 + Li^+ + e^- \underset{\text{Discharge}}{\overset{\text{Charge}}{\rightleftharpoons}} LiC_6 \qquad (2.14)$$
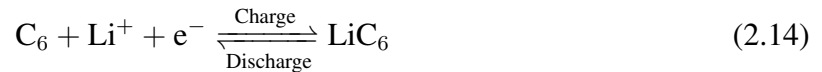
A single individual cell has a pretty limited energy and power capacity, and so, for larger applications, many cells are assembled in series (to increase output voltage) and in parallel (to increase maximum output current). For commercial applications, these battery bundles are standardized as "modules" which include dozens of battery cells connected mechanically and electrically, monitoring equipment, a thermal management system, safety features, and other important components. For very high power applications, like electric transportation, multiple modules are connected into a structure known as a "Battery pack".

To coordinate all these cells and ensure safe and efficient operation, the battery pack needs to be actively controlled. The Battery Management System (BMS) is an electronic managements scheme meant to monitor, protect, and optimize the performance of one or multiple battery modules. A BMS has a wide range of functionalities: monitoring, protection, charge and discharge management, thermal management, communication, diagnosis, and data management. Protection involves ensuring that the batteries operate within a safe voltage, current and temperature window in order to avoid accidents (particularly thermal runaway) and to minimize degradation (which is particularly sensitive to temperature deviation (WALDMANN et al., 2014)). If the BMS detects irregularities, it should be able to disconnect the offending module/branch of cells (GABBAR; OTHMAN; ABDUSSAMI, 2021; WARNER, 2015).

The BMS is a combination of one or more controllers with sensor components which track metrics relevant to battery operation – the most important of which are voltage, current, and surface cell temperature. In a centralized system, there is typically a single controller which oversees the entire battery pack, this approach saves on hardware but requires extra wiring which adds weight, cost, and risk of failure. Recently, some effort has gone into researching Wireless BMS systems which bypass that concern (SAMANTA; WILLIAMSON, 2021). Alternatively, distributed BMS topologies have a centralized host controller and multiple smaller controllers directly attached to the individual cells or modules. This approach is often preferred because it offers greater functionality and control at a detailed level – closer to the individual cell; even if it's more expensive as it increases the amount of electronics required (GABBAR; OTHMAN; ABDUSSAMI, 2021; WARNER, 2015).

Some of the functions of a BMS depend on hidden internal metrics such as State of Charge (SOC) and State of Health (SOH) which can't be measured directly and must be estimated. This is done using a battery cell model.

2.2.2   Battery cell models

Lithium-Ion Batteries are non-linear, electrochemical systems. They are an inherently challenging object to model. The primary trade-off which a system designer must at all times consider is between accuracy and computational/model complexity. The three most common battery models for a fresh battery cell are the bucket model, the equivalent circuit model (ECM), and electrochemical model (HU; DENG, et al., 2022). Of these, the bucket model is the simplest possible model and the electrochemical models are typically the most complex. (RENIERS; MULDER; OBER-BLÖBAUM, et al., 2018) compares these three models in the context of control optimization for energy cost arbitrage using a grid-connected battery system; it finds that more accurate models allowed for more realistic safety limits which both provided more available usable capacity while still limiting degradation. This resulted in significantly more profit over the course of the studied period.

The simplest of these models, the bucket model, is a SoC tracker which represents the battery as a mere repository for energy – much like a fuel tank (RENIERS; MULDER; OBER-BLÖBAUM, et al., 2018). This model tracks the internal energy supply $E(t)$ (measured in Wh or J) overtime as a function of power $P(t)$ (measured in W). This simple formulation isn't really

useful for Battery Management Systems and other detailed oriented applications. It is mostly used for high-level, grid-wide storage optimization problems (HESSE et al., 2017; RIFFONNEAU et al., 2011; HU; DENG, et al., 2022); but even in the context of techno-economic assessment, (RENIERS; MULDER; OBER-BLÖBAUM, et al., 2018) shows that this model can substantially underestimate the business case when compared to the two other types of models.

This section will instead focus on ECMs and the electrochemical models, in sections 2.2.2.1 and 2.2.2.2 respectively.

2.2.2.1 Equivalent Circuit Model

The equivalent circuit models are the family of battery models most widely used in Battery Management Systems and the ones which are most familiar to electrical engineers. They inhabit a good middle ground between accuracy and model simplicity.

These models use a voltage source to represent the Open Circuit Voltage (OCV), which is the steady-state (no current) voltage for a given SoC; and uses electric circuit passive elements (resistors and capacitors) to represent the dynamic response and ohmic losses of a battery cell. In most of these models, the resistance and capacitance values may vary depending on factors such as temperature, SoC, and degradation. In these cases, the values should be constantly updated for the model to be adequately accurate (HU; FENG, et al., 2019).

What follows are different kinds of ECMs, listed in order of increasing complexity.

The simplest kind of ECM is the 'Internal Resistance Model', shown in Figure 2.10a). It is made up of a voltage source and a series resistance (R_{int}) (OLIVEIRA et al., 2023; HU; LI; PENG, 2012). The difference between this model and the bucket is that this one is able to represent voltage and current separately, as opposed to just power flow. Though this model can be used to approximate SoC and ohmic losses (heat) in real time, it is unable to reflect the dynamic characteristics of the battery.

The simplest model which aims to replicate a battery cell frequency response is the 'Thévenin model', also known as 'n-RC model'. This is the most commonly used ECM within electrical engineering, seeing as it balances accuracy and simplicity well. It uses a resistor in series (R_{int}), same as the previous model, but adds at least one additional RC parallel network (R_i and C_i). Typically, either one or two RC bundles are used; though in theory, the number of

parallel RC branches can be arbitrarily large. Figure 2.10b) shows the 2nd order RC model (HU; LI; PENG, 2012).
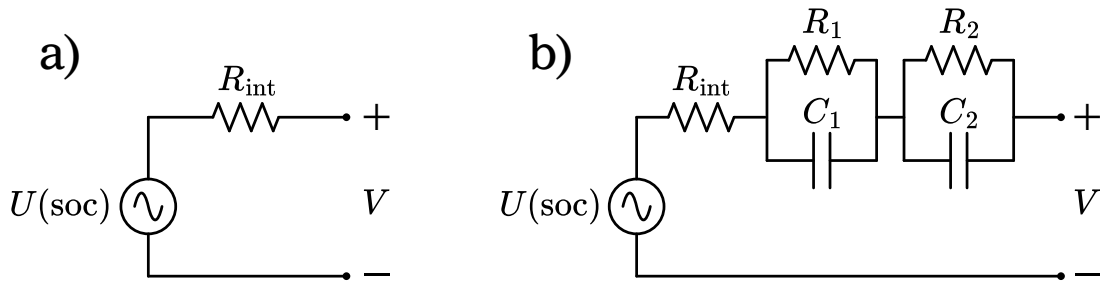
Figure 2.10 – Equivalent Circuit Models. a) Internal resistance model; b) Second order Thévenin model.

To improve upon the Thévenin model, (MU et al., 2017) uses fractional order circuit components to obtain frequency responses which more closely resemble the Electrochemical Impedance Spectroscopy (EIS) results. EIS is a technique for analyzing electrochemical systems such as batteries. It involves applying a small amplitude AC voltage or current signal superimposed over a DC signal, over a range of frequencies (typically from around 0.1Hz to 100kHz), and plotting the resulting impedance using a Nyquist plot (LAZANAS; PRODROMIDIS, 2023; CHOI et al., 2020; AZIZIGHALEHSARI et al., 2023). A simplified experimental set up is shown in Figure 2.11 – adapted from (LAZANAS; PRODROMIDIS, 2023). This method allows one to observe various electrochemical processes over a wide range of frequencies in a non-destructive way. A typical EIS plot for a lithium-ion battery is shown in Figure 2.12 (BOJ et al., 2023). Because it is possible for different equivalent circuits to generate the same or similar frequency profiles, the ECMs which are based on EIS data should ideally relate individual electrical components to meaningful physical processes instead of just striving for numerical approximations.

At the mid-frequency range, the EIS plot is characterized by a semi-elliptical shape. This represents the charge transfer dynamics of lithium-ions between the electrode active material and the electrolyte. This shape can be approximated by having a parallel RC branch with time constant $\tau = RC$. However, when using an ideal capacitor "C", the resulting shape will be a semi-circle of constant radius. To better approximate measurements, the idealized capacitors are replaced with Constant Phase Elements (CPEs), which are non-linear representations of imperfect (so called 'dual-layered') capacitors. The relationship between current and voltage for a CPE is described by (2.15) and its Laplace transform is described by (2.16), where C is the
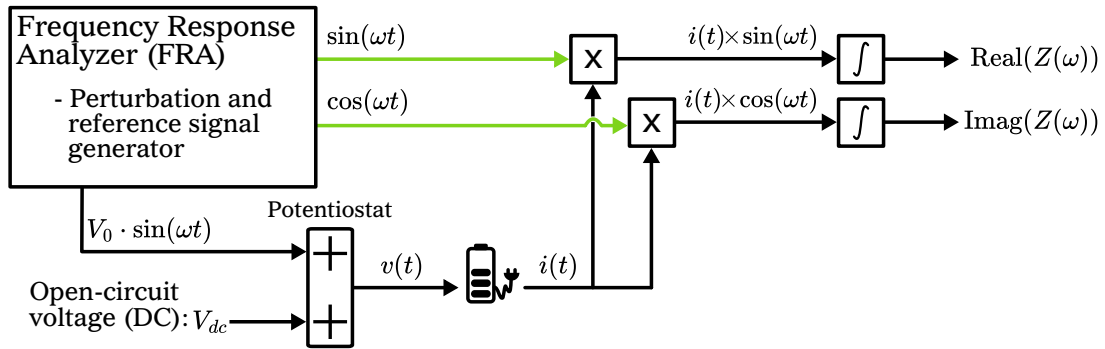
Figure 2.11 – Simplified experimental setup for potentiostatic EIS experiment. Adapted from (LAZANAS; PRODROMIDIS, 2023).
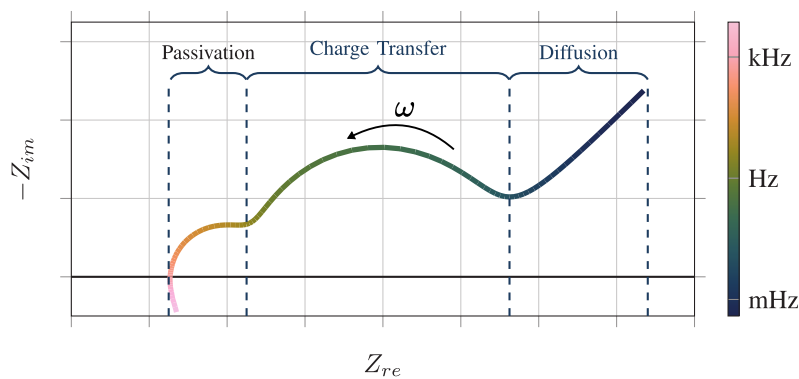
Figure 2.12 – Ilustrative Nyquist plot visualization of an ideal EIS measurement. Note that different impedance features become prominent at different frequency ranges. Figure originally from (BOJ et al., 2023).

CPE capacitance value and α is a frequency independent constant between 0 and 1, where α=1 is an ideal capacitor (MU et al., 2017; LAZANAS; PRODROMIDIS, 2023). Figure 2.13 compares the Nyquist frequency plot between a parallel R-C circuit and two parallel R-CPE circuits; in both cases, the frequency that is associated with the peak of the semi-circle is ω_p=$1/\tau$, where τ is the time constant of the RC element: τ=RC.

$$i = C\frac{d^{\alpha}}{dt^{\alpha}}v \tag{2.15}$$

$$I(s) = Cs^{\alpha}V(s) \tag{2.16}$$

Another significant feature of the EIS plot is the Warburg Impedance, which dominates at low frequencies. It shows up in the plot as a straight line with a slope of 45° degrees at the right-most side of the graph. It indicates the resistance and capacitance growth as frequency decreases. This phenomena is represented in the circuit by the custom made component Z_W, which is mathematically described in (2.17), where σ is the Warburg constant; this is equivalent to a CPE where α is set to 0.5.

$$Z_W = \frac{\sigma}{\sqrt{\omega}} - j\frac{\sigma}{\sqrt{\omega}} \qquad (2.17)$$
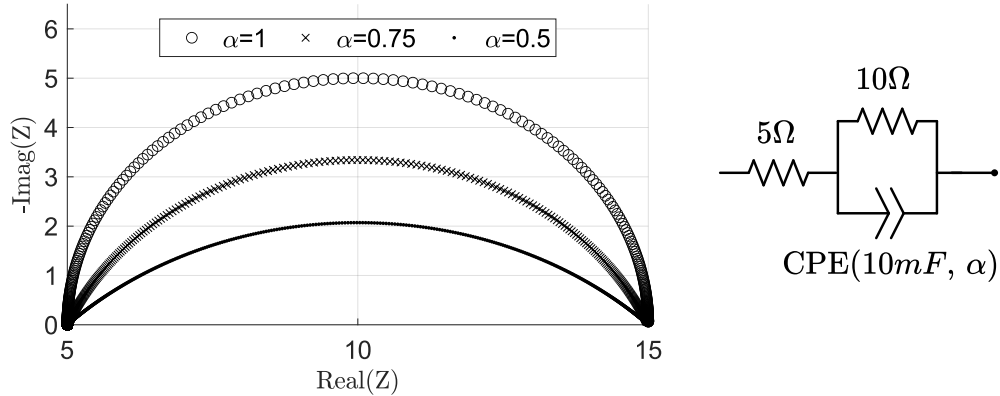
Figure 2.13 – Comparison of the Nyquist plots from parallel R-CPE circuits for different values of α. Note that a CPE with α=1 is equivalent to an ideal capacitor.

The Warburg impedance only becomes dominant at very low frequencies, with a transition point around 1Hz, and proceeds to grow slowly. It is representative of the mass transport diffusion limitations. When a battery system is at rest, lithium atoms are stored inside the anode active material at more of less an even concentration everywhere; once the redox reaction starts, the lithium deintercalation depletes the atoms closest to the electrode-electrolyte interface first. This creates an uneven concentration distribution of lithium in the solid-phase which is eventually corrected by the diffusion of lithium from the bulk of the electrode towards the surface. This is a very slow process that occurs over a long time, and as it does, there is small and slow rebound in cell open-circuit potential as the electrode surface concentration converges (TAYLOR; GILEADI, 1995).

The Randles circuit, shown in Figure 2.14a), is the standard equivalent circuit representation of the battery EIS response, featuring the Warburg impedance in series with a resistor, and both in parallel with a CPE. At high frequencies, current flows through the capacitor; at low frequencies, current flows through the resistor and Warburg impedance. The frequency range where the Warburg becomes significant is far enough away from the frequency range of the capacitor that the Randles circuit can be rearrenged such that the Warburg impedance is in series with the R-CPE bundle, as seen in Figure 2.14b) – a slightly simpler model (LAZANAS; PRODROMIDIS, 2023).

In applications where current is frequently oscillating and low-frequency signals do

not play as much of a role, such as drive cycle profiles, the Warburg impedance may even be disregarded, as is seen in (GUHA; PATRA, 2018). More commonly, the Warburg impedance is itself replaced by an equivalent circuit. Though there is no combination of components which will exactly match the Warburg frequency response, it can be approximated by a infinite sequence of parallel R-C segments in series; this resemble the previously n^{th} order RC Thévenin circuits, which could be arbitrarily large.

Another common alternative is the 'two time constant with Warburg', shown in Figure 2.14c). In addition to all the component present in the Randles circuit: series resistance R_{int} (represents electrolyte resistance), the first R-CPE bundle (charge transfer), and the walburg impedance (diffusion); this model includes an additional R-CPE structure with a smaller time constant τ (higher frequency) which is associated with the Solid Electrolyte Interface (SEI). The SEI is the result of an unintended chemical side-reaction that creates a permeable film between the electrolyte and electrode (impedance increase) and which consumes cyclable lithium (capacity fade, loss of lithium inventory). As such, keeping track of the resistance and capacitance value of this element could be a useful way of quantifying the aging process (JALKANEN et al., 2015; CHOI et al., 2020).
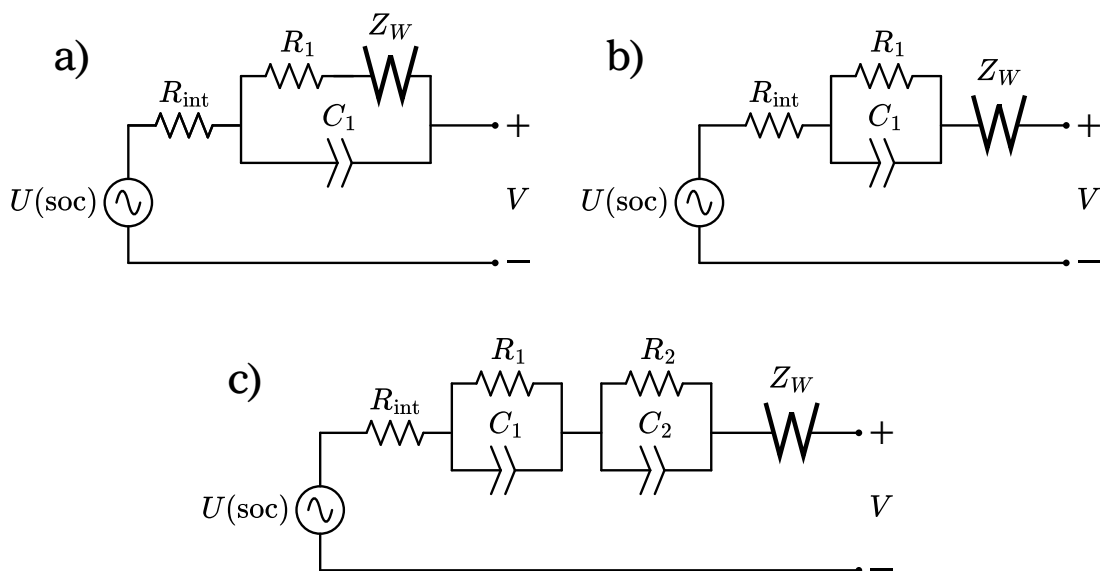
Figure 2.14 – Equivalent Circuit Models with Warburg impedance. a) Full Randles model; b) Simplified Randles model; c) 2τ with Warburg.

2.2.2.2 Physics-Based Models

Physics-based models (alternately known as 'electrochemical' or 'mechanistic' models) are methods for modelling battery systems which arise out of electrochemistry (NEWMAN; BALSARA, 2021). The goal is to represent the internal chemical state of the battery by modelling the reactions and movement of particles which take place within the system. Most of existing electrochemical models are based on the Doyle-Fuller-Newman (DFN) model first developed in (DOYLE; FULLER; NEWMAN, 1993; FULLER; DOYLE; NEWMAN, 1994). It is a continuum model which represents most of its variables as varying continuously along the length of the cell, represented by the x-axis, where the negative current collector sits at x=0 and the positive current collector ends at x=L. The one exception is lithium solid-phase diffusion. Flows in solid-phase lithium concentration (c_s) inside each of the electrodes active material are represented as occurring inside spherical microscopic solid-phase particles with an r-axis radius. Where r=0 is the electrode bulk and r=$R_s^{\pm}$ is the average electrode particle radius, also the electrode surface. In this model, at every discretized node of the x-axis there is a representative spherical particle with an r-axis. Because of this, this models is also known as the "Pseudo Two-Dimensional" (P2D) model.

The DFN model can be broken down into three main phenomena. Charge conservation governs how the voltage potential varies within the solid-phase and in the electrolyte (ϕ_s and ϕ_e); lithium diffusion describes how the lithium concentration varies within the electrolyte and within the solid-phase (c_e and c_s); and transfer current describes the transfer of charges between the active material and the electrolyte due to the redox reaction (j_{tr}).

The original DFN model assumes no degradation and isothermic conditions (no internal heat generation from batteries). Since then, submodels have been created in order to represent the generation of internal heat and side-reactions, unintended chemical processes which lead to capacity degradation and impedance rise. Many of these submodels are 'compatible' with DFN and can be included modularly into the model.

When these submodels are included into the full battery model, the resulting mathematical system is composed of various interacting components represented by dozens of Partial Differential Equations with non-linear elements and variables which exist along a continuous x and r axis. This resulting system is computationally complex and numerically hard to solve. Depending on the application, however, it may be possible to simplify the DFN model such that

it can be solved significantly faster without sacrificing much in terms of accuracy. These models are discussed in greater detail in Section 3.1.2.

The mathematical complexity of these battery models is so remarkable that even implementing one of the simplified versions presents a significant challenge. Thankfully, there already exist good open-source implementations of battery physics-models accessible for researchers. The present work uses PyBaMM, a particularly complete and well documented battery simulation library for Python. It includes many battery models of different levels of complexity and some pre-existing parameter sets from the literature. This software is discussed in more detail in Section 4.2 (SULZER et al., 2021; O'KANE et al., 2022).

A more in-depth account and explanation of this family of models, including its governing equations are presented in see Chapter 3.

2.2.3 Degradation of Batteries

Battery degradation is the result of unintended side-reactions and mechanical stresses which occur within the cell. The four types of degradation are Loss of Lithium Inventory (LLI), Loss of Active Material (LAM), Loss of Electrolyte (LE) and Resistance Increase (RI); the effects of aging are, primarily, capacity and power fade (HAN; LU, et al., 2019; HU; XU, et al., 2020).

The most significant degradation processes are represented graphically in the diagram of Figure 2.15 – adapted from (RENIERS; MULDER; HOWEY, 2019). These are:

- **SEI Growth:** The Solid Electrolyte Interface (SEI) is an insulating layer of organic material – represented as a blue layer in Figure 2.15 – which is formed from a reaction which occurs in the interface between the electrolyte and negative electrode. This reactions consumes lithium atoms and electrolyte solvent, the lithium deposited inside this layer of material is inaccessible for future use (LLI). Though this is the one most significant causes of capacity fade in a lithium based battery, it is governed by complex mechanisms which are still not fully understood – as such, there are different and competing approaches for modelling it mathematically (RENIERS; MULDER; HOWEY, 2019; SINGLE; LATZ; HORSTMANN, 2018; EDGE et al., 2021).

- **Li plating:** Lithium ions form a layer of metallic particles on top of the electrode-

electrolyte interface instead of intercalating into it – this is represented as a redish-orange layer in Figure 2.15. This most often occurs within the negative electrode, particularly in the region nearest the separator. It is associated with fast charging, low temperatures, and batteries operating after the first recommended EoL. This side-reaction is additionally risky due to the possibility of li-plating piercing the separator and causing a short circuit (YANG et al., 2017; EDGE et al., 2021).

- **Electrode cracking and dissolution:** As an electrode charges and discharges, the active material particles slightly expands and contracts. This is a source of mechanical stress which may cause cracks and lead to LAM and accelerated SEI growth (HAN; LU, et al., 2019; O'KANE et al., 2022).

- **Pore-clogging:** As the SEI and Li-plating films grow, they take up space previously occupied by the electrolyte. As the volume share of the electrolyte (ε_e) – alternatively called 'porosity' – decreases the electrolyte conductivity falls and the internal resistance increases (RI) (RENIERS; MULDER; HOWEY, 2019; YANG et al., 2017).
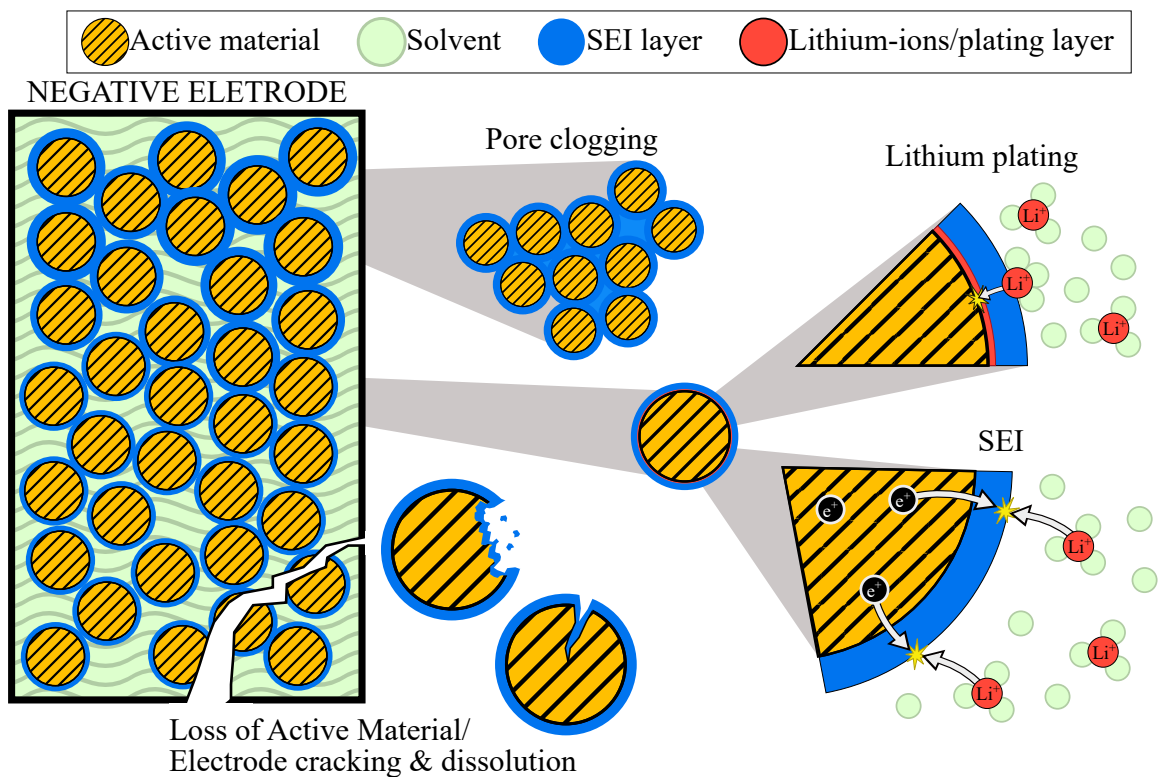
Figure 2.15 – Representation of the most significant degradation mechanisms which occur in a lithium based battery cell. Figure adapted from (RENIERS; MULDER; HOWEY, 2019).

In all cases, temperature is the single most significant stress factor. (WALDMANN et al., 2014) studies degradation between $-20^{o}C$ and $70^{o}C$ and finds increased rates of aging for temperatures both above and below $25^{o}C$; higher than that leads to faster SEI formation and lower than $25^{o}C$ leads to faster lithium plating. This is the reason why a BMS thermal management is so critical.

For the majority of a batteries life-cycle, SEI growth is the most significant of the degradation mechanisms. During this period, capacity degradation occurs linearly. At some point, however, Li-plating grows to become the dominant cause of aging; when that happens, capacity no longer decreases linearly, but rather exponentially. This transition point is known as the "aging knee-point", shown in Figure 2.16 – adapted from (HU; DENG, et al., 2022). This happens past the industry standard EoL (80% SoH) but is relevant for second life applications.
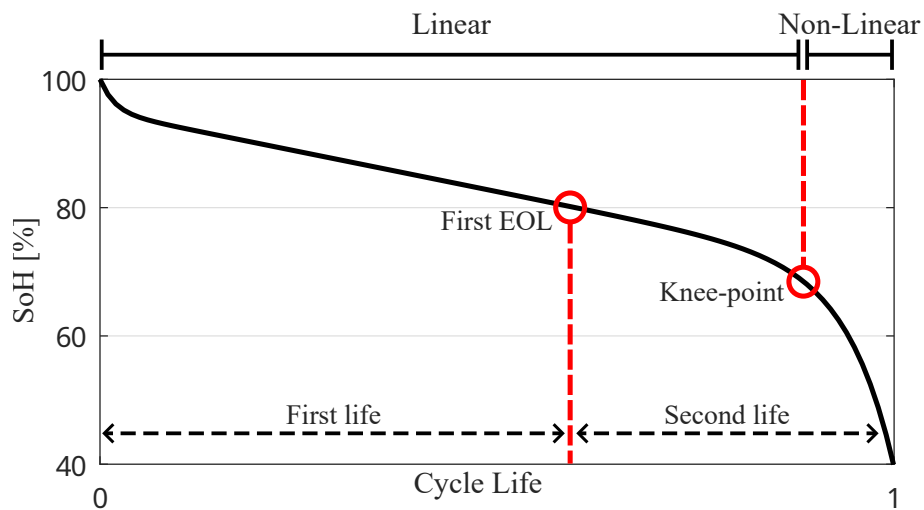
Figure 2.16 – Typical evolution of battery capacity over the various stages in a cell life-cycle. Adapted from (HU; DENG, et al., 2022).

2.2.3.1 Types of Aging Models

There are three main types of battery aging models: empirical, mechanistic, and data-driven (HU; XU, et al., 2020).

Empirical models are based on heuristic correlations between the capacity and resistance trajectories and identified stress factors (GANESH; D'ARPINO, 2023). These models disregard the actual internal mechanisms which are the cause of degradation. Instead, they are typically established by fitting experimental data into a equation trajectory (HU; FENG, et al., 2019). In some cases, the empirical model may be derived by simplifying more complex mechanistic

mathematical formulations, such is the case in (RECHKEMMER et al., 2019). These models are known as 'semi-empirical'. Most empirical models make the distinction between calendar and cycle degradation, the former is due primarily to passage of time – independent of usage – and the latter is caused by usage.

Each type of degradation has its associated stress factors, some common ones include time, mean SoC, and temperature for calendar aging and total current throughput, Depth-of-Discharge (DoD), total number of cycles, and temperature for cycle degradation; note that different models may consider different stress-factors and that these are just some of the more common ones.

Compared to the other approaches, empirical models are relatively easy to implement and are typically computationally simple. Their primary disadvantage is that each model is typically only tuned for a limited set of operating conditions (tied to the experimental results used to initially 'calibrate' the model) and is otherwise low-accuracy. As examples of empirical models, (SAUER; WENZL, 2008) and (GANESH; D'ARPINO, 2023) both compare empirical aging models with more complete, mechanistic aging models. (BAGHDADI et al., 2016) shows a fairly complete empirical model which takes into account a lot of different variables. The National Renewable Energy Laboratory (NREL) has its own empirical lifetime predictive modelling algorithm included in their battery simulation package: BLAST (Battery Lifetime Analysis and Simulation Tool Suite) (NEUBAUER, 2014; NEUBAUER; SIMPSON, 2015).

Mechanistic models simulate aging by modelling the internal chemical processes like SEI growth and Li plating which lead to degradation. These models are extensions of the physics-based models; as such, they inherit a lot of the same benefits and downsides. Mechanistic degradation models are derived from electrochemical first principles and are able to provide insight into the internal state of the battery cell; as such, if properly tuned they are more robust and precise. The downside is that they require extensive parameter estimation and are quite computationally expensive (HU; FENG, et al., 2019; HU; XU, et al., 2020).

In a physics-based model with mechanistic degradation, each individual cause of degradation has to be mathematically described; this is a challenge but thankfully the literature already contains many examples, often multiple alternative representations for the same mechanisms (RENIERS; MULDER; HOWEY, 2019). Because SEI growth is the overwhelmingly dominant cause of degradation – particularly during first-life – a lot of models choose to represent only this phenomenon and not the others. Though it is possible to predict capacity trajectory with this one

single model sufficiently well, by modelling multiple degradation models, there can be emergent inter-mechanism interactions which better reflect real cell aging dynamics. This is a concept known as 'path-dependent aging' – it posits that since different degradation mechanisms are triggered under different circumstances and that past degradation affects future degradation, it is therefore important to model various degradation mechanisms to capture the various 'aging paths' (RAJ et al., 2020; EDGE et al., 2021). Combining degradation models does create feedback loops which can be more accurate than either model in isolation, though this process often requires some fine-tuning of models parameters to properly function (RENIERS; MULDER; OBER-BLÖBAUM, et al., 2018).

Combining mechanistic degradation models is particularly important for modelling the aging knee-point – the point late in a battery life when capacity loss transitions from growing linearly to growing exponentially, exemplified in Figure 2.16. In (YANG et al., 2017), a P2D model with SEI growth, pore clogging, and Li-plating is used. For the initial stages of the battery life, SEI growth is the dominant degradation factor. Then, as electrolyte porosity decreases, the electrolyte potential near the separator falls. This eventually enables rapid Li-plating in the region near the anode-separator interface. With these three degradation models, (YANG et al., 2017) is able to simulate this emergent behaviour which replicates both the aging knee-point and the observed post-mortem degradation patterns (build up of metallic lithium in the region of the anode near the separator) remarkably well (KLETT; ERIKSSON, et al., 2014; KLETT; SVENS, et al., 2015). Another work in the same line as (YANG et al., 2017) which highlights the potential of mechanistic based degradation models is (ATALAY et al., 2020). Here, degradation parameters are calibrated based on the degradation experimental results from two battery stress tests. Later, the resulting model is compared to a new battery under a different degradation experiment. The result is that the (ATALAY et al., 2020) model is able to predict the capacity trajectory with high accuracy, including the aging knee-point transition.

Data-driven models are a new development in battery health estimation, enabled by advancements in data analytics and artificial intelligence. This type of model is similar to the empirical method in the sense that it aims to find a mathematical relationship between the degradation data and battery inputs while being agnostic about the underlying physical processes; the difference is that this method requires an order of magnitude more data and result in significantly more the complex models (AYKOL et al., 2021). This is possible in

large part thanks to Machine Learning (ML) techniques, which allow for the automation of analytical model building. The end results are models which can be just as accurate as the mechanistic models while being more computationally appropriate for real time data processing, so long as the present operating conditions are represented within the training data. The primary downside are the huge amounts of data which are required to create a realistic model and the enormous computational burden needed to actually train the model (HU; XU, et al., 2020; AZIZIGHALEHSARI, Seyedreza et al., 2021). More recently, hybrid Data-Driven and Physics-Based models have been proposed. The simplest version of this involves using mechanistic degradation models to create synthetic battery data to train a Data-driven model. There is also the possibility of more directly encoding the governing equations of a physics-based model such as the Doyle-Fuller-Newman model (DOYLE; FULLER; NEWMAN, 1993) into the machine learning algorithm. This option would allow for a more robust algorithm that would require less data to train. (AYKOL et al., 2021) is a short paper with some suggestions as to how this might be done.

Choosing which of these models to use depends on the application and available resources; it is a balancing act between trade-off.

2.3 Second Life Batteries

After the end of its first life in an Electric Vehicle, Lithium Batteries may be repurposed for a different use case. This is an area of study that is expected to become increasingly relevant as the market for Electric Vehicles continues to expand and more battery packs start to be retired.

Given that Second-Life batteries have partially degraded power delivery and energy storage capacity, the available use cases are limited to those with lesser requirements. Section 2.3.1 discusses some of the problems related to the economic viability of second-life batteries. Section 2.3.2 discusses some of the challenges with evaluating the Health Indicators for an aged Battery Pack and from that estimating the rest of useful life (RUL).

2.3.1 End of Life Logistics and Economic Viability

There is a great deal of potential for second-life batteries. Once a electric vehicle battery system reaches its first end-of-life – at around the 80 to 70% SoH range – it can still be used

for between 5 and 10 more years in stationary applications (VENKATAPATHY; TAZELAAR; VEENHUIZEN, 2015; MATHEWS et al., 2020; HARAM et al., 2021). During this period, these recycled batteries will be replacing new batteries, avoiding the environmental damage associated with the cell manufacturing process – this includes the release of Greenhouse Gases, production of toxic waste product, mineral excavation, etc. (AHMADI; YOUNG, et al., 2017). Additionally, a lot of the proposed second life use-cases are auxiliary to clean energy sources (eg. regulating power delivery for renewable sources, thus ameliorating the problem of intermittency). This makes Second Life Batteries more environmentally beneficial (AHMADI; YIP, et al., 2014). However, for this potential to be realized, second life batteries must be economically viable – which, as of now, is still uncertain.

The two biggest roadblocks which limit the viability of wide-spread adoption of SLBs is the price of new batteries and the costs associated with the collection and repurposing processes. Over the past decade, battery prices have fallen significantly, though this trend has slightly reversed in recent years (BLOOMBERGNEF, 2022). It is still widely expected that the price for new lithium cells will reach US\$100/kWh. More recently, the target price for a new cell has reached as low as US\$80/kWh, as per the United States Department of Energy (DOE, 2020); at this price range, SLBs might struggle to remain competitive. Due to their more limited lifespan and power delivery capabilities, second-life batteries must be significantly cheaper than new lithium cells to be considered equivalent; additionally, in many use-cases, second-life batteries will be in competition with lead-acid and flow batteries, which can be significantly cheaper (ZHU et al., 2021). (MATHEWS et al., 2020) estimates that the price cut-off at which point SLB becomes worth is less than 60% of the original cost, (NEUBAUER; SMITH, et al., 2015) places this limit at a maximum of 72% – though both find that this depends on second-life use-case and rate of capacity loss.

Trouble arises due to the high labour costs associated with the end of life process. Once a battery has experienced its first end of life, it must be collected, assessed for damage and diagnosed for degradation metrics, disassembled, and then reassembled. This process, shown in Figure 2.17, is time consuming and labour intensive; this leads to inflated costs.

(RALLO et al., 2020) studies the battery disassembly process in great detail, each task is broken down into component steps. These are then analyzed according to the number of technicians required and time taken; from that, a cost estimate is generated. The three steps
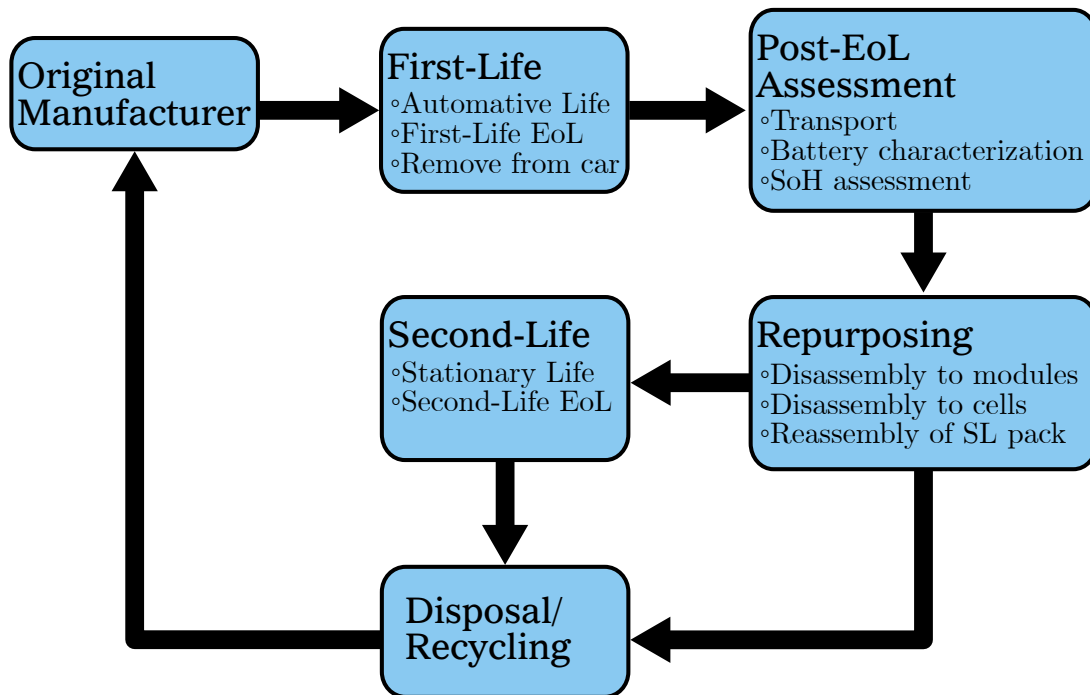
Figure 2.17 – Battery life cycle. Adapted from (RALLO et al., 2020; NEUBAUER, 2014; HARAM et al., 2021).

which most significantly contribute to the final cost are the battery characterization (discussed in more detail in Section 2.3.2), disassembling the pack into module, and disassembling the module into cells.

In a new battery pack, there already exists small variations in the capacity and internal impedance between cells; as the batteries age, the variance only grows (SCHUSTER; BRAND, et al., 2015; PAUL et al., 2013). This is problematic for second life applications, as module-to-module and cell-to-cell heterogeneity can put further stress in the healthier cells, leading to faster degradation. One solution involves sorting through the battery pack and separating the cells based on health indicators when reassembling a new energy storage system from retired cells (ZHU et al., 2021; MARTINEZ-LASERNA; SARASKETA-ZABALA, et al., 2018). Another – potentially complementary – solution is building a new battery pack based on a *SmartBattery* topology, which provides each cell with a dc/dc converter and controller to better manage the cell-to-cell differences (ARAUJO et al., 2019). Both of these solutions, however, requires dismantling the battery pack down to the cell, which is a labour intensive and expensive process. In fact, as per (RALLO et al., 2020), only the pack level of disassembly is potentially profitable (32€/kWh, compared to 60€/kWh when disassembled down to the module). This is an important issue if SLBs are ever going to be viable.

Part of the problem is the lack of standardization in the industry; with appropriate designs, some of the technical challenges associated with the remanufacturing process may be overcome (KAMPKER et al., 2021). There is additional hope for automating, in part or in full, parts of the disassembly process (ZHU et al., 2021; HARAM et al., 2021). In any case, both of these solutions would also be assisting in furthering and facilitating battery recycling, another big area of interest (HARPER et al., 2019). Currently, less than 5% of lithium-ion batteries are recycled, this is in contrast with a 99% recycling rates for lead-acid in the US and Europe (YANAMANDRA et al., 2022). This is in spite of the fact that end of life batteries do contain various precious metals and could be quite valuable. The recycling rate is expected to increase as the necessary infrastructure is built and as the regulations surrounding electric vehicles develop and go into effect (FCAB, 2021; COUNCIL OF EUROPEAN UNION, 2023).

2.3.2   Battery Diagnosis and Rest of Useful Life Estimation

Upon receiving a retired battery pack, it is important to diagnose it with regard to its State of Health (capacity, impedance, and other health metrics) before it can be used in a second life application. Firstly, not all cells are suitable for second life application, if lithium plating has already started forming, the battery should be put to recycling instead (MARTINEZ-LASERNA; SARASKETA-ZABALA, et al., 2018). Beyond that, identifying and sorting the modules and/or cells in accordance to their SoH is important; a heterogeneous battery pack has a more limited performance, degrades faster, and may be more unsafe (due to uneven heat distribution caused by differences in impedance, for example) (TANIM et al., 2020; RAN et al., 2020).

Battery diagnosis is a critical step of the End-of-Life assessment; it can be, however, very time consuming. In (RALLO et al., 2020), 'battery characterization' is the single most time-consuming step (one technician, 250 minutes). One way to minimize time spent on this step is for SoH data to be collected over the course of the battery lifetime and be made available to the repurposer. This idea is known as a "battery passport", a unique product identifier available digitally that would contain relevant information about the battery for various stakeholders. This would include information about the battery chemistry, cell geometry, information about the manufacturers and the supply chain, diagnostics and maintenance data, among other things. The European Union will require this kind of labelling starting on 2026 (BERGER; SCHÖGGL; BAUMGARTNER, 2022; COUNCIL OF EUROPEAN UNION, 2023).

A digital-twin is similar to a digital product passport but even more in-depth. It is a virtual representation (mathematical model or simulation) of a physical product which contains information about the original and is regularly updated. The virtual and physical objects are in constant communication, such that there is a bilateral interdependency between the two systems (JONES et al., 2020; BHATTI; MOHAN; SINGH, 2021). Measurements from the physical object are used to update the model; in return, the model is able to provide information such as SoH and Remaining Useful Life (RUL) estimates to the physical system, as well as – for example – be able to identify and predict need for maintenance in advance (BHATTI; MOHAN; SINGH, 2021; VITALLI; MOREIRA, 2023).

Typically, a digital-twin would be hosted remotely and be accessed through the cloud; in this position the model has access to more computating power, this enables more powerful and complex battery degradation models to be applied; additionally, the data collected is useful as a training data for a data-driven battery model (WU et al., 2020; BAUMANN; ROHR; LIENKAMP, 2018). The computing power available to the cloud could be further expanded by accessing the storage, communication and storage resources of the vehicles themselves while they are charging (a typical vehicle is parked 90% of the time) – this is known as vehicular edge-computing or cloud-computing (LIU et al., 2021; WHAIDUZZAMAN et al., 2014). There are, however, several privacy and security concerns with these approaches which go beyond the scope of this work.

2.3.2.1 SoH Estimation Methods

Battery diagnostic tests should be non-destructive, give insight about the internal electrochemical state of the cell and, ideally, be easily and quickly obtainable. Table 2.3 gives a summary of some SoH estimation methods – adapted from (QIAN et al., 2019). When assessing an aged cell, multiple parameters should be considered. Typically, the more information the better.

The two simplest SoH estimation methods are capacity and DC impedance measurement. A full characterization of both values can be done using Hybrid Pulse Power Characterization (HPPC) test; demonstrated in Figure 2.18(a) as per (CHRISTOPHERSEN, 2015). First, the battery is discharged until it reaches a reference minimum voltage; after an 1 hour rest period, it is charged at a C/3-rate until it reaches a reference maximum voltage – this step is used to determine

Table 2.3 – Parameters and methods used in references for SOH evaluation. Adapted from (QIAN et al., 2019)

Parameters/Methods	Feature
Capacity-based	Easy to obtain, simple evaluation
DC resistance (DCR)	Easy to obtain, simple evaluation
Area-specific impedance(ASI)	Easy to obtain, simple evaluation
AC impedance (EIS)	Hard to obtain, In-depth evaluation, expensive
Incremental capacity (dV/dQ)	Hard to obtain, In-depth evaluation, off-line
Differential voltage (dQ/dV)	Hard to obtain, In-depth evaluation, off-line

battery capacity through Coulomb counting. Then, after another 1 hour of rest, two short pulses are applied as per Figure 2.18(b). The first pulse is a 1 C-rate discharge pulse applied for a period of around 30 seconds; after a 30 second rest period, a smaller charge pulse (sometimes referred to as a "regen" pulse) is applied for around 10 seconds – note that this second pulse is not always applied. Following this, the battery then discharges until it reaches a 10% SoC interval at which point the systems rests and the process repeats itself (internal resistance varies with SoC). The DC resistance (alternatively known as pulse resistance) is calculated based on the current pulse measurements, as illustrated in (2.18), where V_0 and V_1 are the voltage measurements read at the start and at the end of the pulse and ΔI is the amplitude of the current step applied. Note that charge and discharge resistance may have difference values – which is why a charge and
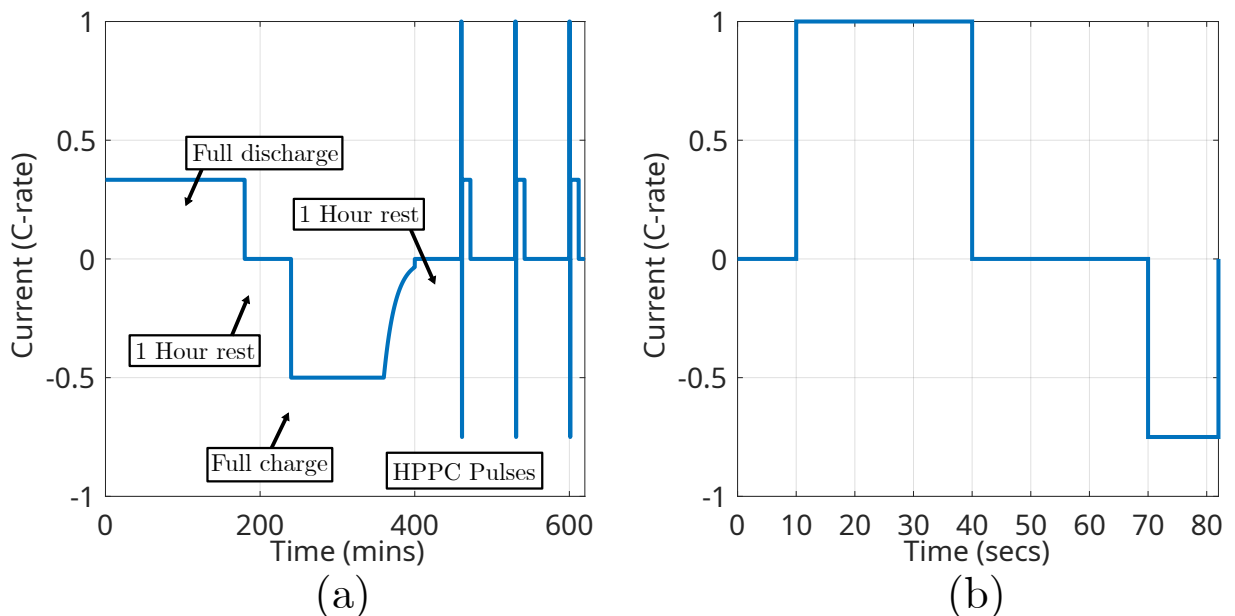
Figure 2.18 – HPPC Test current profile, adapted from (CHRISTOPHERSEN, 2015). a) Full test current profile. b) Charge and discharge pulses (repeated at every 10% SoC interval).

a discharge pulse are applied – and that resistance may also be dependent on amplitude of the current pulse due to the non-linear nature of battery systems.

$$R_{DC} = \frac{V_1 - V_0}{\Delta I} \tag{2.18}$$

Area-Specific Impedance (ASI) [Ωm^2] is another metric obtained from the HPPC test mentioned in Table 2.3; it can be obtained by multiplying the DC resistance R_{DC} with the electrode film surface (A [m^2]) as shown in (2.19). This is done because resistance is inversely proportional to electrode surface area which itself is proportional to total cell capacity, meaning ASI works as a correction factor which allows one to compare batteries of different geometries and capacities more fairly (GALLAGHER; NELSON; DEES, 2011).

$$R_{ASI} = R_{DC} \cdot A \tag{2.19}$$

The HPPC is a particularly thorough and slow assessment test for the battery – it may potentially last an entire day. This is largely due to the long rest periods between discharging the battery and doing a current pulse measurement. These pauses are necessary to allow the diffusion process to settle. The process can be shortened simply by measuring the impedance at fewer SoC values. Either way, both of these two measurements can be done *in-situ* using equipment available in a simple BMS. Allowing the BMS to occasionally do HPPC measurements over an extended rest period and making the results available to the repurposer could save time and simplify the EoL battery assessment.

Alternatively, (WAAG; KÄBITZ; SAUER, 2013) describes a slightly different method for measuring direct current resistance. A current pulse ΔI is applied for a period of ΔT (10s in this case), a line is drawn between the voltage value at end of the pulse and the half-way point. This line is extended until the start of the pulse and the voltage at that moment is used to calculate the resistance value. This process is represented in Figure 2.19(a) and in Equations (2.20) and (2.21). The aim of this technique is to remove the effect of the diffusion phenomenon such that the resulting resistance (R_d) more closely corresponds to the EIS resistance value at the transition point of the Warburg impedance (local minimum), shown in Figure 2.19(b). As a result, this resistance value has more physical significance: it is approximately the sum of the bulk (R_0), SEI (R_1) and charge-transfer (R_2) resistances. Additionally, this impedance measurement method can be used to detect lithium plating (KOLETI; DINH; MARCO, 2020). Typically R_d
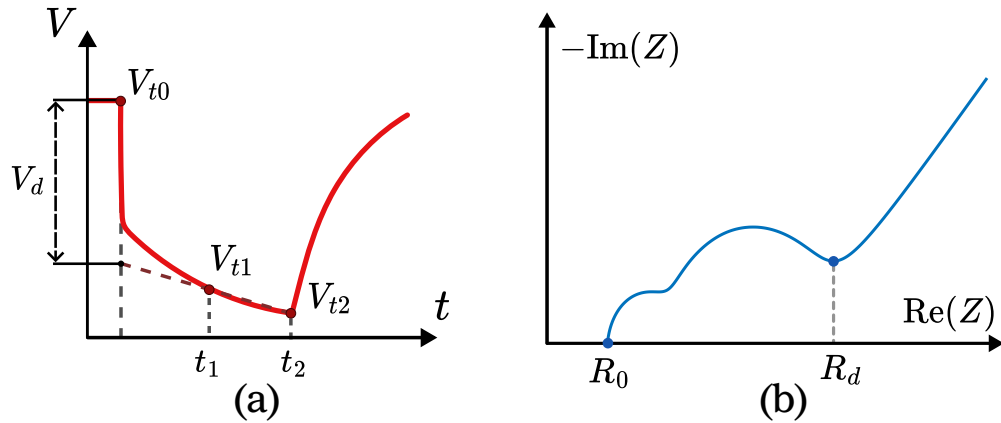
Figure 2.19 – a) Battery cell voltage response to current step and alternative algorithm for R_d using HPPC Pulse. b) Physical significance of R_d value as shown in an EIS plot. Adapted from (KOLETI; DINH; MARCO, 2020).

varies with SoC such that the graph forms an 'U' shape (minimum at around 50% SoC, grows as it approaches 0% and 100%), expect if there is lithium plating present, at which point the R_d values are depressed around the 100% SoC region, particularly at higher current values – shown in Figure 2.20 (KOLETI; DINH; MARCO, 2020).

$$V_d = V_{t2} - (t_2 - t_0) \cdot \frac{V_{t2} - V_{t1}}{t_2 - t_1} \tag{2.20}$$

$$R_d = \frac{V_d}{\Delta I} \tag{2.21}$$

Electrochemical Impedance Spectroscopy was previously discussed in Section 2.2.2.1. It is able to disaggregate the various internal electrochemical processes which occur at different
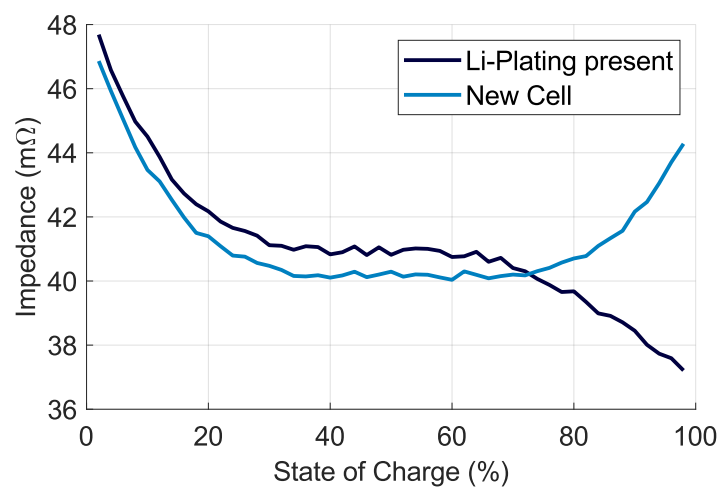
Figure 2.20 – Impedance R_d as a function of SoC with and without Li-Plating. This graph uses fictional values and should be considered for illustrative purposes only. Adapted from (KOLETI; DINH; MARCO, 2020)

frequency ranges, thus providing a much more detailed breakdown of internal battery dynamics than the more simplistic DC resistance measurement which is obtained through the HPPC test. To make an EIS measurement, a small amplitude AC signal is applied at various frequencies. An EIS spectrum with 60 frequency measurements over a range between 100kHz and 0.1Hz (ten frequencies per decade, distributed logarithmically) takes about 2-3 minutes (LAZANAS; PRODROMIDIS, 2023). This is the time required to make an EIS measurement at a single SoC value, it takes much longer to measure over many SoC values due to the necessity of resting between periods of charge and discharge (AZIZIGHALEHSARI et al., 2023) – the same problem as with the conventional HPPC test. The difficulty with EIS measurements is that they require specialized equipment. It is therefore a test that is usually only possible on a laboratory setting. There have been, however, proposals for estimating the EIS spectrum *in-situ* by using BMS voltage and current measurements obtained from regular operation – these methods would allow for the continuous monitoring of battery status throughout the battery lifecycle (GUHA; PATRA, 2018; BAUMANN; ROHR; LIENKAMP, 2018; KUIPERS et al., 2020; GONG et al., 2022).

Lastly, Incremental Capacity Analysis (ICA) and Differential Voltage Analysis (DVA) are two variations on the same test. The charge and discharge voltage is measured by applying a low rate current through the battery cell (the smaller the current, the closer the voltage profile is to equilibrium OCV), then using the measured voltage profile (V vs Q) to determine the IC ($\frac{dQ}{dV}$ vs V) or DV ($\frac{dV}{dQ}$ vs Q) curves (where Q is being used to represent throughput capacity in Ah), as seen in (2.22) and (2.23), respectively. This technique transforms the mostly smooth pseudo-OCV profile into more discernible peaks and valleys (DUBARRY; SVOBODA, et al., 2006; DUBARRY; ANSEÁN, 2022). In the case of ICA, peaks occur in regions where voltage plateaus and represents a chemically stable region. In the case of DVA, peaks occurs in regions of phase transition. Most analysis use ICA, as it can more easily be used to track degradation and has the advantage of having a stable x-axis as capacity decreases; DVA is better if one is measuring the potential of anode and cathode individually (by using a reference electrode) – in this situation, the resulting DVA curves are additive (BLOOM et al., 2005; DAHN et al., 2012). The rest of this explanation will focus on ICA.

$$\frac{dQ}{dV} \approx \frac{Q_2 - Q_1}{V_2 - V_1} \tag{2.22}$$

$$\frac{dV}{dQ} \approx \frac{V_2 - V_1}{Q_2 - Q_1} \tag{2.23}$$

The IC/DV tests are sensitive to temperature, electrical connection, and the calibration

and resolution of the voltmeter (ideally 1mV or lower). For best results, the test is conducted on a single cell (as opposed to a string of cells or a module), with a very low constant current – typically a rate less than C/10, ideally C/25; these characteristics make it a test more associated with a laboratory setting (DUBARRY; ANSEÁN, 2022; DUBARRY; BAURE, 2020). There have been attempts to translate this test into something that can be performed online by a BMS – particularly during charging (RIVIERE et al., 2019; KRUPP et al., 2020; WANG, L. et al., 2016). One of the main limitations is the charging rate used; it is possible to perform ICA with higher currents, though this alters the voltage curve due increased temperatures caused by higher currents and heterogeneities in the intercalation rate along the cell; this results in broader, distorted peaks which – nevertheless – may still be identifiable and useful, though it may require some filter and processing (CHEN, Y. et al., 2022).

The ICA profile of a given cell depends profoundly on the cell chemistry, each active material has its signature peaks and valleys at specific voltage values. Figure 2.21, originally from (DUBARRY; ANSEÁN, 2022), shows the half-cell IC profiles for various active materials, both positive and negative. The first step to analyze any full-cell ICA is to identify and index the peaks, in the case of a LFP/Graphite cell, Figure 2.22, there are five peaks in a new cell – peak 2 is tied to LFP (cathode active material) and peaks 1, 3, 4 and 5 are associated with the graphite
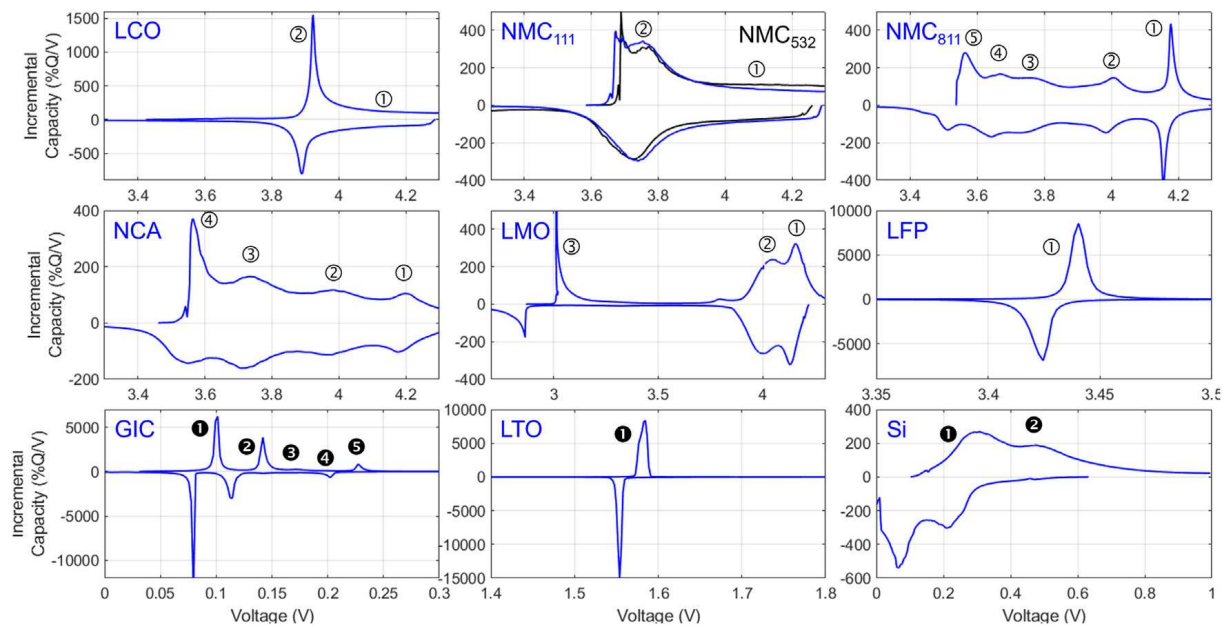
Figure 2.21 – Half-cell Incremental Capacity (measured for charge and discharge at C/25) for various cathode and anode active material. Figure originally from (DUBARRY; ANSEÁN, 2022)
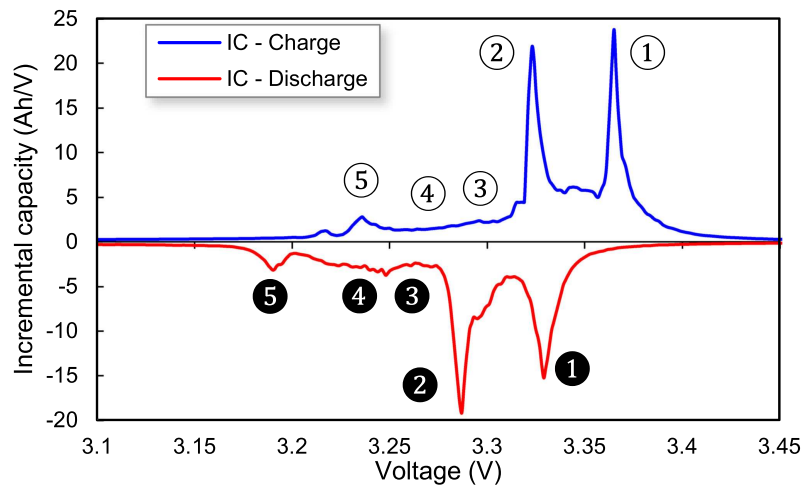
Figure 2.22 – Charge and Discharge incremental capacity for LFP-Graphite Cell, measured at C/25 C-rate. Figure originally from (ANSEÁN et al., 2019).

active (negative active material) (ANSEÁN et al., 2019). Each of these peaks is associated with a particular electrochemical phenomenon; in this sense, ICA is similar to EIS in its ability to provide insight into the internal state of the battery. As such, by tracking the change in the shape, position and area of each of these peaks as the battery ages, its possible to track degradation. Different degradation modes – LLI, LAM, ohmic resistance increase and lithium plating – each have different effects on the various peaks which can be identified (DUBARRY; SVOBODA, et al., 2006; ANSEÁN et al., 2019). New lithium plating formation – a form of degradation of particular interest for repurposing and second life applications – shows up in the ICA profile as a new, previously absent peak at high voltage values; this peak is evident particularly if the ICA is measure using higher charging currents (ANSEÁN et al., 2019; CHEN, Y. et al., 2022). Additionally, lithium-plating formation may also be detected by skipping the constant voltage step during charging and measuring the subsequent voltage relaxation DV ($\frac{dV}{dt}$) as the battery diffusion settles (CHEN, Y. et al., 2022).

2.4   Conclusions

Chapter 2 provided a broad overview of topics pertinent to Second-Life Batteries (SLBs), covering aspects from Electric Vehicle modeling in Section 2.1, to foundational discussions on lithium-ion batteries in Section 2.2, and more detailed considerations of SLBs themselves in Section 2.3. Building on this foundation, the dissertation will now narrow its focus to the simulation of batteries using physics-based models.

Chapter 3 delves deeper into these models, serving both as a literature review and a detailed examination of the internal electrochemical dynamics of batteries, as well as the mathematical models employed to represent these processes. This chapter extends and expands on what has already been said about battery fundamentals and physics-based models in Sections 2.2.1 and 2.2.3.

3 Physics-Based Battery Models

The physics-based battery models (alternatively known as electrochemical or mechanistic models) are the most complete and complex mathematical battery cell representations in the literature. This family of models explicitly attempts to represent the internal chemical state of the cell with a system of physically significant equations. These models are thus significantly more complex and computationally expensive than Equivalent Circuit Models and other simpler alternatives more common in Electrical Engineering. The upside is that these models, if properly calibrated, have the potential to be significantly more accurate than all other models, particularly in extreme conditions like high C-rates or extreme temperatures.

This section provides a brief introduction to these physics-based models. Section 3.1 discusses the basic Doyle-Fuller-Newman (DFN) model, which forms the foundation for most subsequent variants, including some simplified versions – discussed in Section 3.1.2. Section 3.2 explores various submodels that can be integrated with the basic battery model to simulate more complex behaviors – specifically degradation and internal heat generation.

3.1 Base Physical Model

As previously described in Section 2.2.1, batteries are composed of three primary regions: negative electrode (anode), separator, and positive electrode (cathode). Within both electrode regions, there is a 'solid-phase' (alternatively known as the 'active material') which serves as a deposit for lithium atoms. During discharge, lithium ions and free electrons are transferred from the anode to the cathode; the transport of lithium occurs within the cell (through the electrolyte and across the separator) while the transport of electrons occurs outside the cell – where they can be used to do useful work. The inverse of this movement occurs during charging. Figure 2.9 shows a schematic representation of the chemical phenomenon occurring within the cell during discharge and (2.14) shows the graphite (most common anode) reduction and oxidation (redox) reactions which enable the lithium intercalation and deintercalation processes.

3.1.1 Doyle-Fuller-Newman Model

The Doyle-Fuller-Newman model, originally described in (DOYLE; FULLER; NEW-MAN, 1993) and (FULLER; DOYLE; NEWMAN, 1994), is based on the porous electrode theory and concentrated solution theory – two models from electrochemistry which are used to describe the movement of charged particles dissolved in a liquid solution within a uniformly porous medium. It represents the internal volume of the battery as a homogeneous, porous mix of electrolyte and active material.

In this model, at any given moment, the internal macroscopic physical properties of the battery cell (eg. electrolyte lithium concentration c_e) are represented as a one dimensional set of continuum values which vary along the cell length – the x-axis – which extends between one current collector and other. The solid-phase, the electrode active material where the lithium is able to be deposited and held, is represented as microscopic spherical particles of radius $R_s^{\pm}$ (the average particle radius). At any given position x_i, it is assumed that all particles are the same, as if as there were only one per node. Intercalation and deintercalation, the process through which lithium binds and unbinds from the electrode material through the redox reactions, is represented using a 'transfer current' variable (lithium flow between electrode and electrolyte) and diffusion within these spheres along a microscopic r axis (movement within the electrode, between bulk and surface). As such, lithium concentration in the solid phase is the one variable which is modelled in two dimensions ($c_s(x, r)$). Given this, the DFN model is also sometimes called the Pseudo-2-dimensional (P2D) model. For the sake of brevity, the spatial and time dependencies of each variable will not be explicitly declared unless strictly necessary, meaning $c_s(t, x, r)$ will be written as c_s.

A simplified diagram of this model in shown in Figure 3.1 – adapted from (LEE; ONORI, 2021b).

Table 3.1 includes the fundamental equations that govern the DFN model, Table 3.2 lists and names all the symbols and variables. Sections 3.1.1.1 through 3.1.1.3 introduce each of these equations. For a full explanation of the model, see (DOYLE; FULLER; NEWMAN, 1993; FULLER; DOYLE; NEWMAN, 1994; NEWMAN; BALSARA, 2021; HARIHARAN; TAGADE; RAMACHANDRAN, 2018; THOMAS; NEWMAN; DARLING, 2002). Reference (RICHARDSON et al., 2022) is particularly good for beginners with no electrochemistry basis.

Table 3.1 – Doyle-Fuller-Newman model equations(SMITH; WANG, 2006; DOMENICO; STEFANOPOULOU; FIENGO, 2010; PRADA, 2012).

Name of mechanism	Equations		Boundary conditions and/or Complimentary equations	
Transfer current (Butler-Volmher rate)	$j_{tr} = a_s i_o \left(exp(\frac{\alpha_{ox}F}{RT}\eta) - exp(-\frac{\alpha_{red}F}{RT}\eta) \right)$	(DFN.1)	$i_o = i_o^{ref} \cdot c_e^{\alpha_{ox}} c_{ss}^{\alpha_{red}} (c_{s,max} - c_s)^{\alpha_{ox}}$ $\eta = \phi_s - \phi_e - U(c_{ss})$	(DFN.1a) (DFN.1b)
Solid phase charge conservation	$\frac{\partial}{\partial x}\left(\varepsilon_s \sigma \frac{\partial}{\partial x}\phi_s\right) = j_{tr}$	(DFN.2)	$\varepsilon_s \sigma \frac{\partial \phi_s}{\partial x}\big|_{x=0} = \varepsilon_s \sigma \frac{\partial \phi_s}{\partial x}\big|_{x=L} = -\frac{I}{A}$ $\frac{\partial \phi_s}{\partial x}\big|_{x=\delta_n} = \frac{\partial \phi_s}{\partial x}\big|_{x=\delta_{sp}} = 0$	(DFN.2a) (DFN.2b)
Electrolyte phase charge conservation	$\frac{\partial}{\partial x}\left(\kappa_e^{eff}\frac{\partial}{\partial x}\phi_e\right) = -\frac{\partial}{\partial x}\left(\kappa_D^{eff}\frac{\partial \ln(c_e)}{\partial x}\right) - j_{tr}$	(DFN.3)	$\frac{\partial \phi_e}{\partial x}\big|_{x=0} = \frac{\partial \phi_e}{\partial x}\big|_{x=L} = \phi_e(0) = 0$	(DFN.3a)
Solid phase Li^+ diffusion	$\frac{\partial}{\partial t}c_s = \frac{1}{r^2}\frac{\partial}{\partial r}\left(r^2 D_s \frac{\partial}{\partial r}c_s\right)$	(DFN.4)	$\frac{\partial c_s}{\partial r}\big|_{r=0} = 0$ $D_s \frac{\partial c_s}{\partial r}\big|_{r=R_s} = -\frac{j_{tr}}{\mathcal{F}a_s}$	(DFN.4a) (DFN.4b)
Electrolyte phase Li^+ diffusion	$\frac{\partial}{\partial t}\varepsilon_e c_e = \frac{\partial}{\partial x}\left(D_e^{eff}\frac{\partial}{\partial x}c_e\right) + \frac{1-t_+}{\mathcal{F}}j_{tr}$	(DFN.5)	$\frac{\partial c_e}{\partial x}\big|_{x=0} = \frac{\partial c_e}{\partial x}\big|_{x=L} = 0$	(DFN.5a)
Output voltage	$V = \phi_s(L) - \phi_s(0)$	(DFN.6)	-	
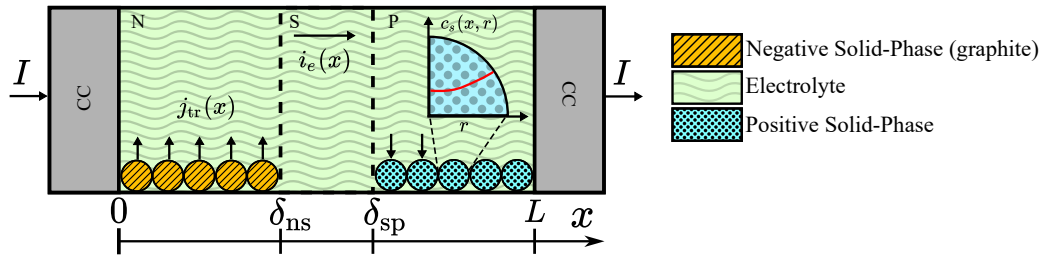
Figure 3.1 – Schematic of battery cell DFN model during discharge. Adapted from (LEE; ONORI, 2021b).

Table 3.2 – List of DFN model variables.

Symbol	Variable name	Unit
a_s	Active surface area	m^{-1}
A	Area of electrode	m^2
c_e	Concentration of lithium in the electrolyte	$mol \cdot m^{-3}$
c_s	Concentration of lithium in the solid phase	$mol \cdot m^{-3}$
c_{ss}	Concentration of lithium at the surface of solid phase	$mol \cdot m^{-3}$
D_e	Electrolyte phase diffusion coefficient	$m^2 \cdot s^{-1}$
D_s	Solid phase diffusion coefficient	$m^2 \cdot s^{-1}$
$\mathcal{F}$	Faraday's constant	$C \cdot mol^{-1}$
i_o	Exchange current density	$A \cdot m^{-2}$
I	Input current	A
j_{tr}	Transfer current per volume	$A \cdot m^{-3}$
L	Total cell length	m
r	Radial coordinate in the 1D model	m
R	Ideal gas constant	$J \cdot mol^{-1} \cdot K^{-1}$
R_s	Radius of spherical particles	m
t	Time	s
t_+	Li ion transference number	-
U	Half-cell Open Circuit Potential (OCP)	V
V	Cell voltage	V
x	Spatial coordinate in the 1D model	m
α	Charge transfer coefficient	-
δ	Length of individual electrodes and separator	m
ε_s	Volume fraction of the active material	-
ε_e	Volume fraction of the electrolyte/porosity	-
ε_s	Volume fraction of the filler	-
η	Electrode overpotential	V
κ	Ionic conductivity	$S \cdot m^{-1}$
ϕ	Electric potential of electrolyte of solid phase	V
σ	Solid phase conductivity	$S \cdot m^{-1}$

3.1.1.1 Transfer Current

The volumetric transfer current ($j_{tr}[A/m^3]$) in equation (DFN.1) represents the rate of the redox (reduction and oxidation) chemical reactions which allows for the intercalation and deintercalation of lithium ions into both negative and positive electrodes. In the DFN model, this dynamic is represented as a transfer current (j_{tr}) between solid and electrolyte phase currents (i_s and i_e). (RICHARDSON et al., 2022). Figure 3.2 exemplifies this phenomenon during discharge. When fully charged, lithium atoms are stored in the negative active material. As the battery cell discharges, lithium ions are released into the electrolyte (represented by electrolyte phase current, i_e) and free ions and released into the solid-phase and are eventually released externally through the current collector (solid-phase current, i_s).

This rate of the redox reaction is described with by the Butler-Volmer equation, which depends on overpotential (DFN.1b) – the difference between the voltage gap between solid-phase and electrolyte, and equilibrium potential (U) (DICKINSON; WAIN, 2020). Charge transfer rates α_{ox} and α_{red} determine the relative rates of the oxidation and reduction reaction, respectively responsible for the deintercalation and interlation in and out of the electrode solid-phases. In the case of a battery, these reactions are near symmetrical such that both terms can be assumed to be equal to $\alpha = 0.5$. With this assumption, the transfer current equation can be simplified as a hyperbolic sine ($e^x - e^{-x} = \sinh x$).

The transfer current value depends primarily on exchange current density (i_o), specific
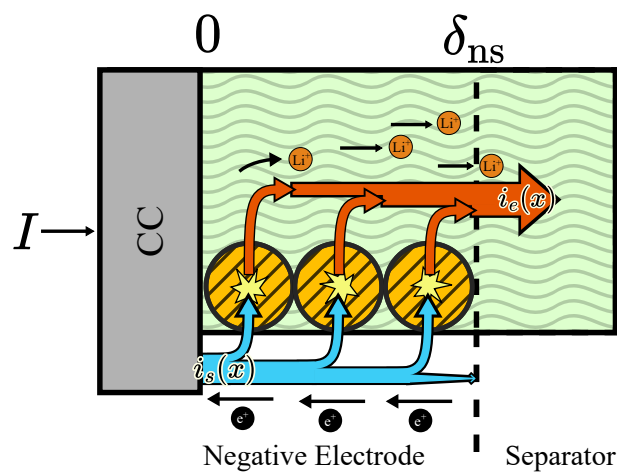
Figure 3.2 – Diagram representation of the process of lithium deintercalation (oxidation reaction) which releases a lithium ion previously deposited in the negative solid-phase into the electrolyte.

active surface area (a_s) and overpotential (η). The exchange current rate determines the rate of reaction and is tied mainly to lithium ion concentration in the solid and electrolyte phases. Active surface area relates the active particle surface over active particle volume, given a spherical particle of radius R_s, this is equal to (3.1). Overpotential – shown in (DFN.1b) – is the difference between the potential difference across an interface ($\phi_s - \phi_e$) and the half-cell OCP for the given electrode active material ($U^\pm$) – the former is an important property of the electrode active material, functions as the reaction equilibrium potential, each possible electrode chemistry has an unique voltage profile as a function of lithium concentration (MARQUIS, 2020; RICHARDSON et al., 2022).

$$a_s^\pm = \varepsilon_s^\pm \cdot \frac{3}{R_s^\pm} \tag{3.1}$$

3.1.1.2 Charge Conservation

The charge conservation equations (DFN.2) and (DFN.3) relate electric potential (voltage) in the solid and electrolyte mediums (ϕ_s and ϕ_e) to the volumetric transfer current described by (DFN.1). In the case of solid-phase potential (DFN.2), this relationship can be derived from (3.2a) and (3.2b). Where $i_s [A/m^2]$ is the current density in the electrode solid phase and $\sigma [S/m]$ is the solid phase conductivity.

$$i_s = -\sigma \varepsilon_s \cdot \frac{\partial}{\partial x} \phi_s \tag{3.2a}$$

$$j_{tr} = -\frac{\partial}{\partial x} i_s \tag{3.2b}$$

The charge conservation equation for the electrolyte (DFN.3) follows a similar logic with an additional term which depends on ionic concentration, c_e, to account for concentrated solution theory (RICHARDSON et al., 2022; NEWMAN; BALSARA, 2021). Notably, the electrolyte effective ionic conductivity (κ_e^{eff}) depends on electrolyte volume fraction (porosity) as described by (3.3). This is significant because one of the effects of degradation (discussed more in depth in Section 3.2.2) is the decrease of electrolyte volume share, which directly leads – as per (3.3) – to resistance increase.

$$\kappa_e^{\text{eff}} = \kappa_e \varepsilon_e^{Brugg} \tag{3.3}$$

Note that solid phase and electrolyte phase potentials are dependent on transfer current which is itself dependent on cell potential. This is one of many circular, non-linear relationships that have to be numerically solved through recursive methods at each time step of the simulation (HAN; TANG; RAHIMIAN, 2021).

3.1.1.3 Lithium-ion Diffusion

The mass conservation equations (DFN.4) and (DFN.5) describe the movement of lithium ions within the solid and electrolyte domains of the cell. This is an issue of great importance seeing as the movement of free lithium-ions between anode and cathode and vice-versa is the fundamental working principle of the battery cell; the thing that enables it to charge, store, and discharge energy.

One of the ways through which lithium concentration influences the macroscopic operation of the battery is with Half-cell OCP ($U^{\pm}$) – the equilibrium voltage of the intercalation reaction in (DFN.1). Each electrode material has a unique voltage profile as a function of surface lithium concentration which can be measured experimentally as demonstrated in (WANG, A. A. et al., 2022). Figure 3.3(a) shows the half-cell open circuit potentials for a NMC/Graphite-Silicon battery, Figure 3.3(b) show resulting Open-Circtuit Voltage for the full cell given the combination of these two half-cells (CHEN, C.-H. et al., 2020).

The reason why these half-cell OCPs have such a big impact on over-all output voltage can be derived from (DFN.1b). Typically, both overpotential η and electrolyte potential ϕ_e are rather small (particularly if applied current is low). Given that, (DFN.1b) can be approximated as (3.4). This itself can be combined with (DFN.6) and rearranged to show that (3.5). This is an important conclusion which will later be used to derive a simplified variant of the DFN model in Section 3.1.2.2.

$$\phi_s \approx U(c_{ss}) \tag{3.4}$$

$$V \approx U^+(c_{ss}(L)) - U^-(c_{ss}(0)) \tag{3.5}$$

For both solid-phase and electrolyte cases, the diffusion dynamics are described using "Fick's laws of diffusion". These are expressed as second-order partial differential equations of the format: "$\dot{u} = D \cdot \nabla^2 u$" applied to a one dimensional space (r-axis for solid-phase, x-axis for electrolyte phase) (LI; CHEN, 2008). This same equation structure is used to define the heat equation. With fickian dynamics, the total amount of (in this case) lithium atoms in a volume changes solely as a function of the boundary conditions; such that, if the boundary conditions are zero, total lithium in the system remains constant and the concentration tends to homogenize overtime. This dynamic is not preserved in the electrolyte phase diffusion case (DFN.5) due to the inclusion of an additional terms that depends on volumetric transfer current (j_{tr}) – effectively
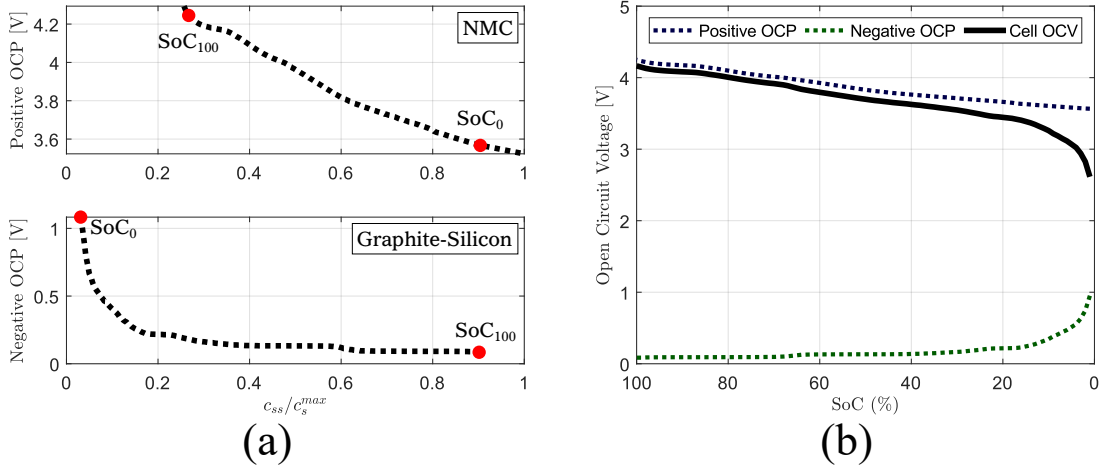
Figure 3.3 – Battery electric potential. a) OCP for each of the individuals half-cells for a NCM/Graphite-Silicon battery as a function of lithium concentration; b) Full cell Open-Circuit Voltage. Adapted from (CHEN, C.-H. et al., 2020).

a form of 'generation'. The equation for solid-phase diffusion (DFN.4) might be unfamiliar due to it being expressed in a system of spherical coordinates, but given that solid-phase diffusion D_s is constant throughtout the particle, this equation can be rewritten as (3.6), which is more easily discernible and computable (LI; CHEN, 2008; DOMENICO; STEFANOPOULOU; FIENGO, 2010). Note also that for solid-phase diffusion, electrode surface boundary conditions (DFN.4b) depend on transfer current j_{tr}.

$$\frac{\partial}{\partial t}c_s = D_s \left(\frac{\partial^2}{\partial r^2}c_s + \frac{2}{r}\frac{\partial}{\partial r}c_s \right) \tag{3.6}$$

3.1.2 Simplified Models

The DFN model is a widely used model within academia, it manages to remain accurate even in situations of high C-rate and/or extreme temperatures. Its biggest disadvantage is its complexity, both in terms of parametization and computational requirements.

In terms of parameters, there are as many as 35 parameter needed to simulate a full DFN model (CHEN, C.-H. et al., 2020). Further complicating things, many of these values are functions dependent on other variables such as temperature T and lithium concentration c_e and c_{ss}. The independent measurement of all these parameters is a laborious and expensive process which requires specific equipment and the destruction of the cell in question (CHEN, C.-H. et al., 2020; WANG, A. A. et al., 2022). Thankfully, a lot of these variables refer to physical properties which, once measured, should be true of all cells – or at least of all cells of a certain chemistry. By limiting the number of unknowns, less estimation and measurements are required

to characterize a cell. For this reason, there is at least one database which attempts to log battery model parameters from across the scientific literature – though it is a limited database and in no way an exhaustive list (WANG, A. A. et al., 2022; WANG; SULZER, 2021).

Additionally, calculating the numerical solution for the DFN model can take a long time for each time-step, which can be a challenge for certain applications, particularly Battery Management Systems (BMS) (SUBRAMANIAN; DIWAKAR; TAPRIYAL, 2005; JIN, 2022). Due to these complications, it is often more appropriate to use a simplified approximated model.

3.1.2.1 Simplified Solid-Phase Diffusion

The DFN model is made up of a system of interconnected differential and algebraic equations, listed on Table 3.1. The typical way to solve these system of Partial Differential Equations (PDEs) is to discretize the space in accordance to the Finite Elements Method, Finite Differences Method, Finite Volume Method – or some other – and replace the PDEs with a series of Ordinal Differential Equations (ODEs) or Differential Algebraic Equations (DAEs) which are easier to solve (LI; CHEN, 2008). In the case of lithium ion diffusion within the electrode solid-phase, shown in equation (DFN.4) and explained in greater detail in Section 3.1.1.3, the r-axis needs to be discretized. However, in the DFN model, it is as if there is one spherical particle within every node in the x-axis. This causes the number of ODEs tied to the solid phase dynamics to grow multiplicative, proportional to both the number x-axis and r-axis nodes – this is the two-dimensional nature of solid-phase lithium diffusion.

Though computational complexity related to lithium diffusion grows quickly, it is not particularly beneficial. Macroscopic cell behaviour depends only on the concentration at the electrode surface, the concentration values in $r < R_s^\pm$ range are not of particular importance. One approach to simplify the diffusion model proposed by (SUBRAMANIAN; DIWAKAR; TAPRIYAL, 2005) is to assume a polynomial distribution of concentration in the r-axis. Two models are presented, the low order polynomial (LOP) assumes a quadratic polynomial and the high order polynomial (HOP) assumes a quartic polynomial.

- Low order polynomial $c(t,r) = a(t) + b(t)\frac{r^2}{R_s^2}$

$$\frac{\partial}{\partial t}\bar{c}_s = -\frac{3}{R_s}\frac{j_{tr}}{a_s\mathcal{F}} \tag{3.7a}$$

$$c_{ss} = \bar{c}_s - \frac{R_s}{5D_s}\frac{j_{tr}}{\mathcal{F}a_s} \tag{3.7b}$$

- High order polynomial $c(t, r) = a(t) + b(t)\frac{r^2}{R_s^2} + d(t)\frac{r^4}{R_s^4}$

$$\frac{\partial}{\partial t}\bar{c}_s = -\frac{3}{R_s}\frac{j_{tr}}{a_s\mathcal{F}} \tag{3.8a}$$

$$\frac{\partial}{\partial t}q = -30\frac{D_s}{R_s^2}q - \frac{45}{2R_s^2}\frac{j_{tr}}{\mathcal{F}a_s} \tag{3.8b}$$

$$c_{ss} = \bar{c}_s + \frac{8R_s}{35}q - \frac{R_s}{35D_s}\frac{j_{tr}}{\mathcal{F}a_s} \tag{3.8c}$$

Where $\bar{c}_s$ is the volume-averaged concentration, c_{ss} is the surface concentration, and q is the volume-averaged concentration flux.

The simplified model eliminates the need to model the r-axis and replaces the diffusion dynamics from equation (DFN.4) with a significant simpler model described by equations (3.7) and (3.8). According to (SUBRAMANIAN; DIWAKAR; TAPRIYAL, 2005), these two approaches managed to save 80% to 90% of the time to solve the simulation when compared to the full P2D model (ZHANG; WHITE, 2007). Both approaches are reasonably accurate though typically fail to capture transient behaviour at high currents. The LOP is accurate up to around 2 C-rate while the HOP is accurate up to around 5 C-rate (TORCHIO et al., 2016). To achieve accuracy at higher currents, one could derive polynomial approximations of even higher orders by extending the approach described in (SUBRAMANIAN; RITTER; WHITE, 2001; SUBRAMANIAN; DIWAKAR; TAPRIYAL, 2005) or implementing alternative more advanced methods like the ones seen in (RAMADESIGAN et al., 2010).

3.1.2.2 Single Particle Model

The Single Particle Model (SPM), depicted in Fig 3.4, is a commonly used simplified version of the DFN model (SANTHANAGOPALAN et al., 2006; GUO; SIKHA; WHITE, 2010; NING; POPOV, 2004). It is based on the premise that the solid phase within each of the electrodes is uniform, meaning that, instead of simulating the lithium solid-phase diffusion in every node of a discretized x-axis, only a single spherical particle per phase is simulated. It is the insight from the (3.5) approximation expanded.

One of the big advantages of SPM models is that instead of arriving at the value of transfer current j_{tr} at every node in x recursively, it is only a single value per phase and it can be calculated deterministically. Transfer current boundary equations (DFN.1a) and (DFN.1b), in addition to equation (3.2), indicate that solid-phase current (i_s) is directly proportional to applied current (I) in the two extremes of the battery (at x=0 and x=L) and is equal to zero in edges of
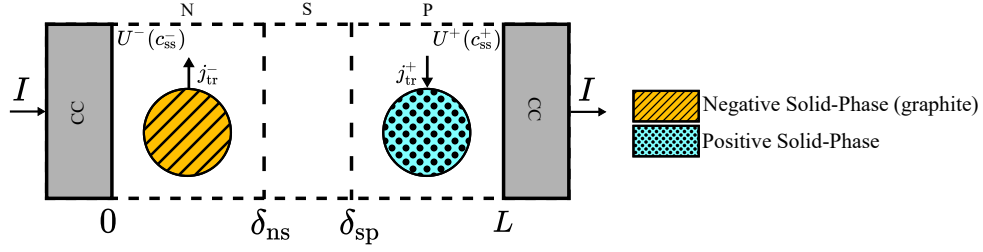
Figure 3.4 – Single Particle Model schematic.

the separator. Combining this insight with (3.2b), which relates transfer current and solid-phase current, one can obtain (3.9). From that, transfer current for both electrode phases $j_{tr}^{\pm}$ can be calculated as a function of applied current using (3.10) (PRADA, 2012).

$$\int_0^{\delta_n} j_{tr}(x)dx = \frac{I}{A} \tag{3.9a}$$

$$\int_{\delta_{sp}}^{L} j_{tr}(x)dx = -\frac{I}{A} \tag{3.9b}$$

$$j_{tr}^- = \frac{I}{A\delta^-} \tag{3.10a}$$

$$j_{tr}^+ = \frac{-I}{A\delta^+} \tag{3.10b}$$

In the SPM model, the equation for cell output voltage is given by combining the DFN voltage equation (DFN.6) and the overvoltage equation (DFN.1) such that:

$$V = \overbrace{(U^+ + \phi_e(L) + \eta^+)}^{\phi_s^+} - \overbrace{(U^- + \phi_e(0) + \eta^-)}^{\phi_s^-} \tag{3.11a}$$

$$V = \Delta U + \Delta\phi_e + \Delta\eta \tag{3.11b}$$

The half-cell open circuit potentials $U^{\pm}$ are the dominant terms in equations (3.11). As before, these depend on surface concentration $c_{ss}^{\pm}$.

The kinetic overpotential $\eta^{\pm}$ can be expressed as a function of transfer current:

$$\eta^{\pm} = \frac{RT}{\alpha\mathcal{F}} \cdot \text{arcsinh}\left(\frac{j_{tr}^{\pm}}{2a_s^{\pm}i_o^{\pm}}\right) \tag{3.12}$$

The term $i_o^{\pm}$ is the exchange current and depends on lithium concentration in the electrolyte and particle surface – as shown in (DFN.1a). In an SP model, this variable is either made to be only dependent on surface concentration or is considered as a constant for simplicity sake.

The electrolyte potential difference $\Delta\phi_e$ is equal to:

$$\Delta\phi_e = (1 - t_+)\frac{2RT}{\mathcal{F}} \ln \frac{c_e(L)}{c_e(0)} - IR_e \tag{3.13}$$

The first term of equation (3.13) depends on the lithium distribution within the electrolyte c_e. The basic SPM does not model lithium transport in the electrolyte as described by (DFN.5). Rather this value is assumed to be uniform and constant – this is a reasonable approximation for currents up to 1 C-rate. There is a subset of Single Particle Models which do account for the electrolyte dynamics known as SPMe. These models are accurate to currents up to 2 C-rate (PRADA, 2012; PRADA et al., 2013; MOURA et al., 2016; ALLAM; ONORI, 2018).

The second term contains a term proportional to electrolyte resistance, which is a term depends on effective electrolyte conductivity κ_e – given by (3.3), electrode length δ_j and cell area A as stated in equation (3.14) (PRADA, 2012; PRADA et al., 2013)

$$R_e = \frac{1}{2A} \left(\frac{\delta^-}{\kappa_{e-}^{\text{eff}}} + 2\frac{\delta^s}{\kappa_{es}^{\text{eff}}} + \frac{\delta^+}{\kappa_{e+}^{\text{eff}}} \right) \tag{3.14}$$

3.2 Complementary Submodels

The original DFN model (DOYLE; FULLER; NEWMAN, 1993) does not account for capacity degradation or heat generation from the battery. To better represent these dynamics, it is necessary to modify the base model with additional equations and parameters.

3.2.1 Thermal model

Many of the electrochemical processes and reactions that take place within the battery are sensitive to temperature changes. This is particularly true for degradation mechanisms, for which temperature is one of the most significant stress factors (EDGE et al., 2021). (WALDMANN et al., 2014) studies battery degradation for temperatures between -20^oC and 70^oC and identifies increased aging rates for temperatures above and below 25^oC.

The reaction rate dependence on temperature can be represented by the Arrhenius equation (3.15). Here, Ψ is a generic variable which represents a particular temperature dependent parameter, $E_a^\Psi \ [J/mol]$ is the activation energy for the given parameter. A lot of variables can be described using the arrhenius equation template, these include: electrolyte and solid phase diffusivity (D_e and D_s), electrolyte conductivity κ_e, intercalation reaction rate (i_o^{ref}), among

others (MARQUIS, 2020).

$$\Psi = \Psi_{\text{ref}} \cdot \exp\left(\frac{E_a^{\Psi}}{R} \cdot \left(\frac{1}{T_{ref}} - \frac{1}{T}\right)\right) \tag{3.15}$$

Temperature additionally has an effect on the Open Circuit Potential of each of the electrodes as presented by (3.16). The entropic potential ($\partial U/\partial T$) is typically measured experimentally as a function of surface lithium concentration (c_{ss}) for a fixed temperature (GU; MALYSZ, et al., 2016; BAEK et al., 2022). Note that the effect that entropic potential has on output voltage is typically small, in the order of a $0.1mV/K$, and can often be disregarded.

$$U(c_{ss}, T) = U_{\text{ref}}(c_{ss}) + (T - T_{ref})\frac{\partial U(c_{ss})}{\partial T}\bigg|_{T=T_{ref}} \tag{3.16}$$

The simplest possible thermal model is isothermal. It assumes that there is no internal heat generation such that cell temperature always matches ambient temperature. In situations with higher currents or when heat dissipation is constrained, generation can be a significant factor in overall temperature. The simplest model which corrects for these limitation is the so called "lumped model". It represents cell temperature as being uniform along the entire cell and from ambient temperature due to internal heat generation and heat transmission with the environment. Both of which are explicitly modelled (3.17).

$$MC_p\frac{\partial T}{\partial t} = Q - hA_c(T - T_{amb}) \tag{3.17}$$

In Equation (3.17); Q represents the heat generated within the battery (W); M and C_p are the cells mass (kg) and heat capacity ($J/_{kg \cdot K}$), respectively. Variables A_c and h are the cells external surface area exposed to cooling (m^2) and its thermal convective coefficient ($W/_{m^2 \cdot K}$), respectively (PRADA, 2012). Note that h depends on the form of cooling employed, it can range from $5 - 10$ if the cell is subject to free convection air cooling, $10 - 70$ for forced air cooling, and over 100 with liquid cooling (PRADA, 2012).

Internal heat generation Q can be broken down into four component parts: ohmic heating, reaction heating, reversible/entropic heating, and contact/current collector heating. In a DFN model, these can be represented as shown in eq (3.18)(SMITH; WANG, 2006; SRINIVASAN; WANG, 2002; FANG; KWON; WANG, 2010).

$$Q = Q_{\text{ohm}} + Q_{\text{rea}} + Q_{\text{ent}} + Q_{\text{cc}} \tag{3.18a}$$

$$Q_{\text{ohm}} = A \int_0^L \sigma^{\text{eff}} \left(\frac{\partial \phi_s}{\partial x}\right)^2 + \kappa^{\text{eff}} \left(\frac{\partial \phi_e}{\partial x}\right)^2 + \kappa_D^{\text{eff}} \left(\frac{\partial ln(c_e)}{\partial x} \cdot \frac{\partial \phi_e}{\partial x}\right) dx \tag{3.18b}$$

$$Q_{\text{rea}} = A \int_0^L j_T (\phi_s - \phi_e - U) dx \tag{3.18c}$$

$$Q_{\text{ent}} = A \int_0^L j_T T \frac{\partial U}{\partial T}(c_{ss}) dx \tag{3.18d}$$

$$Q_{\text{cc}} = I^2 \cdot R_{cc} \tag{3.18e}$$

The contribution of Q_{ent} is typically small, such that it can be disregarded by approximating $\partial U / \partial T = 0$ (FORGEZ et al., 2010). This model can be greatly simplified by assuming the OCP terms are constant along the x-axis and that the transfer current reaction rates are spatially uniform. Given these assumptions, Q can be rewritten as shown in equation (3.19). Here, U_{avg}^j is the average OCP and I_T^j is the total transfer current within each of the j electrodes, where $j \in \{+, -\}$(GU; WANG, 2000; RAO; NEWMAN, 1997).

$$Q = \sum^j \left(I_T^j \cdot (U_{\text{avg}}^j - T \frac{\partial U_{\text{avg}}^j}{\partial T}) \right) - IV \tag{3.19a}$$

$$I_T^j = A \int_{\Delta L_j} j_T(x) dx \tag{3.19b}$$

In a Single-Particle Model, the heat generation equation (3.19) is further simplified as shown in (3.20)(PRADA, 2012).

$$Q = \left((V - U^+ - U^-)I + \frac{\partial (U^+ - U^-)}{\partial T} I \right) \tag{3.20}$$

Beyond the lumped thermal model, there are more complex models which account for uneven distributions of temperature within the cell. This is important when modelling for thermal runaway, which is triggered by the hottest point in the cell (GU; WANG, 2000). Any model which aims to account for temperature distribution within a cell is necessarily dependent on the particular cell geometry; for lithium cells, the two most common types are 'Pouch cells' and 'Cylindrical cells'.

In both cases, the DFN model x-axis is too thin to contain any significant temperature gradients. For pouch cells, its more worth modelling temperature along height and length

$(T(t, y, z))$, and for cylindrical cells, temperature is modelled relative to cylinder radius and height $(T(t, r_c, y))$.

These models are naturally more complex and outside the scope of this work. For more on distributional thermal models, references (MARQUIS, 2020; XU et al., 2015) and (TIMMS et al., 2021) discuss pouch cell models and references (FORGEZ et al., 2010), and (ZHANG, 2011) discuss cylindrical models.

3.2.2 Degradation Model

Within the cell, there are undesired side-reactions which decrease available lithium and increase internal resistance. Over many cycles, the cumulative effect of these reactions leads to capacity fade and impedance increase, in addition to other effects. Typically, the metric used to track capacity degradation is 'State of Health' (SoH), it measures current capacity $Q(t)$ as a fraction of nominal capacity Q_{nom}.

The typical life-cycle of a battery, illustrated by the graph in Figure 2.16, starts with accelerated capacity degradation for the first few cycles as a initial layer of Solid Electrolyte Interface (SEI) builds on top the surface of the negative solid phase. After this initial build-up, capacity continues to decrease at a slower but constant rate. This phase of linear degradation lasts for most of the batteries life-cycle. Once the SoH reaches 80%, the battery is typically deemed to be at its End of Life (EoL), though realistically it still can be reused in a Second Life scenario with a less intensive duty-cycle. The linear, SEI growth dominated capacity fade continues past the 80% SoH mark, up until the transition from linear to non-linear capacity degradation – the so called 'knee-point'(HU; DENG, et al., 2022). Continued use past the knee-point is highly discouraged as it presents rapid capacity loss and increased risk of short-circuit or thermal runaway, a significant safety risk. Studies that have disassembled batteries past the aging knee-point reveal a layer of solid lithium metal within the negative electrode, especially near the separator interface (YANG et al., 2017; BROUSSELY et al., 2005; KLETT; ERIKSSON, et al., 2014; KLETT; SVENS, et al., 2015; SCHUSTER; BACH, et al., 2015). Accurate modelling of degradation mechanisms is thus important to estimate Remaining Useful Life (RUL), especially for Second Life Batteries (SLB) (HU; DENG, et al., 2022).

This work focuses on the degradation mechanisms included in the (YANG et al., 2017) model which is able to model the linear to non-linear transition as shown in Figure 3.5 by
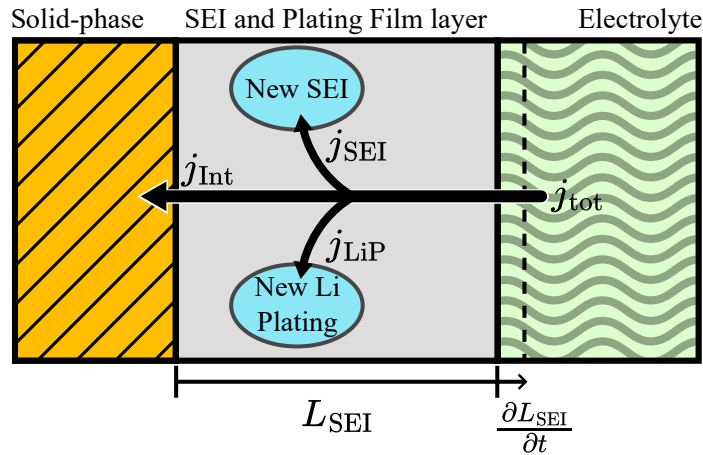
Figure 3.5 – Volumetric current being used for intercalation and side-reactions. Adapted from (YANG et al., 2017)

modelling SEI growth, pore-clogging and lithium plating. Initially, SEI growth is the dominant degradation mechanism, as it grows, it consumes cyclable lithium which becomes unavailable for future redox reactions (loss of capacity). SEI growth also causes porosity (ε_e) to decrease in a process known as 'pore-clogging'. This in turn results in greater anode electrolyte resistivity, a more significant electrolyte potential drop within the anode, and, eventually, significantly faster lithium-plating – particularly near the negative-separator interface (BROUSSELY et al., 2005). This feedback loop eventually leads to non-linear accelerated growth. During this final stage of the batteries life, Li-plating is the dominant degradation factor.

Although SEI growth and Li-plating are understood to be the leading causes of battery aging, there are other phenomena which contribute to degradation and impedance growth which are unaccounted for in the Yang model; for example particle cracking and solid phase disillusion. (RENIERS; MULDER; HOWEY, 2019) reviews and compares various degradation mechanisms and models; it also studies the emergent behaviour derived from the interaction of two or more of these models being run in parallel. A battery model which accounts for more degradation processes should be able to better capture the path-dependent nature of battery degradation; which is to say, it will better reflect how different degradation dynamics and paths will be more or less prominent for different usage patterns. Additional degradation models creates possibilities for more feedback loops and alternative degradation paths (DUBARRY; BAURE; DEVIE, 2018; RAJ et al., 2020; EDGE et al., 2021).

3.2.2.1 SEI Growth

The Solid Electrolyte Interface is a layer of organic material that forms on the surface of the negative electrode. It is the result of a chemical reaction between lithium ions, electrons, and the electrolyte solvent Ethylene Carbonate (*EC*) as shown in (3.21).

$$2\overbrace{C_2H_4CO_3}^{EC} + 2Li^+ + 2e^- \rightarrow (CH_2OCO_2Li)_2 + C_2H_4 \tag{3.21}$$

This reaction occurs in the interface between the solid-phase and electrolyte, alongside the intercalation transformation. The reaction kinetics is represented by the volumetric current density $j_{SEI}[A/m^3]$, which serves as a measure of the lithium-ions being consumed by the reaction (3.21) and being deposited into the SEI film. The growth of the film layer is proportional to current density j_{SEI} and partial molar volume $V_{SEI}[m^3/mol]$ as described in equation (3.22); where $L_{SEI}[m]$ is the thickness of the SEI film.

$$\frac{d}{dt}L_{SEI} = -V_{SEI}\frac{j_{SEI}}{\mathcal{F}a_s} \tag{3.22}$$

As the SEI film grows, cyclable lithium from the negative electrode is deposited within the SEI layer and is lost – this is a form of capacity degradation known as Loss of Lithium Inventory (LLI). In this case, the negative electrode loses lithium relative to the positive side such that both concentrations become out of phase. This particular kind of LLI is called stoichiometric drift and is shown in Figure 3.6.
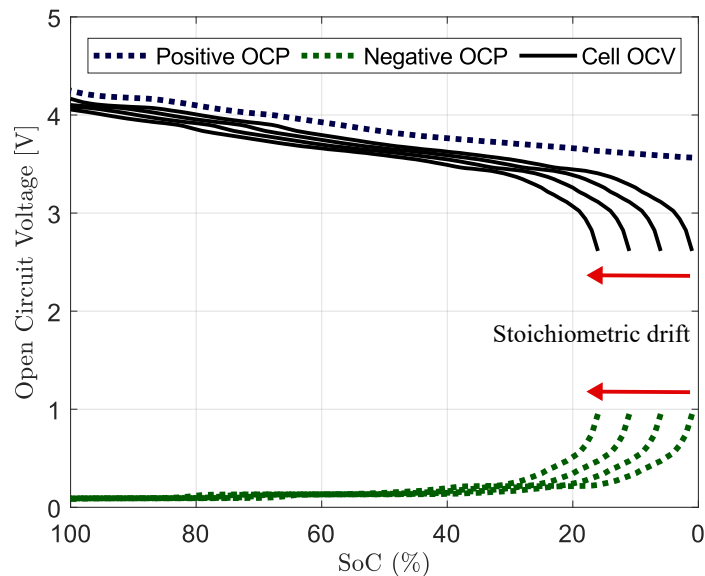
Figure 3.6 – Effect of loss of lithium inventory on open-circuit voltage.

The SEI films represents a source of resistance for the process of intercalation. This is modelled by rewritting the overpotential equation (DFN.1) as (3.23). Here, R_{film} represents the film resistivity, given by (3.24). It depends on SEI and solid lithium layer lengths L and conductivity κ. The volumetric current density j_{T} is the total transfer current and it includes the intercalation, SEI reaction and the plating reaction currents $j_{\text{T}} = j_{\text{int}} + j_{\text{SEI}} + j_{\text{pl}}$, as seen in Figure 3.5. The increase of charge transfer resistance contributes to the overall battery impedance rise, though it is less significant than the rise of the electrolyte resistance within the negative electrode region due to the decrease in anode porosity – which is the dominant cause of resistance rise.

The growth of the SEI film additionally leads to a decreased in the electrolyte porosity (ε_e) as described by (3.25).

$$\eta_{\text{int}} = \phi_s - \phi_e - U_{\text{int}} - \frac{j_{\text{T}}}{a} R_{\text{film}} \tag{3.23}$$

$$r_{\text{film}} = \frac{L_{\text{SEI}}}{\kappa_{\text{SEI}}} + \frac{L_{\text{Pl}}}{\kappa_{\text{Pl}}} \tag{3.24}$$

$$\frac{d}{dt}\varepsilon_e = -a_s \frac{d}{dt}(L_{\text{SEI}} + L_{\text{Pl}}) \tag{3.25}$$

The SEI growth reaction (3.21) is a multi-step process with multiple moving component (lithium ions, electrons, EC solvent). In the context of modelling, the rate of reaction can only ever be as fast as the rate limiting step. However, there is no consensus as to what is the rate determining step for SEI growth. In (RENIERS; MULDER; HOWEY, 2019), the researchers focus on three approaches: kinetically limited, solvent diffusion limited, and electron tunnelling. Respectively, these models are limited by reaction kinetics as described by a Tafel equation, which is to say, exponential relative to overpotential; transport of EC solvent from electrolyte to solid phase surface through SEI film; and transport of electrons from solid-phase surface to electrolyte through SEI film – respectively.

The (YANG et al., 2017) model uses a simplified version of the SEI growth model presented in (SAFARI et al., 2008). This model is both kinetically and solvent transport limited. Equation (3.26) shows a Tafel equation that directly describes the reaction kinetics; k_{s0} is a fitting variable, c_{EC}^s represents the concentration of the EC solvent on the solid-phase surface, η_{SEI} is the overpotential for the SEI equation, where U_{SEI} is the equilibrium potential for this specific reaction (the voltage difference ΔV between solid-phase and electrolyte such that there is no reaction, no current). Equation (3.27) describes the transport of EC solvent within the SEI film along the r-axis, between $r = R$ (the solid-phase surface) and $r = R + L_{SEI}$ (the SEI-electrolyte

interface); the term ν is the SEI film velocity, which is equal to the rate of SEI layer growth $\nu = \partial L_{SEI}/\partial t$, and c_{EC}^0 is the bulk electrolyte concentration in the electrolyte.

$$j_{\text{SEI}} = -\mathcal{F}k_{s0}c_{EC}^s \times \exp\left(-\frac{\beta_s \mathcal{F}}{RT}(\eta_{\text{SEI}} - \frac{R_{\text{film}}}{a_s}j_T)\right) \tag{3.26a}$$

$$\eta_{\text{SEI}} = \phi_s - \phi_e - U - U_{SEI} \tag{3.26b}$$

$$\frac{\partial c_{EC}}{\partial t} = D_{EC}\frac{\partial^2 c_{EC}}{\partial r^2} - \nu\frac{\partial c_{EC}}{\partial r} \tag{3.27a}$$

$$D_{EC}\frac{\partial c_{EC}}{\partial r}\Big|_{r=R} = \frac{j_{SEI}}{\mathcal{F}} - \nu \cdot c_{EC}(R) \tag{3.27b}$$

$$c_{EC}(R + L_{SEI}) = K_{EC} \cdot c_{EC}^0 \tag{3.27c}$$

The disadvantage of the Safari approach is that its a continuum model, meaning that EC solvent concentration diffusion would have to be actively simulated in the r-axis, between the range of $r = R_s$ and $r = R_s + L_{\text{SEI}}$. Simulating on axis that changes size is particularly computationally complex. Ideally one would prefer zero-dimensional models, models which do not rely on variables which vary continously over a dimensional range (MARQUIS, 2020).

(SINGLE; LATZ; HORSTMANN, 2018) reviews and compares four zero-dimensional models in order to identify which of these most accurately replicates the long-term degradation patterns. Each of these models considered a different limiting factor, these are: solvent-diffusion, electron tunnelling, electron conduction and interstitial lithium diffusion. The work finds that both the electron tunnelling and the solvent diffusion models are unlikely to be the long-term degradation mechanisms, it concludes that the interstitial lithium diffusion limited model – which posits that neutral lithium atoms travel from the electrode to the electrolyte where they react with solvent – is the best match for the experimental data available. This model takes the form shown in (3.28) (MARQUIS, 2020). Marquis (MARQUIS, 2020) arrives at a similar formulation for zero-dimensional growth model independently.

$$j_{\text{SEI}} = -\frac{\mathcal{F}D_{Lii}}{L_{SEI}}c_{Lii}^0 \exp\left(-\frac{\mathcal{F}}{RT}(\phi_s - \phi_e)\right) \tag{3.28}$$

3.2.2.2 Li-Plating

Lithium plating refers to the process where metallic lithium is deposited on the surface of the negative electrode, as presented by reaction (3.29)(YANG et al., 2017), instead of intercaliting into it(RENIERS; MULDER; HOWEY, 2019; EDGE et al., 2021).

$$Li^+ + e^- \rightarrow Li(s) \tag{3.29}$$

This reaction typically occurs either due to high lithium concentration on the solid-phase surface (c_{ss}) or low electrolyte potential (ϕ_e). The former can be caused by fast charging or slow solid-phase diffusion due to low temperatures. The latter can be caused by fast charging or pore-clogging (O'KANE et al., 2022).

Plated lithium can be returned as lithium ions during the subsequent discharge in a process known as lithium stripping, thus recovering lost capacity. Alternatively, plated lithium can undergo further side reactions and become SEI. The growth of the metallic lithium layer, eq (3.30), is described similarly to the growth of the SEI layer, eq (3.22). The rate of Li-plating and stripping can be represented by standard Butler-Volmer or Tafel kinetics. Some Li-plating models, including the one featured in (YANG et al., 2017), present the model as irreversible, without accounting for lithium stripping, eq (3.31). Where plating overpotential is described by (3.32).

$$\frac{\partial L_{pl}}{\partial t} = -V_{pl}\frac{j_{pl}}{\mathcal{F}a_s} \tag{3.30}$$

$$j_{pl} = -a_s i_{pl}^0 \exp\left(\frac{\alpha_{pl}\mathcal{F}}{RT}\eta_{pl}\right) \tag{3.31}$$

$$\eta_{pl} = \phi_s - \phi_e - R_{\text{film}}j_T \tag{3.32}$$

Other models, such as the one proposed in (O'KANE et al., 2020; O'KANE et al., 2022), do attempt to account for reversibility of Li-plating by including stripping. This model, shown in eq (3.33), tracks the total plated lithium concentration (c_{pl}) which builds up over time, eq (3.34). Models with stripping are sometimes used to simulate fast Li-plating under conditions of fast-charging in low temperatures in (O'KANE et al., 2020). Outside these extreme scenarios, its unlikely that such rapid growth will be observed outside a pore-clogging scenario; as such, for long-term Li-plating model, the simpler irreversible model of, described in (3.31), is used.

$$j_{pl} = \mathcal{F}k_{pl}\left(c_{pl}\exp\left(\frac{\mathcal{F}\alpha_{pa}\eta_{pl}}{RT}\right) - c_e\exp\left(\frac{-\mathcal{F}\alpha_{pc}\eta_{pl}}{RT}\right)\right) \tag{3.33}$$

$$\frac{\partial c_{pl}}{\partial t} = -\frac{j_{pl}}{\mathcal{F}} \tag{3.34}$$

3.3   Conclusions

Chapter 2 and 3 served as a good theoretical basis for this project. The rest of this dissertation focuses on the simulation experiment: testing long-term battery degradation in an electric vehicle using a physics-based battery model and a EV powertrain model.

Chapter 4 describes the preparation and characterization of the model used. Appendixes A and B – referenced within this chapter – include and explain snippets of Python and Matlab code used to set-up this simulation.

4 System Description

This work aims to simulate and study the long term degradation of a battery electric cell. In its first-life, this battery cell operates within an electric vehicle; more specifically, a bus following in a regular and predictable route around the UFMG Pampulha Campus – as described by the drive-cycle included in (ALCANTARA, 2022). Once the battery cell model reaches 80% of its original capacity, a new battery simulation using data from the previous experiment will be run based on a less capacity and power intensive grid-support application – this represents this cells transition to a stationary second-life. This simulation then runs until the start of the aging knee-point (end of battery second-life).

To simulate the electric vehicle dynamics, a Simulink model is constructed based on the mathematical modelling described in Section 2.1 of this thesis. Section 4.1 describes the specifics of this simulink model.

The battery cell itself is represented using a physics-based model; though more computationally complex, this approach has the potential of being the most accurate for degradation simulation if properly calibrated, particularly for simulating long-term second-life degradation (ATALAY et al., 2020; HU; DENG, et al., 2022). Instead of programming the physics-based model from scratch – which would be an endeavour outside of the scope of this project – this work relies on a preexisting open-source electrochemistry based battery model: PyBaMM (Python Battery Mathematical Modelling), an open-source battery simulation library for Python which includes many kinds of battery models of differing levels of complexity (SULZER et al., 2021; PYBAMM, T., 2024b). Section 4.2 describes the PyBaMM tools.

Section 4.3 describes the simulation workflow necessary to integrate the MATLAB/Simulink and PyBaMM models and run a long-term degradation simulation experiment.

4.1   Simulink Model

The electric vehicle powertrain model is implemented with MATLAB/Simulink using the equations described in Section 2.1. This mathematical model is based primarily on the one shown in (ALCANTARA, 2022) with modifications aimed at improving accuracy as per (MIRI;

FOTOUHI; EWIN, 2021) and (OLIVEIRA et al., 2023).

Figure 4.1 presents a simplified diagram for the simulink model for the electric vehicle powertrain. The model inputs are the drive-cycle (vehicle reference speed overtime) and a inclination time series (road-slope in degrees overtime). Both of these have been measured by (ALCANTARA, 2022) and are based on the planned bus route shown in Figure 4.2. These datasets, shown in part in Figure 4.3, have time-steps equal to one second ($dt = 1s$).

The powertrain model output is P_{pack}, this values represents the power consumed from – or delivered to – the battery storage system; P_{cell} represents the power delivered to an individual cell, approximated by multiplying P_{pack} by the ratio of cell capacity over pack capacity. Note that realistically, P_{pack} would include power delivered to systems other than the powertrain such
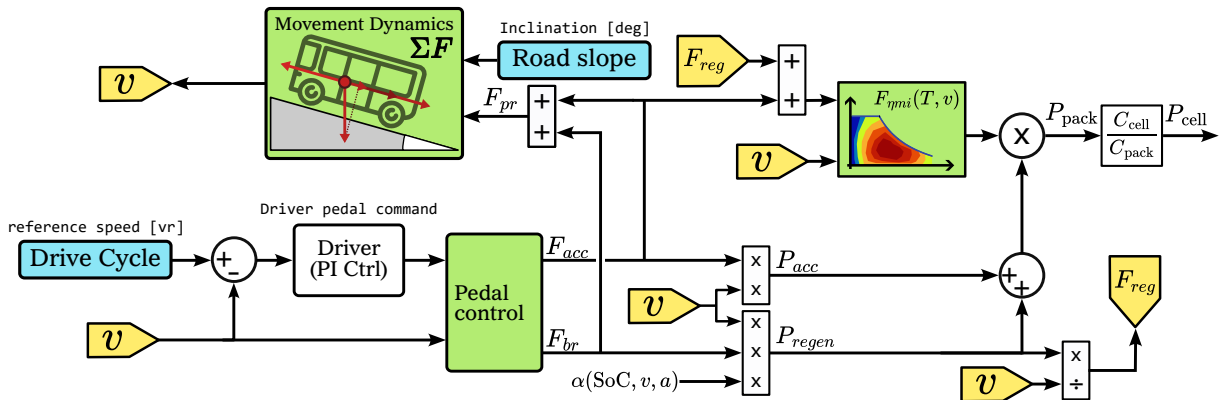
Figure 4.1 – Full model diagram of Electric Vehicle powertrain.

Figure 4.2 – Route performed by e-bus. Basis for drive cycle and inclination time series developed by (ALCANTARA, 2022) used in this work. Figure originally from (ALCANTARA, 2022).
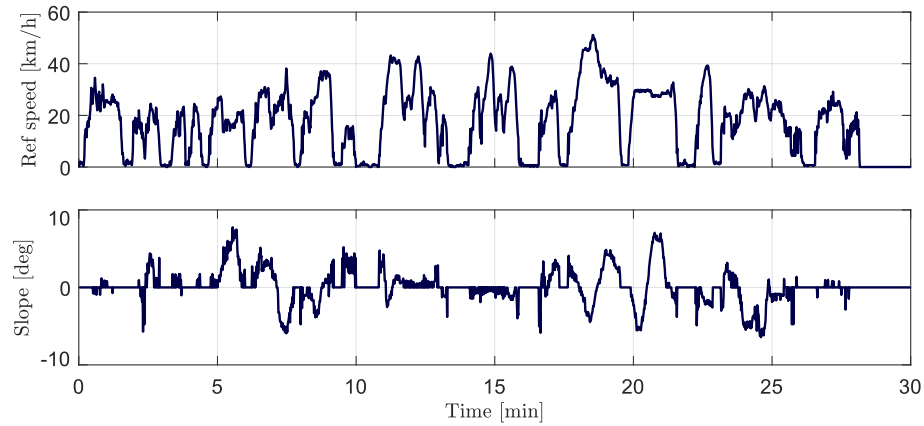
Figure 4.3 – Drive-cycle and road inclination derived from bus-route in Figure 4.2. Adapted from (ALCANTARA, 2022).

as heating/cooling, on-board computers and controllers, media and stereo systems, among others. The powertrain, however, is the single most significant system by an order of magnitude, thus it is the only one represented in this simulation model.

The movement dynamics block in Figure 4.1 models vehicle movements as described by equations (2.1 2.2, 2.3, 2.4) and (2.5). This blocks depends on bus characteristics such as mass, drag and friction coefficient, vehicle front area and others. The full list of values for the electric vehicle properties and variables used in this Simulink model are listed in Table 4.1.

The pedal control block in Figure 4.1 models the brake and acceleration system as presented by Figure 2.6 and equations (2.11, 2.12, 2.13). This blocks depends on the drive pedal command PI controller block as input, the P and I values used for this controller block (included in Table 4.1) are the values which managed to minimize the errors, as measured through 'root mean square deviation' (RMSE), between reference and model output speeds.

Lastly, the motor and inverter efficiency block in Figure 4.1, represented by function $F_{\eta mi}$, is a look-up table which returns electrical efficiency (or its inverse) as a function of motor torque (a combination of acceleration and regenerative torque) and rotational velocity in accordance with (2.10). Electrical efficiency is a value between zero and one, if the vehicle is actively accelerating (meaning that propulsion force F_{pr} and velocity v are heading in the same direction). Then this blocks provides the inverse of efficiency; otherwise, block outputs the efficiency value itself. This dynamic is expressed by (4.1), where the efficiency map being used, shown in Figure 4.4, is roughly based on motor-inverter efficienct map for the 2014 Honda Accord shown in Figure 2.4, from (OZPINECI, 2015). The use of a private vehicle motor-inverter efficiency curve

Table 4.1 – BYD electric-bus parameters for simulation. Adapted from (BYD, 2022) and (AL-
CANTARA, 2022).

Parameter Name	Value
Mass (M)	20300 kg
Max torque (T_{max})	1100 Nm
Max power (P_{max})	300 kW
Max regenerative power (P_{reg}^{max})	180 kW
Gear ratio (G)	22
Wheel radius (r_w)	0.502 m
Front area (A)	8.20 m^2
Transmission efficiency (η_t)	0.80
Rotational inertial coeff (k_m)	1.3
Air drag coeff. (C_{drag})	1.3
Rolling resistance coeff. (C_{rr})	0.01
Driver controller value 'P'	0.30
Driver controller value 'I'	0.08
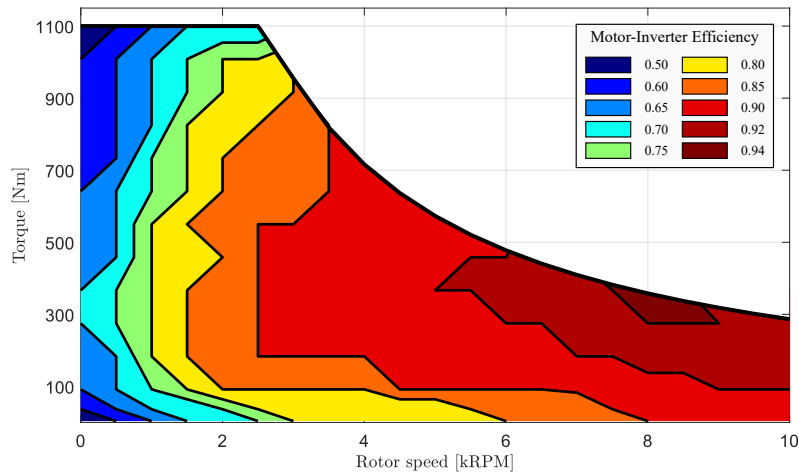
Figure 4.4 – Motor-inverter efficiency map and torque curve. Illustrative model based roughly
on the 2014 Honda Accord efficiency map, shown in Figure 2.4.

in the context of an e-bus simulation is unrealistic, in this case, it is done out of a lack of better
source of data.

$$
F_{\eta mi} = \begin{cases} \eta_{mi}(T_m, v)^{-1}, & \text{if } F_m > 0 \\ \eta_{mi}(-T_m, v), & \text{otherwise} \end{cases} \tag{4.1}
$$

Given the Simulink model described in this section, Figure 4.5 compares the models
inputs (road slope and reference drive-cycle velocity) and outputs (battery power and measured
output velocity) for a period of three minutes near the start of the drive cycle.
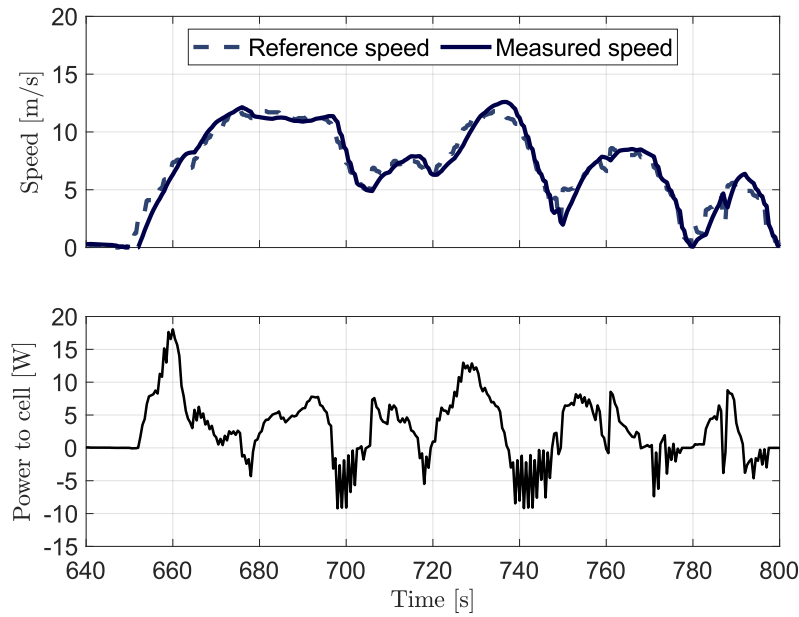
Figure 4.5 – Simulink models inputs velocity (reference and measured) and output (cell power consumption) during a three minute window.

4.2 Battery Simulation Tool: PyBaMM

The physics-based battery models described in Chapter 3 are complex systems comprised of non-linear, intermingled, differential equations. As such, implementing even a relatively simple model from scratch is a big challenge beyond the scope of this project. Thankfully, there already exist commercial and open-source implementations of electrochemical battery models, one of which – PyBaMM – was chosen for simulation in this work.

The two more notable commercial solutions for battery simulations are by COMSOL Multiphysics (NYMAN; EKSTRÖM; FONTES, 2012, 2017) and AutoLion by Gamma Technologies (KALUPSON; LUO; SHAFFER, 2013). Of note, (YANG et al., 2017) and (ATALAY et al., 2020) – two important articles which demonstrated the DFN model with SEI and lithium plating degradation being used to predict the aging knee-point capacity trajectory and that serve as important references for this work – each used AutoLion and COMSOL, respectively, to run their simulation models. Both of these are robust options which see use in the industry and academia. However, the price for these software licenses represents a barrier to use, collaboration, and sharing of results.

The alternative to these commercial implementations are the open-source models. Notable examples include: DUALFOIL (NEWMAN, 1998), LIONSIMBA (TORCHIO et al., 2016),

DEARLIBS (LEE; ONORI, 2021a), Slide (RENIERS; MULDER; HOWEY, 2019; HOWEY, 2019), and PyBaMM (MARQUIS, 2020; SULZER et al., 2021; PYBAMM, T., 2024b). Of these, PyBaMM was chosen as this projects simulation tool.

The Python Battery Mathematical Modelling (PyBaMM) library is an open-source battery simulation package written for Python. It is a frequently updated and well documented codebase which has increasingly been used in academic publications. Unlike some of the previously mentioned open-source battery solutions; which often implement a single type of battery model – be it DFN, SPM, or some other such variation – PyBaMM is not limited to one particular approach. It includes many modelling options and various alternative mathematical representations for any given physical phenomenon. This enables the end-user the ability to customize their battery model in accordance to the needs of each project. This modular approach to battery modelling – which allows for more flexibility – is possible because PyBaMM represents and solves the batteries underlying mathematical models using symbolic logic and computation (SULZER et al., 2021).

Once the entire system of equations is encoded as a symbolic expression-tree, and the simulation space has been discretized; the model can be solved using a time-stepping algorithm. PyBaMM supports a variety of ordinary differential equation (ODE), differential algebraic equations (DAE), and algebraic (root finding) solvers (SULZER et al., 2021). These include SciPy (VIRTANEN et al., 2020), SUNDIALS (HINDMARSH et al., 2005), CasADi (ANDERSSON; ÅKESSON; DIEHL, 2012; ANDERSSON; GILLIS, et al., 2019), and JAX (BRADBURY et al., 2018). Of these, CasADi is the PyBaMM default solver and the one which this work uses and focuses on.

Appendix A includes demonstrations and examples which highlight some of the PyBaMM functionalities which were relied upon in this work. This appendix includes working code which can be used to replicate the results. For more tutorials, examples, and detailed explanations on these and other topics, see the Examples page and the documentation section in the PyBaMM website (PYBAMM, T., 2024b).

4.2.1 Battery Parameter Values

In order to simulate the degradation of a battery cell with a first-life use-case within an electric vehicle, followed by a stationary second-life application; a Physics-based battery

cell model is used, as implemented with the PyBaMM simulation library. By using a relatively more complicated battery model, this work expects to better replicate the long-term degradation mechanisms. In particular; by modelling SEI growth, lithium plating, and pore clogging; this project expects to be able to replicate the aging knee-point dynamics which are characteristic of second-life end of life – the point at which the capacity degradation transitions from growing linearly to growing exponentially (YANG et al., 2017; ATALAY et al., 2020; HU; DENG, et al., 2022).

One of the biggest challenges in implementing a physics-based battery simulation is the process of parametization. These models aim to represent various electrochemical phenomenon mathematically; thus, the resulting equations are dependent on various physically significant parameter variables – see Table 3.2 for some examples. Independently measuring these variables is an expensive and laborious activity as shown in (CHEN, C.-H. et al., 2020), which describes the process of experimentally measuring the 36 parameter variables needed for a simple DFN model.

The process of measurements and tests required to estimate a full battery parameter set is a task outside of the scope of this project. Instead, this work relies on pre-existing parameter sets from the literature. A useful resource in this compiled in resources such as `liiondb.com` – an online database that compiles parameter sets and values from across the literature (WANG, A. A. et al., 2022; WANG; SULZER, 2021). More specifically, PyBaMM itself includes a small collection of parameter sets – including (CHEN, C.-H. et al., 2020). Among the parameter sets pre-included in PyBaMM, "`OKane2022`" – from (O'KANE et al., 2022) – was chosen as the basis for the battery cell model for this projects simulation, basic information about this cell is listed in Table 4.2. This is based on the existence of the "Modelling coupled degradation mechanisms in PyBaMM" example notebook included among the PyBaMM documentation (PYBAMM, 2022).

All the base parameters for the electric vehicle battery cell simulation are thus used unchanged from the pre-existing O'Kane parameter set in PyBaMM. The degradation parameters have, however, been modified. This is because the (PYBAMM, 2022) example includes degradation mechanisms beyond the SEI growth and plating; namely, this example notebook also considers electrode swelling and cracking (a form of Loss of Active Material) and SEI growth in the cracks. To simplify the model and reduce the simulation computational burden,

only SEI (as described by the 'EC reaction limited' model, see Equation (3.5) (SINGLE; LATZ; HORSTMANN, 2018)) and Lithium plating (as described by the 'irreversible' model, see Equation (3.31) (SAFARI et al., 2008)) are used. These are the same mechanisms and models which were used in (YANG et al., 2017).

This change in degradation model necessitates modified parameter values to maintain the original degradation trajectory demonstrated in the PyBaMM example simulation in (PYBAMM, 2022); Table 4.3 lists new parameter values that allow the new degradation model to approximately keep pace with the original example simulation. Additionally, Table 4.3 shows the parameter values for an accelerated degradation experiment. These are the values that actually ended up being used in the simulation in Chapter 5 due to time constraints, unfortunately. The computational burden and simulation time both turned out to be unexpectedly high, making true long-term degradation simulations (which would involve thousands of cycles) impractical.

Table 4.2 – Basic information about the battery cell used in this simulation experiment. Adapted from (O'KANE et al., 2022) and (LG CHEM, 2018).

Property name	Value
Model name	LG M50T – INR21700
Cell type	Cylindrical
Chemistry	NMC 811
Nominal capacity	5.0 Ah
Nominal energy	18.2 Wh
Maximum / Minimum voltage	4.25 V / 2.50 V

Table 4.3 – Parameter values for PyBaMM degradation model. One set of values matches the pace of degradation demonstrated in the PyBaMM example (regular) (PYBAMM, 2022), the other values produces accelerated degradation – used for this project.

Degradation model	Parameter	Regular pace	Accelerated pace
SEI: EC reaction limited	SEI kinetic const. rate	$4 \cdot 10^{-15}$	$2.461 \cdot 10^{-15}$
	EC diffusivity	$1.418 \cdot 10^{-21}$	$2.5 \cdot 10^{-19}$
	SEI molar volume	$9.585 \cdot 10^{-5}$	$3.195 \cdot 10^{-5}$
Lithium-plating: irreversible	Exchange current density	$4.4 \cdot 10^{-5}$	$2.25 \cdot 10^{-4}$
	Lithium metaL molar volume	$1.3 \cdot 10^{-5}$	$6.5 \cdot 10^{-6}$

4.3   Simulation workflow

In order to simulate the long term degradation of a battery cell, the electric vehicle powertrain Simulink model – described in Section 4.1 – is combined with a physics-based cell model in the simulation tool PyBaMM – described in Section 4.2. The goal is to replicate the porosity and lithium plating led aging knee-point – the batteries final end-of-life – as demonstrated

by (YANG et al., 2017; MÜLLER; DUFAUX; BIRKE, 2019; ATALAY et al., 2020), among others. This section describes the interface between MATLAB/Simulink and PyBaMM which allows the two programs to communicate, as well as more details on the simulation set-ups for the first and second life of the battery cell.

The integration between Simulink and PyBaMM battery models is possible through the common medium of CasADi, an open-source software package for solving optimization and differential systems using symbolic logic, available as a package/library for Python, C++, and MATLAB/Octave (ANDERSSON; GILLIS, et al., 2019). CasADi is used by PyBaMM as its default solver of differential equations; meaning that, internally, the mathematical representation of the battery cell is converted into CasADi functions whenever PyBaMM runs to solve a simulation. By extracting and exporting the CasADi functions from PyBaMM and into MATLAB, it is possible to implement a PyBaMM battery block within a Simulink model. This was first demonstrated in (TRANTER, 2021).

The Simulink block – represented by Figure 4.6 – takes cell power (P_{cell}) and temperature (T_{cell}) as input and outputs an arbitrary list of variables which can be determined by the user. In this case, output variables include cell voltage, current, total remaining capacity, and heat. Appendix B details the internal workings – including the code used – of the CasADi Battery Simulink block which runs two CasADi functions per Simulink time-step based on the PyBaMM model.

Importantly, although PyBaMM includes support for thermal models, these tend to massively complicate the mathematical model and add to the simulation convergence time. By
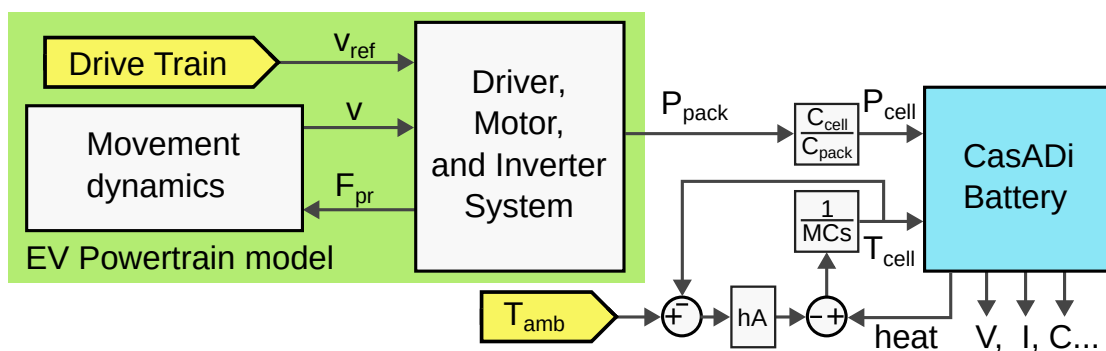
Figure 4.6 – Diagram for Simulink model. Connection between Powertrain model and CasADi battery block.

defining the PyBaMM thermal model as "isothermal" (the simplest model, where there is no internal heat generation and cell temperature equals ambient temperature) and calculating cell temperature externally, in Simulink, the CasADi simulation is significantly sped up (TRANTER, 2021). The thermal model implemented in this model is the lumped thermal model, described in (PRADA, 2012). The heat generated by the battery is calculated within the Simulink block but outside the CasADi function in accordance to Equation (3.20) (see appendix B for more details). The temperature of the battery cell overtime is calculated using simple Simulink blocks (shown in Figure 4.6) in accordance to Equation (3.17). Ambient temperature (T_{amb}), measured in Kelvin, is the one input for this thermal model; it changes over the course of the simulation following a half-sine shape, as described by (4.2) – where T_{base} is a random value between 21 and 27 Celsius (equivalent to 294.15 to 300.15 K), T_{amp} is a random value between 1 and 6 K, and T_{max} is equal to 10 hours, the maximum possible simulation length. Note that in (4.2), lower-case t and upper-case T are used to indicate different metrics: time and temperature respectively.

$$T_{\text{amb}} = T_{\text{base}} + T_{\text{amp}} \cdot \sin\left(\pi \cdot t / T_{\text{max}}\right) \tag{4.2}$$

Using this setup, it is possible to run an electric vehicle discharge cycle. While a similar simulation workflow could be used to execute the simulation charging steps within Simulink, it still is more convenient to run those in PyBaMM. These charging stages are defined by a period of either constant current (CC) or constant power (CP) charging, followed by constant voltage (CV) and a rest period. These long periods of stable (constant) input values benefit from longer simulation time-steps, which can be more flexibly adjusted in PyBaMM. To make use of PyBaMM mid-execution time-step adjustment and to avoid having to implement CCCV or CPCV charging control in Simulink (which is already present in PyBaMM anyway), Python will be used to run the charging steps.

To alternate between simulating the battery in MATLAB/Simulink and Python, the workflow shown in Figure 4.7 was developed – executed by the Matlab code in Listing 4.1. In the first stage, PyBaMM is used to describe the initial battery model. This includes everything from the model type, degradation sub-models, parameter set, simulation time-step and model input and output variables are all chosen. The model is initiated with a short simulation and the two CasADi functions and the internal variables y vector are exported, written to file. In the second stage, the Simulink model is activated. Upon start-up, the CasADi battery blocks loads the functions and variables vector; at the end of the simulation, the new values of the 'y' vector

```matlab
1  n_total_cycles = 1000;
2  cycles_per_loop = 5;
3
4  % set-up pybamm model
5  system("conda run -n pybamm_env python pybamm_setup.py");
6  % runs python file using specific conda python enviroment
7
8  for ii = 1 : cycles_per_loop : n_total_cycles
9      out = sim("Simulink_EV_model.slx"); % runs simulink model
10
11     % save simulink data
12     y0 = out.y0
13     save("temp/y_new.mat", "y0"); % overwrite y_new
14     save("temp/y_" + num2str(ii) + ".mat", "y0"); % save a copy
15     writematrix([out.tout, out.power_timeseries], "save/power_data.csv");
16     writematrix([out.tout, out.temp_timeseries], "save/temperature_data.csv
       ");
17
18     % runs charge cycle plus 'cycles_per_loop-1' discharge and charge
       cycles
19     system("conda run -n pybamm_env python pybamm_cycle.py " + ...
20             int2str(cycles_per_loop-1));
21 end
```

Listing 4.1: Simplified MATLAB code which executes long-term simulation workflow shown in Figure 4.7.
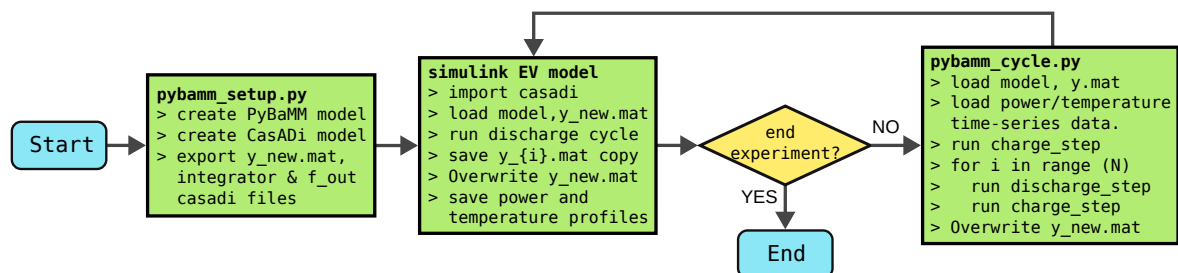
Figure 4.7 – Workflow for long-term degradation simulation experiment which alternates between running in MATLAB/Simulink and Python/PyBaMM. Implemented by code in Listing 4.1.

are saved to file. Lastly, a second Python file is run, this loads the model – the same as was used in the stage one – and the newest copy of the 'y' vector; with this, PyBaMM runs a charging cycle and saves the new value of 'y' to file. In a previous version of this code, the third stage of this workflow was used to run N pairs of discharge and charge step pairs – in addition to the initial charging step. This was originally done to save time, as simulating a drive-cycle in PyBaMM using pre-determined power and temperature time series (discussed in Section A.2) can, in some cases, be faster. Adjustments made to the code and solver settings have, however, significantly sped up the Simulink simulation such that this functionality is no longer used. Nevertheless, the capability is still present in the code and in the diagram of Figure 4.7.

The whole workflow can be executed within MATLAB by using either the built-in Python interpreter in MATLAB or using the 'system' command to execute Python code through the command prompt. Listing 4.1 shows an abridged piece of code which executes the workflow from Figure 4.7.

4.4 Conclusions

This chapter describes the parameters for the second-life battery simulation experiment. The simulation uses a physics-based model built using PyBaMM to represent the battery. Specifically, the battery cell is represented using a DFN model (DOYLE; FULLER; NEWMAN, 1993) with simplified solid-phase diffusion submodel based on quartic polynomial concentration profile, as described by (3.8) (SUBRAMANIAN; DIWAKAR; TAPRIYAL, 2005). The battery thermal model is constructed outside of the PyBaMM/CasADi mathematical model itself, in Simulink. It is modelled in accordance to the lumped thermal model described in (3.17) and (3.20) (PRADA, 2012). The degradation mechanisms included in this battery model are EC-reaction limited SEI growth model, as described by Equation (3.28) (SINGLE; LATZ; HORSTMANN, 2018); and irreversible lithium-plating, described by Equation (3.31). The base parameters used for this battery model are given by (O'KANE et al., 2022), one of the parameters sets which come pre-installed with PyBaMM. The degradation parameters, however, are adjusted to cause accelerated loss of capacity and degradation (knee-point within roughly 100 cycles), the values used for this Simulation are shown in Table 4.3.

The whole project was simulated on an ASUS X515JF laptop equipped with 8Gb of RAM and a 1.0GHz Intel core i5-1035G1 processor. As for software, this work uses MATLAB R2022b, Python 3.10.13, PyBaMM 24.1, and CasADi 3.6.4.

Chapter 5 discusses the simulation results.

5 Discussion of Results

The simulation experiment described in this project occurs in two stages, one for each of the batteries lifetime use-cases.

In its first-life, the battery pack is used within an electric bus following a pre-determined route within the Pampulha Campus of the Federal University of Minas Gerais. To simulate this stage of the battery life, a Simulink model representing the EV powertrain with a CasADi battery cell block is used to simulate each vehicular discharge cycle. This model and its relationship/interface with PyBaMM is depicted in diagram form in Figures 4.1, 4.6, and 4.7; and is described and explained in greater detail in Sections 4.1 and 4.3. Each discharge cycle simulation is made up of many instance of the Pampulha campus bus route drive cycle described in (ALCANTARA, 2022); every time a lap around the route is completed (once every 28 simulated minutes), there is a 10 minute rest period before the route restarts. This process is repeated for 10 simulated hours or until the battery State-of-Charge reaches 5% of its nominal capacity. Following that, at the end of every simulink discharge cycle, a copy of the internal variable vector y is saved to file for future use and then exported to Python/PyBaMM where the charging step is simulated using a CPCV charging pattern followed by 10 hours of simulated rest. This process is described in greater detail in Sections 4.2 and 4.3.

Originally the plan was to the simulate discharge drive-cycle within Python/PyBaMM using the pre-establish power and temperature cycles from the Simulink simulation. In this scenario, drive-cycle simulation within Simulink would only be done occasionally to update the power and temperature profiles as the cell degrades. However, through tinkering with some of the solver options, the difference between simulating the drive-cycle discharge in Simulink and PyBaMM was minimized such that the option ended up not being used; though the option is still present in the code.

The charge-step in Simulink and discharge-step in PyBaMM simulation loop (depicted in Figure 4.7) is repeated until the aging knee-point is reached. This is the point at the very ending of the battery life when degradation transitions from growing linearly to growing exponentially due to increased rate of plating (YANG et al., 2017).

The second stage of the simulation experiment encompasses the battery second life. Using a copy of the battery internal variables vector y saved during the simulation first stage, it is possible to restore the battery to one of its past states. This is used to restore the battery to a point just after it reached 80% State-of-Health. Then, this version of the battery is put under a stationary use-case, characterized by more stable temperatures, narrower Depth-of-Discharge bands, and limited C-rates. More specifically, the simulation subjects the battery model to a time-shift charge profile: charging at low C-rates for most of the day and discharging for 3 hours during peak-consumption hours. This simpler simulation is easily implemented using PyBaMM.

The goal is to compare the rate of degradation between different implementations of the stationary use-case and the base-case of continued first-life electric vehicle use. Section 5.1 discusses the results from the first stage of this simulation experiment, degradation while being used within an electric vehicle. Section 5.2 discusses the second stage of this simulation work, stationary use in the battery second life.

5.1   Battery First Life

Using the accelerated degradation parameters shown in Table 4.3, the electric vehicle battery simulation was run up to the aging knee-point end-of-life, which occurred in the 117th cycle. Each cycle had been made up of a 'discharge' step, consisting of a Simulink drive-cycle simulation for 10 simulated hours or until the battery cell reaches 5% State-of-Charge; and a 'charge' step, which consists of CPCV charging followed by a long rest period meant to represent night-time.

The entire simulation – all 117 cycles – was completed in 44 hours and 50 minutes of simulation time. Each discharge step took an average of 146 seconds per simulated hour, or 24 minutes and 23 seconds for a 10 hour simulation. This ratio remained consistent even as the battery degraded and cell capacity decreased, causing the discharge steps to end before reaching the 10 hour mark by triggering the state-of-charge end-point. Meanwhile, each charging step – which consists of charging for roughly two hours at 9W (roughly 0.5 C-rate) followed by 12 hours of rest – took on average 16 seconds to run. This discrepancy is in large part due to the differences in time-step. The Simulink model has a fixed time-step equal to 0.5 seconds. This is necessary due to the nature of electric vehicle simulation, which naturally involves rapidly changing power demand as the vehicle accelerates and decelerates. By contrast, because the

charging step consists of much more stable input values, the time-steps can be significantly longer – as long as one minute per time-step during the constant power step and five minutes during the rest step.

At this pace of roughly 60 simulated cycles per day, a correctly paced long-term simulation (which would involve several thousands of cycles) would take months to run. This is why it was decided that, for demonstrations purposes, this project should use accelerated degradation parameters. The time taken to arrive at a solution is an important factor in determining the usefulness of simulation experiments, this presents a problem for the physics-based model approach seeing as the pace presented in this work might be prohibitively slow for some simulation projects; particularly in the context of electric vehicle simulations, which require short time-steps. The simulation pace can be further optimized and improved by having access to better processing power; simplifying the battery model (by limiting the number of nodes in discretization and/or using an SPM model as opposed to a simplified DFN, for instance); better tuning the CasADi solver settings, as discussed in (LI; O'KANE, et al., 2024); and by replacing the fixed time-step with a more flexible approach which adapts to variations in the input values.

Outside of the context of Electric Vehicles, most other applications – such as, for instance, stationary grid-supporting storage – can be simulated using significantly longer time-steps. In those cases, the simulation set-up as described in Chapter 4 likely can be used without pace of simulation being as much of a significant problem. Additionally, in the case of a digital-twin where the goal is more so for the simulated model to keep up with the real life equivalent rather than to run through the entire life-cycle in one go, the aforementioned pace of simulation is less of a problem.

In terms of degradation, SEI growth is the main cause of degradation for most of the battery life-cycle – as expected. Figure 5.1a) shows the trajectory of capacity lost to SEI through the entire experiment as a function of total capacity throughput. During the initial few cycles, rate of SEI led capacity loss is slightly elevated but that subsides after the initial few cycles and capacity loss remains roughly linear for the rest of the simulation. In Figure 5.1b), the share of capacity lost to Lithium-plating is an order of magnitude smaller than what is lost to SEI. Additionally, the rate of growth for plating remains roughly constant (linear) throughout most of the simulation up until the very end, at which point the rate of change increases significantly – as expected from a plating led knee-point. Shortly after that, however, the simulation crashes,
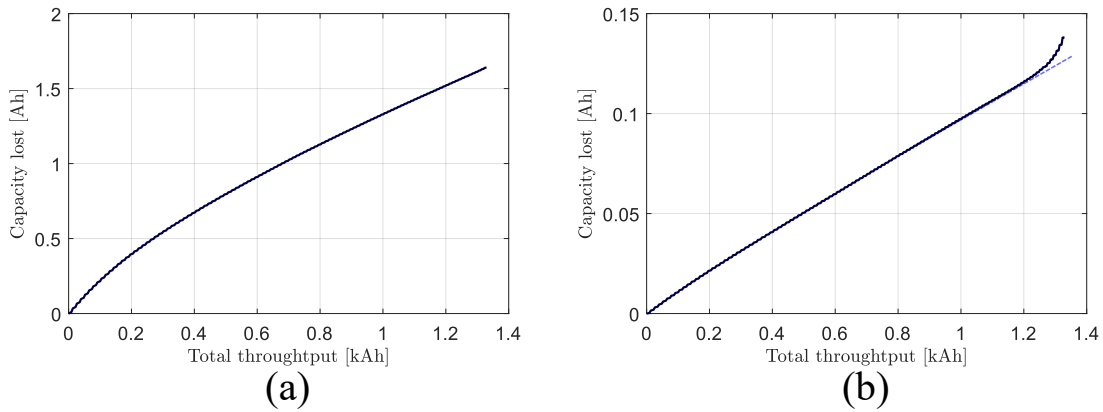
Figure 5.1 – Loss of battery cell capacity (in Ah) overtime due to the two main degradation mechanisms. a) SEI Growth. b) Lithium-plating, with linear growth trend-line (dashed, in light-blue) to highlight acceleration of degradation near end-of-life.

CasADi is unable to converge towards a result. This tends to happen as porosity (which is inversely proportional to electrolyte resistivity) approaches zero. Though the simulation would ideally continue, by the point at which it crashes, the battery is already starting to undergo non-linear capacity loss and quickly approaching its definitive end of life. The simulation could in theory be made more stable such that it does not crash so soon and extends further into the knee-point region by using a more finely discretized model or by adjusting the CasADi solver option parameters. Both of these alternatives come at the cost of increased model complexity and simulation convergence time.

Though the acceleration of lithium-plating degradation is visible from Figure 5.1b), the simulation crashes before this transition is perceptible in the plot of total capacity, shown in Figure 5.2. This reflects well on the ability of physics-based models to forecast the start of the aging knee-point by modelling different degradation mechanisms individually. Another way to observe the capacity degradation is by plotting the voltage profile overtime – as is shown in Figure 5.3.

Both SEI and plated lithium are thin film-like layers of material which grow on top of the interface between the negative electrode material and the electrolyte. The thickness of the SEI and plating layers are directly proportional to the amount of lithium consumed by both of these side-reactions, as described by Equations (3.22) and (3.30). The build-up of this film occurs unevenly along the cell. More specifically, one would expect these layers to be thinnest near the current collector and thickest near the separator. Additionally, the increased rate of lithium-plating formation is supposed to be caused primarily by accelerated build up of metallic

lithium near the separator (KLETT; ERIKSSON, et al., 2014; KLETT; SVENS, et al., 2015; YANG et al., 2017).
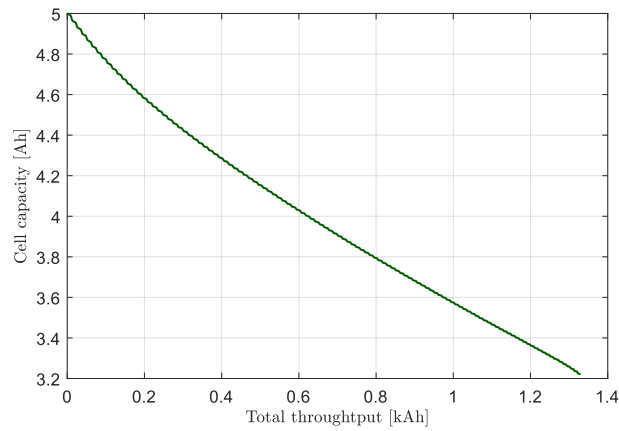
Figure 5.2 – Total battery cell capacity as cell ages, relative to total throughput.
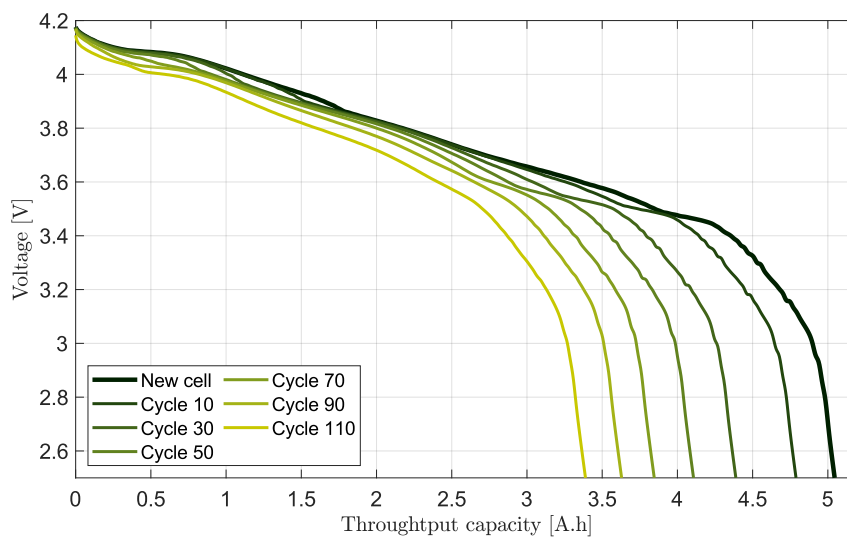
Figure 5.3 – Voltage profile as a function of throughput capacity overtime. Values obtained from constant power discharge at 1W, approximately 1/18 C-rate.

The nature of physics-based battery model allows one to investigate these internal chemical properties. Indeed, all of these end-of-life characteristics were replicated in the simulation experiment. Figure 5.4 shows the negative electrode porosity value (at the current collector, separator, and average) overtime. As both the SEI and plating films grow, they occupy more space and consume electrolyte material – this causes the share of the volume occupied by the electrolyte (ie. electrode porosity) to decrease. For most of the battery life-cycle, the difference between the mean and separator porosity remains consistent – as seen in Figure 5.5. Once the average porosity reaches a certain threshold (around 0.05 in this case), lithium-plating in

particular starts to accelerate and the separator porosity starts to more significantly diverge. This can be seen in Figure 5.5 and in the highlighted section of Figure 5.4.
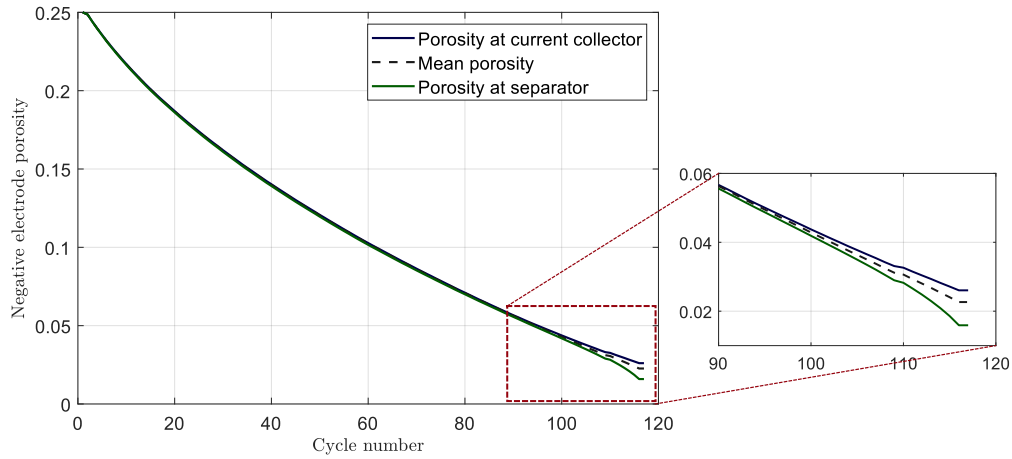
Figure 5.4 – Negative electrode porosity (volume share of electrolyte) overtime as a function of cycle number. At current collector and separator interfaces and electrode average.
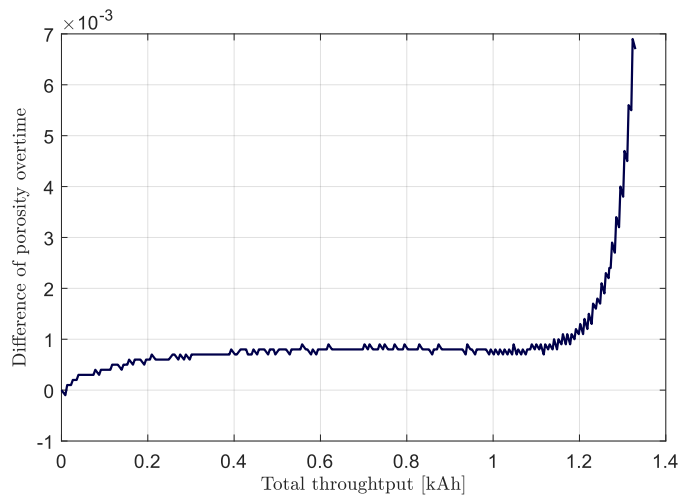
Figure 5.5 – Difference between average negative electrode porosity and porosity at the separator interface overtime. Point of divergence (approximately 1200Ah) coincides with cycle 100 in Figure 5.4.

Figures 5.6 and 5.7 show the thickness of the SEI and plated lithium films along the normalized negative electrode length – where x=0 is the negative current collector and x=1 is the anode-separator interface. Figure 5.6a) shows the total thickness of the SEI film overtime; it grows linearly and near uniformly throughout the cell for the majority of the battery life-cycle. Figure 5.6b) highlights the small differences in SEI thickness along the x-axis by plotting the thickness difference relative to the thickness at the current collector – the point within the negative electrode where SEI remains the thinnest for the entire battery life-cycle. The relative

thickness distribution remains approximately constant for most of the cell life up until cycle 90; after which there is a small pick-up in SEI growth particularly in regions nearer to the separator. This sudden acceleration matches the divergence point in Figures 5.4 and 5.5 which occurs at the 100th cycle, which coincides with 1200Ah of total throughput.

This is in contrast with the thickness of the plated lithium layer. Figure 5.7a) shows the build-up of plated lithium overtime; it occurs approximately linearly and uniformly at first – similarly to the build up of SEI shown in Figure 5.6a) – up until cycle 90. After the 100th cycle, the rate of lithium plating near the separator speeds up by an order of magnitude – a lot more dramatically than what occurs with SEI growth. Figure 5.7b) highlights the exponential nature of accelerated plating build-up past the start of the knee-point by displaying the plated lithium film thickness in proportion, as a percentage, relative to the thickness at the thinnest point – near the current collector. Note that, unlike the graph in Figure 5.6b), which plots the *difference* between thickness at a given point and the minimum (one minus the other), Figure 5.7b) shows the *proportion* of thickness at a given point relative to the minimum (one divided by the other). This visualization better highlights the multiplicative nature of plating growth towards the end of life. Comparing Figures 5.6b) and 5.7b) also reveals that while the SEI thickness difference distribution profile remains consistent prior to cycle 100, it is the plated lithium ratio distribution profile the thing that remains consistent up until cycle 100. This hints at the exponential rather than linear nature of lithium-plating distribution even prior to the aging knee-point.
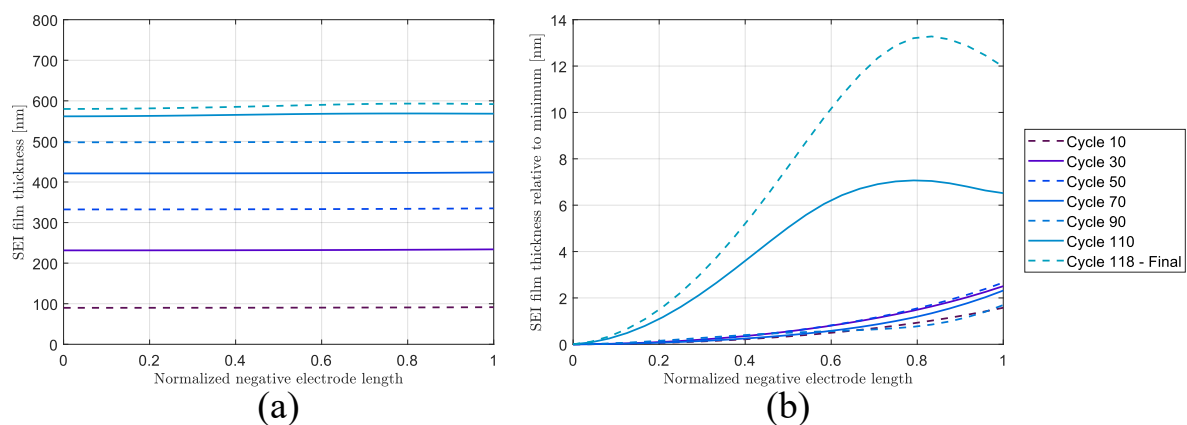
Figure 5.6 – Evolution of the distribution of SEI film thickness overtime. a) Total thickness. b) Thickness difference relative to minimum.
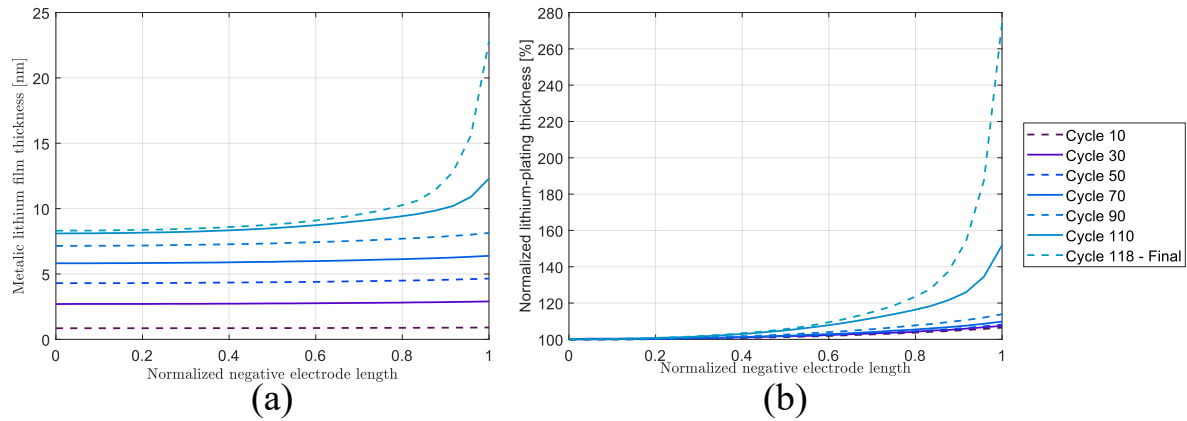
Figure 5.7 – Evolution of the distribution of plated lithium thickness overtime. a) Total thickness. b) Normalized thickness relative to minimum.

5.2 Battery Second-Life

As previously stated, at the end of every simulation cycle during the first life simulation a copy of the battery cell data is saved to a file. For second life simulation, the battery data from the cycle closest to 80% State-of-Health mark is loaded and used to run a simplified charge and discharge cycle meant to be representative of stationary battery applications.

These second life cycles occur at a constant ambient temperature equal to 25^oC. This is meant to reflect the more stable and controlled environments available to stationary application. The charge and discharge cycle is meant to resemble an energy time-shift strategy, a basic energy storage application where the battery is charged during off-peak periods – during which the cost of energy is cheaper – and is discharged during peak periods – when energy is more expensive. Under Brazilian legislation, peak hours (*Horário de Ponta*) have a pre-determined start and set length of 3 hours. This pattern can be easily replicated using the in-built 'Experiment' functionality in PyBaMM.

The second-life simulation cycle is described by the code in Listing 5.1. Firstly, the battery is charged at a constant power rate of approximately C/6 then held at the upper voltage value until C/50 (CPCV charging). After four hours of rest, the battery discharges at a rate dependent on depth-of-discharge (equal to C×DoD/3) for three hours or until voltage reaches a pre-determined lower minimum. The cycle restarts after a eleven hour rest period. The upper and lower voltage limits depend on intended depth-of-discharge as described in (5.1), where $V(SoC)$ refers to the voltage profile values for a new cell – shown in Figure 5.8.

$$V_{max} = V(\text{SoC}_{max}) \tag{5.1a}$$

$$V_{min} = V(\text{SoC}_{min}) \tag{5.1b}$$

$$\text{DoD} = \text{SoC}_{max} - \text{SoC}_{min} \tag{5.1c}$$

```
capacity_wh = 18.2;      dod = 0.80
lower_volt_lim = 3.32;   upper_volt_lim = 4.08
sl_exp = pybamm.Experiment(operating_conditions=[(
    f"Charge at 3 W for 6 hours or until {upper_volt_lim}V",
    f"Hold at {upper_volt_lim}V until C/50",
    "Rest for 4 hours (5 minutes period)",
    f"Discharge at {dod*capacity_wh/3} W for 3 hours or until {
    lower_volt_lim}V",
    "Rest for 11 hours (5 minutes period)"
)] * max_cycles, temperature=298.15)
```

Listing 5.1: PyBaMM Python code which defines stationary second-life experiment cycle.
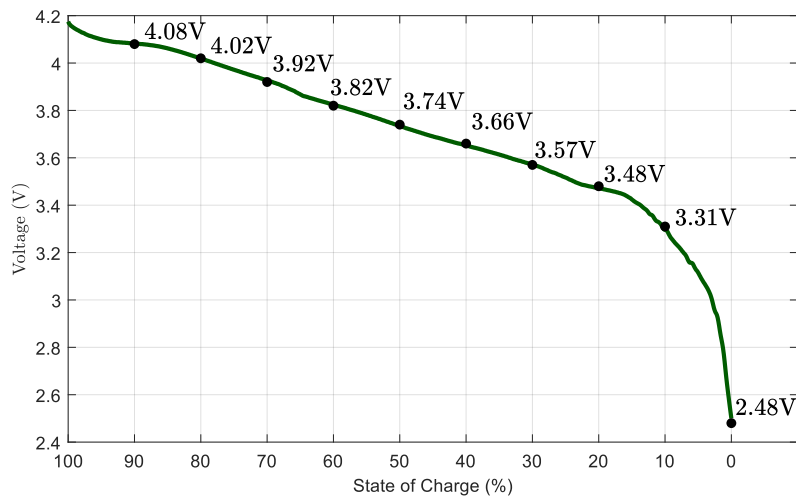
Figure 5.8 – Voltage profile as a function of State-of-Charge for a brand new cell, values obtained with PyBaMM discharge simulation at 1W. Text denotes the voltage value at intervals of 10 percentage points SoC.

The second-life time-shift simulations were done using four values for DoD. For each scenario, both the upper and lower voltage limits and discharge C-rate depend on DoD, as described by (5.1) and Listing 5.1. These values are shown in Table 5.1. The advantage of defining DoD in accordance with upper and lower voltage limits – as opposed to percentage of total capacity in Ah – is that this approach ensures the battery avoids high and low charge states even as the cell continues to degrade and capacity decreases. Additionally, this approach (charge/discharge until a predetermined voltage upper and lower limit) is already pre-programmed into PyBaMM, which makes it more convenient for this experiment. Note that the battery operates mostly on the lower range of the SoC scale, it was determined through trial-and-error that this

minimizes degradation and extends battery life (at least within this simulation).

Table 5.1 – Simulation values for various second-life scenarios. Upper and lower voltage limits and discharge C-rate for different values of DoD.

DoD [%]	Vmax (SoC$_{max}$)	Vmin (SoC$_{min}$)	Discharge C-rate
80	4.08V (90%)	3.32V (10%)	0.267C
70	4.02V (80%)	3.32V (10%)	0.233C
60	3.87V (65%)	3.11V (5%)	0.200C
50	3.78V (55%)	3.11V (5%)	0.167C

Figure 5.9 compares the total cell capacity overtime between first and second life use-cases. The green lines trace the capacity trajectory for the first-life (electric vehicle) simulation, same as was presented in Section 5.1. One green line is darker and solid while the other is lighter and dashed, they respectively represent the before and after of the first end-of-life – which happens when capacity reaches 80% state-of-health value. The lines in blue represent the previously described stationary time-shift use-case for different values of DoD. The darker the hue, the greater the value of DoD. The end point of these plots is the point at which the PyBaMM simulation crashes, which does not necessarily match the ideal second end-of-life as will soon be discussed.

Figure 5.10 shows the total capacity lost due to lithium-plating between the different first and second life use-cases. Note that the lithium plating acceleration – typical of knee-point end-of-life – is observed in the 'First life extended', 'DoD 80%' and (just barely) in the 'DoD 70%' cases. This was initially thought to be an error, perhaps an artifact from the model or parameters not representative of real cell behaviour. However, looking back on (YANG et al., 2017) (in particular, figure 2 from that paper), it seems like there too (both from simulation results and experimental measurements) the angle of the slope post knee-point depends on the
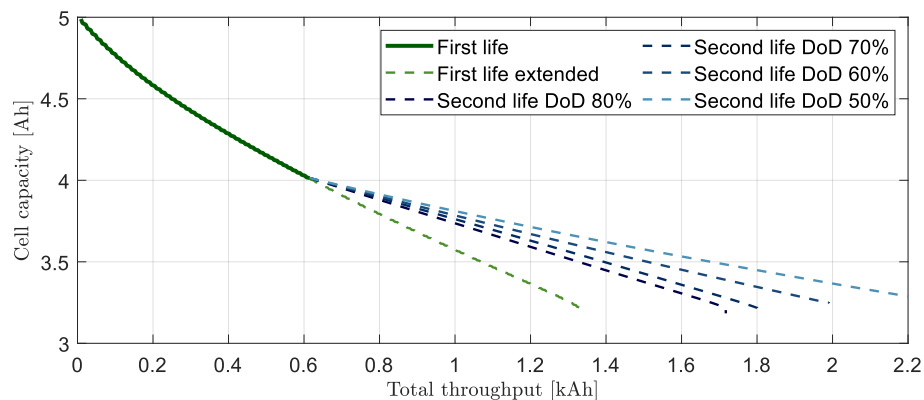
Figure 5.9 – Battery cell capacity overtime for different applied use-cases.
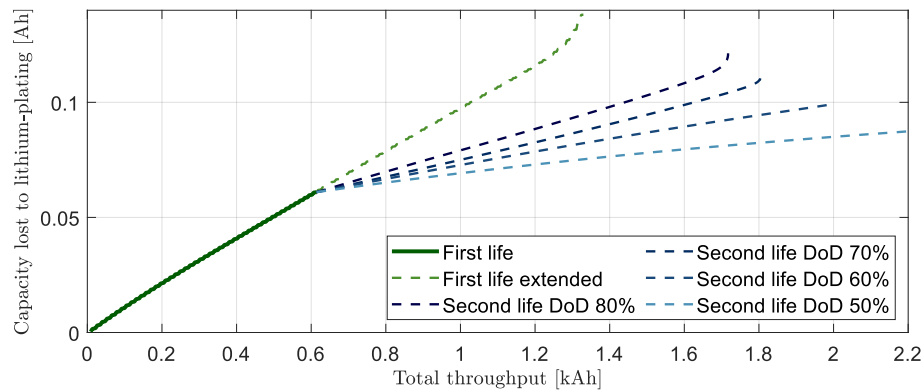
Figure 5.10 – Battery cell total capacity lost to lithium-plating side reaction for different applied use-cases.

discharge C-rate, being much less pronounced for the case with C/3 discharge rate. This might indicate the possibility of limiting and/or delaying the aging knee-point by limiting discharge rates. Overall, this aspect of the simulation is inconclusive; more research – ideally using real experimental measurements as a reference point – is required to better understand this specific facet of knee-point behaviour.

Another previously discussed metric to help determine the start of the aging knee-point is the internal negative electrode porosity. Figure 5.11 shows the mean and separator negative electrode porosity overtime for the five different battery simulations. In all cases, the divergence between mean and separator porosity occurs towards the end of life; despite that, however, the acceleration in the pace of lithium-plating doesn't always occurs. Figure 5.12 more specifically highlights the difference between the two values.

Generally, the second-life use-cases with smaller depths-of-discharge ranges fared better (preserved battery capacity and delayed knee-point for longer) than the ones with the bigger DoD ranges, and all of the second-life stationary examples improved on the first-life use-case capacity trajectory. More specifically, Table 5.2 compares the total end-of-life throughput (both in absolute terms and relative to the first-life example) for different metrics and definitions for the end of useful life – the point prior to the aging knee-point itself when the battery cell would, ideally, be deactivated. The first row of Table 5.2 shows the total throughput at the point when the PyBaMM simulation fails to converge; in terms of strictly physical interpretation, this metric is not particularly meaningful, though it is the one most noticeable from the plots in Figures 5.9 to 5.12. The four other metrics are thresholds values for physical properties related the emergence of the aging knee-point: total state-of-health (the choice of 65% SoH as a threshold end point

was somewhat arbitrary), pace of lithium plating growth, divergence in porosity distribution and mean porosity in the negative electrode region. Lastly, the final two rows include the average and the minimum among the four physically significant values. Given the safety risks associated with plating build-up at the separator, using the 'minimum' row might be advisable as the predictor for the ideal end of a battery second-life and/or estimating RUL.
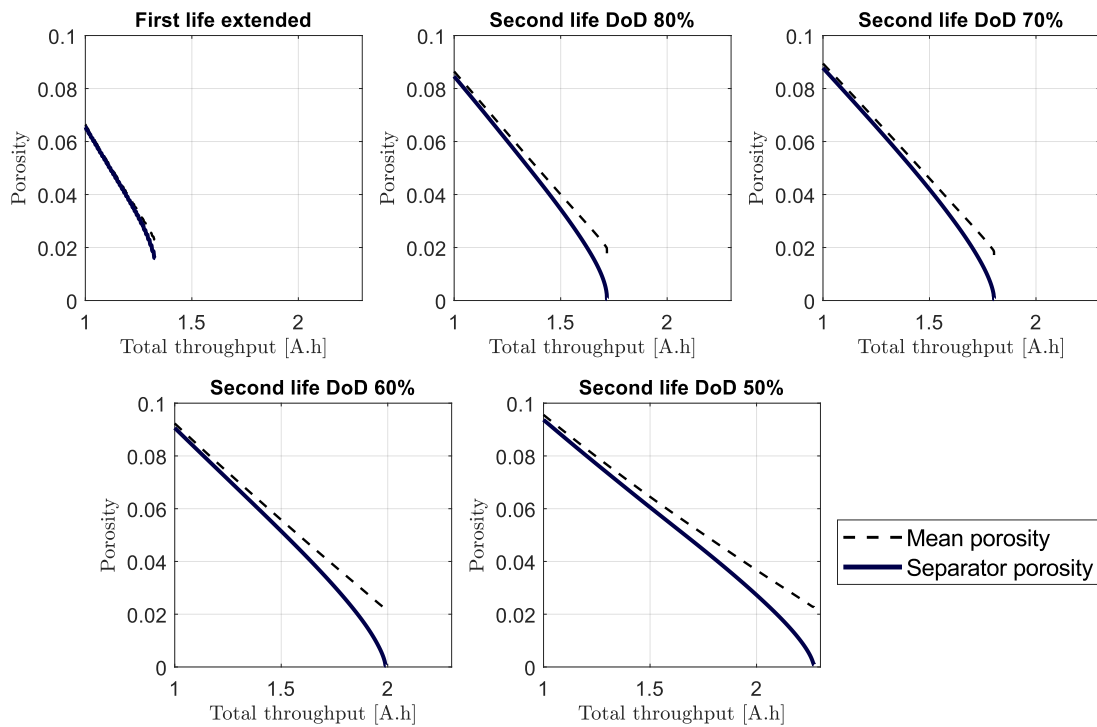
Figure 5.11 – Mean and separator porosity overtime for different battery first and second life use-cases.
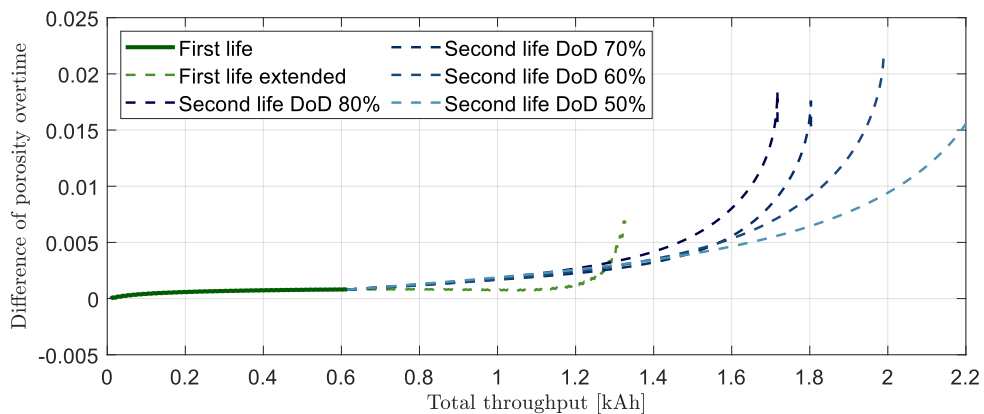
Figure 5.12 – Difference between mean negative electrode porosity and porosity at the separator interface for various simulation use-cases.

Table 5.2 – Total lifetime battery throughput for different end-of-life metrics and simulation cycling parameters. Cells included both total lifetime throughput capacity (measured in Ah) and percentage relative to the "First-Life extended" use-case described in Section 5.1.

	FL-Extended	SL-DoD 80%	SL-DoD 70%	SL-DoD 60%	SL-DoD 50%
Pybamm Crash	**1329.52 Ah**	1717.3 Ah (129.2%)	1803.2 Ah (135.6%)	1990.7 Ah (149.7%)	2270.3 Ah (170.8%)
State-of-Health 65%	**1304.4 Ah**	1677.9 Ah (128.6%)	1756.5 Ah (134.7%)	1979.1 Ah (151.7%)	2270.3 Ah (174.0%)
Plating growth rate (150% initial rate)	**1261.04 Ah**	1662.4 Ah (131.8%)	1749.9 Ah (138.8%)	1989.3 Ah (157.8%)	–
Porosity difference ($\triangle\varepsilon$=0.0067)	**1323.25 Ah**	1556.5 Ah (117.6%)	1649.8 Ah (124.7%)	1692.5 Ah (127.9%)	1823.25 Ah (137.8%)
Mean porosity value (ε=0.03)	**1272.3 Ah**	1614.5 Ah (126.9%)	1681.6 Ah (132.2%)	1873.6 Ah (147.3%)	2126.6 Ah (167.1%)
Average	**1290.25 Ah**	1627.8 Ah (126.2%)	1709.5 Ah (132.5%)	1883.6 Ah (146.0%)	2073.4 Ah (160.7%)
Minimum	**1261.04 Ah**	1556.5 Ah (123.4%)	1649.8 Ah (130.8%)	1692.5 Ah (134.2%)	1823.3 Ah (144.6%)

6 Conclusions and Future Work

Lithium based batteries are complex, non-linear, electrochemical systems which are inherently hard to model. Often, simplified models are used for simulation, forecasting, and control purposes. In Electrical Engineering, it is common to use Equivalent Circuit Models (explained in Section 2.2.2.1) to represent the transient dynamic response from a battery system, and Empirical degradation models (explained in Section 2.2.3) to model and forecast the short to medium term capacity and resistance degradation trajectories. Though these models are greatly simplified and are often agnostic about the real internal cell dynamics, they are perfectly adequate for a lot of control and forecasting use-cases – particularly in first-life use.

In the context of Second-Life Batteries, however, the ability of these simplified models to predict behaviour and forecast degradation is greatly diminished. However, it is precisely during the battery second-life when good simulation and state estimation tools are more needed – particularly the ability to predict and forecast the aging kneepoint. This is because of the greater constraints, fragility, and safety precautions needed in second-life use due to the aged state of the battery cells.

The main alternative to the empirical family of models are the physics-based models. These models mathematically describe the internal physical state and chemical reactions using a system of differential equations. Because there is an effort to represent the underlying electrochemical dynamics, these models have the potential – if properly tuned – of having much higher accuracy, even in extreme situation like high C-rate, high/low temperatures, or late-stage battery degradation (YANG et al., 2017; HU; FENG, et al., 2019; ATALAY et al., 2020). The biggest downside of physics-based models are their complexity, both in terms of parametization (requiring many parameter variables to properly describe each individual cell) and computationally (taking a long time to solve each simulation) (HU; FENG, et al., 2019; CHEN, C.-H. et al., 2020).

The goal of this project was to explore the viability of using these physics-based models to simulate through the full life of a battery, from electric vehicle storage in the first-life to stationary time-shift application in the second-life. For this, an introductory review of the mathematical basis of the physics-based models was written (Chapter 3) and an appropriate open-source

implementation, PyBaMM, was chosen for the simulation (Section 4.2). An Electric Vehicle Simulink model was constructed (Section 4.1) and integrated with the physics-based battery model (Section 4.3). This served as the basis for the first-life simulation, the results of which were discussed in Section 5.1. After that, following the first-life battery simulation, a copy of the internal battery data at cycle 50 – just after the battery had reached the 80% SoH threshold – was loaded back into PyBaMM and used to run second-life simulations. These were able to be run significantly faster than first-life simulations (more than one hundred charge and discharge cycles per hour) due primarily to longer and more flexible time-step options. The results of these second-life simulations are shown in Section 5.2.

One of the big challenges for physics-based models is determining the value for the simulation parameters, (CHEN, C.-H. et al., 2020) describes the measurement process required to define the DFN model for a specific battery cell. To avoid this step, this work uses one of the pre-installed parameter sets included in PyBaMM: 'OKane2022', used in (O'KANE et al., 2022) and (PYBAMM, 2022).

As expected, the simulation takes a long time to run; each full battery cycle during the first life (made up of an electric vehicle discharge drive cycle and a CPCV charging step) took on average 24 and a half minutes to complete, this is mostly due to the short length of the fixed time-steps used in the drive-cycle simulation (dT=0.5s). Given that modern lithium-ion commercial battery cells are able to last for thousands of full cycles, at a pace of approximately 60 simulation cycles per day, it would have taken months to simulate a correctly paced long-term battery degradation experiment. This would not have been viable. Though there are ways to make this simulation faster; like optimizing the model and CasADi solver settings, or by making the simulation time-steps more flexible (allowing for longer steps when there are small or no changes to the power and temperature inputs); for this project the degradation parameters from (O'KANE et al., 2022) were manually modified, as described in Table 4.3, resulting in an accelerated degradation pattern which reaches the 80% SoH threshold within 50 cycles and the aging knee-point within 117 cycles.

The use of fictional degradation values means that the results in Chapter 5 aren't actually reflective of any real battery system. This choice was taken because demonstrating this approach to simulation – the theory, the software, and the workflow – was deemed more important than generating physically significant results in this initial moment. Future work, discussed in Section

6.1, shall focus on applying the techniques described in this project in more practical and experimental applications, including in techno-economic assessments.

Though the battery degradation parameters were in part fictional, the results shown in Chapter 5 still managed to replicate some of the expected behaviour from a real cell. The general aging knee-point pattern of SEI growth leading to anode porosity loss which in turns causes accelerated lithium-plating concentrated near the separator interface described in (YANG et al., 2017; MÜLLER; DUFAUX; BIRKE, 2019; ATALAY et al., 2020) and others was able to be replicated. Additionally, the stationary second-life use-cases did manage to slow the rate of capacity loss relative to first-life electric vehicle drive cycles, as expected.

In some instances, however, the simulation results did not match expectations. Though the results in Figures 5.1 and 5.7 show a small acceleration in the pace of lithium-plating triggered by the fall in porosity and centered on the anode-separator interface, the amount of capacity lost to this reaction was in all cases relatively small – not sufficient to be visible in the capacity plot of Figure 5.2. In some cases, particularly in some of the low DoD stationary cases, the faster rate of plating growth did not transition out of the linear trend. By contrast, in (YANG et al., 2017) – a major influence in this work – lithium-plating represented one third of the total life-time capacity loss by the end of the simulation, the majority of which occurred between cycles 2250 and 3250. Another unexpected aspect of the results had to do with the SEI rate of growth relative to the upper and lower DoD limits. Typically, loss of capacity is minimized by avoiding both high and low SoC regions such that DoD is centered around the middle of the SoC scale (typically at some point between 45% to 60% SoC) (BAGHDADI et al., 2016; RECHKEMMER et al., 2019). However, through trial and error, SEI growth in the simulations of Section 5.2 was minimized by occupying the lower voltage ranges. In some cases, some of these observations might in fact be realistic battery behaviour. Without an experimental reference point, it is hard to say whether these might be a true property of the battery chemistry or whether this is an artifact of the mathematical degradation model or the parameter values.

This work has successfully shown the potential of physics-based degradation simulations in the context of SLBs and demonstrated it with an – admittedly illustrative – example of it being used in combination with a Simulink Electric Vehicle model. There were two main problems with the simulation presented here. The first had to do with the pace of simulation, this was somewhat expected given that physics-based battery models are generally known to be computationally

intensive, though the extent of how slow the first-life simulation actually went was somewhat surprising. This can be ameliorated by tinkering with the PyBaMM and CasADi settings, but a lot of it is due to the very short time-steps that are required from EV powertrain simulations. The second problem had to do with the lack of a experimental references with which to compare the simulation results with. Some of the simulation results were unexpected but perhaps still plausible, without a reference it is hard to determine what is realistic. These two concerns can be worked on in future projects.

6.1 Future work

There are many way this project can be built upon. This section lists some of the more promising and interesting possibilities.

- **Continued research into Second-Life Batteries**. This work is a part of a larger project related to the study of Second-Life batteries, specifically the reuse of batteries originally from electric vehicles in grid-supporting stationary settings. While the focus of this thesis had to do with physics-based simulation models, the 'State-of-the-Art' review in Chapter 2 discusses other relevant dimensions related to Second-Life Batteries in a more superficial manner. These topics could be further expanded upon; of particular interest, Section 2.3.2.1 discusses methods for State-of-Health estimation. Of these, Electrochemical Impedance Spectroscopy (EIS) seems most workable and promising (discussed further in Section 2.2.2.1).

- **Build a physics-based model based on experimental degradation data**. Run a degradation experiment on a real battery cell and use the data as the reference when determining degradation parameters, similar to (ATALAY et al., 2020). Tools such as Parasweep (LI; O'KANE, et al., 2024) can assist in identifying parameters from experimental data in PyBaMM.

- **Expand on the electric vehicle model**. The EV representation described in Section 2.1 and used for this simulation is a simplified model based mostly on steady-state equations. A more robust model which better accounts for vehicle dynamics, particularly within the electric motor, could be useful for capturing the short duration high-power output peaks.

- **Techno-economic analysis**. Once a physics-based model has been calibrated with experimental data such that one can be confident that simulation results reflect plausible and realistic battery behaviour, the model could be used for techno-economic analysis. This was one of the original goals of this dissertation, described in Chapter 1, but it was dropped as a result of the choice to use accelerated degradation parameter. Any economic analysis done under conditions wouldn't have been significant. An economic assessment of SLB should also consider the price of disassembly and assessment of the EV battery pack, as was done in (RALLO et al., 2020).

- **Advanced Battery Management System/Digital-Twin of the battery**. This work described the process of exporting PyBaMM battery data as a numerical vector and two CasADi function files. Using the CasADi library for C++, it may be possible to have an instance of the battery model running in a portable computer (raspberry pi, for instance) alongside the battery using real data measurements as input. This model could function as a digital-twin or serve as a diagnostic tool for an advanced battery management system (HU; FENG, et al., 2019).

- **Grid-supporting battery simulation**. As discussed in Section 5.1, the main cause for the long simulation times was the short simulation time-steps required for Electric Vehicle simulation. In applications such as grid-supporting storage where simulation time-steps can be made to be much longer (sometimes in the order of multiple minutes), the simulation workflow as described in Sections 4.2 and 4.3 could be promising. Combining PyBaMM simulation with a distribution grid simulation tool like OpenDSS might be of interest.

- **Model battery packs**. PyBaMM is specialized in simulating individual battery cells. This is true generally for physics-based models, which concern themselves with the inner state of each cell. In real world applications, however, battery cells are always used bundled together as 'Battery Packs'. Small differences between cells within a battery module or pack – particularly regarding differences in temperature – can have the effect of accelerating degradation in addition to introducing safety risks to the system. Within this work, these differences were ignored, simulation was conducted on a single cell, this is the equivalent of assuming an homogeneous battery pack. To simulate a systems with many cells, one could simulate many cells individually in Simulink, as was done(TRANTER,

2021). There is also "liionpack", a Python library based on PyBaMM for simulating battery modules and packs (PYBAMM, T., 2024a).

Bibliography

AHMADI, Leila; YIP, Arthur, et al. Environmental feasibility of re-use of electric vehicle batteries. **Sustainable Energy Technologies and Assessments**, Elsevier, v. 6, p. 64–74, 2014.

AHMADI, Leila; YOUNG, Steven B, et al. A cascaded life cycle: reuse of electric vehicle lithium-ion battery packs in energy storage systems. **The International Journal of Life Cycle Assessment**, Springer, v. 22, p. 111–124, 2017.

ALCANTARA, Pedro Henrique Fialho de. **Estudo da Autonomia do e-Bus no Campus Pampulha da UFMG**. [S.l.: s.n.], 2022.

ALLAM, Anirudh; ONORI, Simona. An Interconnected Observer for Concurrent Estimation of Bulk and Surface Concentration in the Cathode and Anode of a Lithium-ion Battery. **IEEE Transactions on Industrial Electronics**, Institute of Electrical and Electronics Engineers Inc., v. 65, p. 7311–7321, 9 Sept. 2018. ISSN 02780046. DOI: 10.1109/TIE.2018.2793194.

ALVAREZ, Roberto; LÓPEZ, Alberto; DE LA TORRE, Nieves. Evaluating the effect of a driver's behaviour on the range of a battery electric vehicle. **Proceedings of the Institution of Mechanical Engineers, Part D: Journal of Automobile Engineering**, SAGE Publications Sage UK: London, England, v. 229, n. 10, p. 1379–1391, 2015.

ANDERSSON, Joel AE; ÅKESSON, Johan; DIEHL, Moritz. CasADi: A symbolic package for automatic differentiation and optimal control. In: SPRINGER. RECENT advances in algorithmic differentiation. [S.l.: s.n.], 2012. P. 297–307.

ANDERSSON, Joel AE; GILLIS, Joris, et al. CasADi: a software framework for nonlinear optimization and optimal control. **Mathematical Programming Computation**, Springer, v. 11, p. 1–36, 2019.

ANSEÁN, David et al. Lithium-ion battery degradation indicators via incremental capacity analysis. **IEEE Transactions on Industry Applications**, IEEE, v. 55, n. 3, p. 2992–3002, 2019.

ARAUJO, Lucas S et al. Smartbattery: An active-battery solution for energy storage system. In: IEEE. 2019 IEEE 15th Brazilian Power Electronics Conference and 5th IEEE Southern Power Electronics Conference (COBEP/SPEC). [S.l.: s.n.], 2019. P. 1–6.

ATALAY, Selcuk et al. Theory of battery ageing in a lithium-ion battery: Capacity fade, nonlinear ageing and lifetime prediction. **Journal of Power Sources**, Elsevier, v. 478, p. 229026, 2020.

AYKOL, Muratahan et al. Perspective—combining physics and machine learning to predict battery lifetime. **Journal of The Electrochemical Society**, IOP Publishing, v. 168, n. 3, p. 030525, 2021.

AZIZIGHALEHSARI, S et al. Battery Dynamics Exploration: Insights and Implications of Relaxation Time in Electrochemical Impedance Spectroscopy. In: IEEE. 2023 IEEE 8th Southern Power Electronics Conference (SPEC). [S.l.: s.n.], 2023. P. 1–6.

AZIZIGHALEHSARI, Seyedreza et al. A Review of Lithium-ion Batteries Diagnostics and Prognostics Challenges. In: IEEE. IECON 2021–47th Annual Conference of the IEEE Industrial Electronics Society. [S.l.: s.n.], 2021. P. 1–6.

BADLAM, Justin et al. The Inflation Reduction Act: Here's what's in it. **McKinsey's Public Sector Practice**, 2022. Available at https://www.mckinsey.com/industries/public-sector/our-insights/the-inflation-reduction-act-heres-whats-in-it.

BAEK, Sun Woong et al. Thermodynamic analysis and interpretative guide to entropic potential measurements of lithium-ion battery electrodes. **The Journal of Physical Chemistry C**, ACS Publications, v. 126, n. 14, p. 6096–6110, 2022.

BAGHDADI, Issam et al. Lithium battery aging model based on Dakin's degradation approach. **Journal of Power Sources**, Elsevier, v. 325, p. 273–285, 2016.

BAUMANN, Michael; ROHR, Stephan; LIENKAMP, Markus. Cloud-connected battery management for decision making on second-life of electric vehicle batteries. In: IEEE. 2018 Thirteenth International Conference on Ecological Vehicles and Renewable Energies (EVER). [S.l.: s.n.], 2018. P. 1–6.

BERGER, Katharina; SCHÖGGL, Josef-Peter; BAUMGARTNER, Rupert J. Digital battery passports to enable circular and sustainable value chains: Conceptualization and use cases. **Journal of Cleaner Production**, Elsevier, v. 353, p. 131492, 2022.

BHATTI, Ghanishtha; MOHAN, Harshit; SINGH, R Raja. Towards the future of smart electric vehicles: Digital twin technology. **Renewable and Sustainable Energy Reviews**, Elsevier, v. 141, p. 110801, 2021.

BLOOM, Ira et al. Differential voltage analyses of high-power, lithium-ion cells: 1. Technique and application. **Journal of Power Sources**, Elsevier, v. 139, n. 1-2, p. 295–303, 2005.

BLOOMBERGNEF. Lithium-ion Battery Pack Prices Rise for First Time to an Average of $151/kWh$, 2022.

BOJ, E Aguilar et al. A distribution of relaxation time approach on equivalent circuit model parameterization to analyse li-ion battery degradation. In: IEEE. 2023 11th International Conference on Power Electronics and ECCE Asia (ICPE 2023-ECCE Asia). [S.l.: s.n.], 2023. P. 1403–1409.

BRADBURY, James et al. **JAX: composable transformations of Python+NumPy programs**. [S.l.: s.n.], 2018. Availiable at http://github.com/google/jax.

BROUSSELY, Michel et al. Main aging mechanisms in Li ion batteries. **Journal of power sources**, Elsevier, v. 146, n. 1-2, p. 90–96, 2005.

BYD. **BYD D9W 20.410 Datasheet**. [S.l.], 2022. https://www.byd.com.br/wp-content/uploads/2022/03/BYD-D9W-20.410-v.-7.0-2022.pdf.

CANALS CASALS, Lluc; AMANTE GARCÍA, Beatriz; GONZÁLEZ BENÍTEZ, Maria Margarita. A Cost Analysis of Electric Vehicle Batteries Second Life Businesses. In: **Project Management and Engineering Research, 2014: Selected Papers from the 18th International AEIPRO Congress held in Alcañiz, Spain, in 2014**. Ed. by José Luis Ayuso Muñoz, José Luis Yagüe Blanco and Salvador F. Capuz-Rizo. Cham: Springer International Publishing, 2016. P. 129–141. ISBN 978-3-319-26459-2. DOI: 10.1007/978-3-319-26459-2_10. Available from: <https://doi.org/10.1007/978-3-319-26459-2_10>.

CASALS, Lluc Canals; GARCÍA, B Amante; CANAL, Camille. Second life batteries lifespan: Rest of useful life and environmental analysis. **Journal of environmental management**, Elsevier, v. 232, p. 354–363, 2019.

CHEN, Chang-Hui et al. Development of experimental techniques for parameterization of multi-scale lithium-ion battery models. **Journal of The Electrochemical Society**, IOP Publishing, v. 167, n. 8, p. 080534, 2020.

CHEN, Yuxin et al. Operando detection of Li plating during fast charging of Li-ion batteries using incremental capacity analysis. **Journal of Power Sources**, Elsevier, v. 539, p. 231601, 2022.

CHOI, Woosung et al. Modeling and applications of electrochemical impedance spectroscopy (EIS) for lithium-ion batteries. **Journal of Electrochemical Science and Technology**, The Korean Electrochemical Society, v. 11, n. 1, p. 1–13, 2020.

CHRISTOPHERSEN, Jon P. **Battery test manual for electric vehicles, revision 3**. [S.l.], 2015.

COUNCIL OF EUROPEAN UNION. **Regulation (EU) 2023/1542 – "New batteries regulation"**. [S.l.: s.n.], 2023. https://eur-lex.europa.eu/eli/reg/2023/1542/oj.

DAHN, Hannah M et al. User-friendly differential voltage analysis freeware for the analysis of degradation mechanisms in Li-ion batteries. **Journal of The Electrochemical Society**, IOP Publishing, v. 159, n. 9, a1405, 2012.

DAVENPORT, Coral; FRIEDMAN, Lisa; PLUMER, Brad. California to Ban the Sale of New Gasoline Cars. **The New York Times**, Aug. 2022. Available from: <https://www.nytimes.com/2022/08/24/climate/california-gas-cars-emissions.html>.

DICKINSON, Edmund J.F.; WAIN, Andrew J. The Butler-Volmer equation in electrochemical theory: Origins, value, and practical application. **Journal of Electroanalytical Chemistry**, v. 872, p. 114145, 2020. Dr. Richard Compton 65th birthday Special issue. ISSN 1572-6657. DOI: https://doi.org/10.1016/j.jelechem.2020.114145. Available from: <https://www.sciencedirect.com/science/article/pii/S1572665720303283>.

DIEKMANN, Jan; KWADE, Arno. **Recycling of lithium-ion batteries: The LithoRec Way**. [S.l.]: Springer, 2018.

DOE. **Energe storage grand challenge roadmap**. [S.l.], 2020.

DOMENICO, Domenico Di; STEFANOPOULOU, Anna; FIENGO, Giovanni. Lithium-ion battery state of charge and critical surface charge estimation using an electrochemical model-based extended Kalman filter. **Journal of Dynamic Systems, Measurement and Control, Transactions of the ASME**, American Society of Mechanical Engineers Digital Collection, v. 132, p. 2565–2578, 6 Nov. 2010. ISSN 00220434. DOI: 10.1115/1.4002475/470149. Available from: <https://dx.doi.org/10.1115/1.4002475>.

DOYLE, Marc; FULLER, Thomas F; NEWMAN, John. Modeling of galvanostatic charge and discharge of the lithium/polymer/insertion cell. **Journal of the Electrochemical society**, IOP Publishing, v. 140, n. 6, p. 1526, 1993.

DUBARRY, Matthieu; ANSEÁN, David. Best practices for incremental capacity analysis. **Frontiers in Energy Research**, Frontiers, v. 10, p. 1023555, 2022.

DUBARRY, Matthieu; BAURE, George. Perspective on commercial Li-ion battery testing, best practices for simple and effective protocols. **Electronics**, MDPI, v. 9, n. 1, p. 152, 2020.

DUBARRY, Matthieu; BAURE, George; DEVIE, Arnaud. Durability and reliability of EV batteries under electric utility grid operations: Path dependence of battery degradation. **Journal of The Electrochemical Society**, IOP Publishing, v. 165, n. 5, a773, 2018.

DUBARRY, Matthieu; SVOBODA, Vojtech, et al. Incremental capacity analysis and close-to-equilibrium OCV measurements to quantify capacity fade in commercial rechargeable lithium batteries. **Electrochemical and solid-state letters**, IOP Publishing, v. 9, n. 10, a454, 2006.

EDDY, Melissa. European Union to Ban Gas-Powered Cars by 2035. **The New York Times**, Feb. 2023. Available from: <https://www.nytimes.com/2023/02/14/world/europe/eu-gas-powered-cars-ban.html>.

EDGE, Jacqueline S et al. Lithium ion battery degradation: what you need to know. **Physical Chemistry Chemical Physics**, Royal Society of Chemistry, v. 23, n. 14, p. 8200–8221, 2021.

EHSANI, Mehrdad et al. **Modern electric, hybrid electric, and fuel cell vehicles**. [S.l.]: CRC press, 2018.

FANG, Weifeng; KWON, Ou Jung; WANG, Chao-Yang. Electrochemical–thermal modeling of automotive Li-ion batteries and experimental validation using a three-electrode cell. **International journal of energy research**, Wiley Online Library, v. 34, n. 2, p. 107–115, 2010.

FCAB. **National Blueprint for Lithium Batteries (2021-2030)**. [S.l.], 2021.

FIELD, Kyle. BloombergNEF: Lithium-Ion Battery Cell Densities Have Almost Tripled Since 2010. **Clean Technica**, 2020.

FORGEZ, Christophe et al. Thermal modeling of a cylindrical LiFePO4/graphite lithium-ion battery. **Journal of power sources**, Elsevier, v. 195, n. 9, p. 2961–2968, 2010.

FULLER, Thomas F; DOYLE, Marc; NEWMAN, John. Simulation and optimization of the dual lithium ion insertion cell. **Journal of the electrochemical society**, IOP Publishing, v. 141, n. 1, p. 1, 1994.

GABBAR, Hossam A; OTHMAN, Ahmed M; ABDUSSAMI, Muhammad R. Review of battery management systems (BMS) development and industrial standards. **Technologies**, MDPI, v. 9, n. 2, p. 28, 2021.

GALLAGHER, Kevin G; NELSON, Paul A; DEES, Dennis W. Simplified calculation of the area specific impedance for battery design. **Journal of Power Sources**, Elsevier, v. 196, n. 4, p. 2289–2297, 2011.

GANESH, Sai Vinayak; D'ARPINO, Matilde. Critical Comparison of Li-Ion Aging Models for Second Life Battery Applications. **Energies**, MDPI, v. 16, n. 7, p. 3023, 2023.

GARCHE, Jürgen et al. **Encyclopedia of electrochemical power sources**. [S.l.]: Newnes, 2013.

GONG, Zhe et al. An EV-Scale Demonstration of In-Situ Battery Electrochemical Impedance Spectroscopy and BMS-Limited Pack Performance Analysis. **IEEE Transactions on Industrial Electronics**, IEEE, v. 70, n. 9, p. 9112–9122, 2022.

GOODENOUGH, John B. How we made the Li-ion rechargeable battery. **Nature Electronics**, Nature Publishing Group UK London, v. 1, n. 3, p. 204–204, 2018.

GU, Ran; MALYSZ, Pawel, et al. On the suitability of electrochemical-based modeling for lithium-ion batteries. **IEEE Transactions on Transportation Electrification**, Institute of

Electrical and Electronics Engineers Inc., v. 2, p. 417–431, 4 Dec. 2016. ISSN 23327782. DOI: 10.1109/TTE.2016.2571778.

GU, WB; WANG, CY. Thermal-electrochemical modeling of battery systems. **Journal of The Electrochemical Society**, IOP Publishing, v. 147, n. 8, p. 2910, 2000.

GUHA, Arijit; PATRA, Amit. Online estimation of the electrochemical impedance spectrum and remaining useful life of lithium-ion batteries. **IEEE Transactions on Instrumentation and Measurement**, IEEE, v. 67, n. 8, p. 1836–1849, 2018.

GUO, Meng; SIKHA, Godfrey; WHITE, Ralph E. Single-particle model for a lithium-ion cell: Thermal behavior. **Journal of The Electrochemical Society**, IOP Publishing, v. 158, n. 2, a122, 2010.

HAN, Sangwoo; TANG, Yifan; RAHIMIAN, Saeed Khaleghi. A numerically efficient method of solving the full-order pseudo-2-dimensional (P2D) Li-ion cell model. **Journal of Power Sources**, Elsevier, v. 490, p. 229571, Apr. 2021. ISSN 0378-7753. DOI: 10.1016/J.JPOWSOUR.2021.229571.

HAN, Xuebing; LU, Languang, et al. A review on the key issues of the lithium ion battery degradation among the whole life cycle. **ETransportation**, Elsevier, v. 1, p. 100005, 2019.

HARAM, Mohammed Hussein Saleh Mohammed et al. Feasibility of utilising second life EV batteries: Applications, lifespan, economics, environmental impact, assessment, and challenges. **Alexandria Engineering Journal**, Elsevier, v. 60, n. 5, p. 4517–4536, 2021.

HARIHARAN, Krishnan S.; TAGADE, Piyush; RAMACHANDRAN, Sanoop. Theoretical Framework of the Electrochemical Model. In: MATHEMATICAL Modeling of Lithium Batteries: From Electrochemical Models to State Estimator Algorithms. [S.l.]: Springer Nature, 2018. chap. 2, p. 13–32. ISBN 978-3-319-03526-0. DOI: 10.1007/978-3-319-03527-7. Available from: <http://www.springer.com/series/8059>.

HARPER, Gavin et al. Recycling lithium-ion batteries from electric vehicles. **nature**, Nature Publishing Group, v. 575, n. 7781, p. 75–86, 2019.

HESSE, Holger C et al. Economic optimization of component sizing for residential battery storage systems. **Energies**, MDPI, v. 10, n. 7, p. 835, 2017.

HINDMARSH, Alan C et al. SUNDIALS: Suite of nonlinear and differential/algebraic equation solvers. **ACM Transactions on Mathematical Software (TOMS)**, ACM New York, NY, USA, v. 31, n. 3, p. 363–396, 2005.

HOWEY, David. SLIDE: Linux-compatible initial release. **Zenodo**, 2019. Availiable at doi.org/10.5281/zenodo.2848823.

HU, Xiaosong; DENG, Xinchen, et al. A review of second-life lithium-ion batteries for stationary energy storage applications. **Proceedings of the IEEE**, IEEE, v. 110, n. 6, p. 735–753, 2022.

HU, Xiaosong; FENG, Fei, et al. State estimation for advanced battery management: Key challenges and future trends. **Renewable and Sustainable Energy Reviews**, Elsevier, v. 114, p. 109334, 2019.

HU, Xiaosong; LI, Shengbo; PENG, Huei. A comparative study of equivalent circuit models for Li-ion batteries. **Journal of Power Sources**, Elsevier, v. 198, p. 359–367, 2012.

HU, Xiaosong; XU, Le, et al. Battery lifetime prognostics. **Joule**, Elsevier, v. 4, n. 2, p. 310–346, 2020.

INTERNATIONAL ENERGY AGENCY. **Trends in electric vehicle batteries**. [S.l.: s.n.], 2024. Available at: https://www.iea.org/reports/global-ev-outlook-2024/trends-in-electric-vehicle-batteries.

JALKANEN, K et al. Cycle aging of commercial NMC/graphite pouch cells at different temperatures. **Applied Energy**, Elsevier, v. 154, p. 160–172, 2015.

JIN, Xing. Aging-Aware optimal charging strategy for lithium-ion batteries: Considering aging status and electro-thermal-aging dynamics. **Electrochimica Acta**, v. 407, p. 139651, 2022. ISSN 0013-4686. DOI: https://doi.org/10.1016/j.electacta.2021.139651. Available from: <https://www.sciencedirect.com/science/article/pii/S0013468621019356>.

JONES, David et al. Characterising the Digital Twin: A systematic literature review. **CIRP journal of manufacturing science and technology**, Elsevier, v. 29, p. 36–52, 2020.

KALUPSON, Jim; LUO, Gang; SHAFFER, Christian E. AutoLion™: A Thermally Coupled Simulation Tool for Automotive Li-Ion Batteries. In: SAE 2013 World Congress Exhibition. [S.l.]: SAE International, Apr. 2013. DOI: https://doi.org/10.4271/2013-01-1522. Available from: <https://doi.org/10.4271/2013-01-1522>.

KAMPKER, Achim et al. Battery pack remanufacturing process up to cell level with sorting and repurposing of battery cells. **Journal of Remanufacturing**, Springer, v. 11, p. 1–23, 2021.

KANE, Mark. China: Nearly 6 Million Plug-In Cars Were Sold In 2022. **InsideEVs**, Feb. 2023. Available at: https://insideevs.com/news/651363/china-plugin-car-sales-december2022/.

KANE, Mark. Europe: Plug-In Car Sales Reached Spectacular Record in December 2022. **InsideEVs**, Feb. 2023. Available from: <https://insideevs.com/news/651295/europe-plugin-car-sales-december2022/>.

KANE, Mark. EV Battery Market: LFP Chemistry Reached 31% Share In September. **InsideEVs**, 2022. Available at: https://insideevs.com/news/628303/ev-battery-lfp-share-september2022/.

KLETT, Matilda; ERIKSSON, Rickard, et al. Non-uniform aging of cycled commercial LiFePO4//graphite cylindrical cells revealed by post-mortem analysis. **Journal of Power Sources**, Elsevier, v. 257, p. 126–137, 2014.

KLETT, Matilda; SVENS, Pontus, et al. Uneven film formation across depth of porous graphite electrodes in cycled commercial Li-ion batteries. **The Journal of Physical Chemistry C**, ACS Publications, v. 119, n. 1, p. 90–100, 2015.

KOLETI, Upender Rao; DINH, Truong Quang; MARCO, James. A new on-line method for lithium plating detection in lithium-ion batteries. **Journal of Power Sources**, Elsevier, v. 451, p. 227798, 2020.

KRUPP, Amelie et al. Incremental capacity analysis as a state of health estimation method for lithium-ion battery modules with series-connected cells. **Batteries**, MDPI, v. 7, n. 1, p. 2, 2020.

KUIPERS, Matthias et al. An algorithm for an online electrochemical impedance spectroscopy and battery parameter estimation: Development, verification and validation. **Journal of Energy Storage**, Elsevier, v. 30, p. 101517, 2020.

LACAP, Joseph; PARK, Jae Wan; BESLOW, Lucas. Development and Demonstration of Microgrid System Utilizing Second-Life Electric Vehicle Batteries. **Journal of Energy Storage**, Elsevier, v. 41, p. 102837, Sept. 2021. ISSN 2352-152X. DOI: 10.1016/J.EST.2021.102837.

LAZANAS, Alexandros Ch; PRODROMIDIS, Mamas I. Electrochemical Impedance Spectroscopy A Tutorial. **ACS Measurement Science Au**, ACS Publications, 2023.

LEE, Seong Beom; ONORI, Simona. A Robust and Sleek Electrochemical Battery Model Implementation: A MATLAB® Framework. **Journal of the Electrochemical Society**, v. 168.9, 2021. DOI: 10.1149/1945-7111/ac22c8.

LEE, Seong Beom; ONORI, Simona. A robust and sleek electrochemical battery model implementation: a MATLAB® framework. **Journal of The Electrochemical Society**, IOP Publishing, v. 168, n. 9, p. 090527, 2021.

LG CHEM. **LG INR21700 M50T Product specification datasheet**. [S.l.: s.n.], 2018. https://www.batteryspace.com/prod-specs/11514.pdf. Acessed on 10-06-2024.

LI, Jichun; CHEN, Yi-Tung. **Computational Partial Differential Equations Using MATLAB®**. 1st. [S.l.]: Chapman and Hall/CRC, 2008.

LI, Junqiu. **Modeling and simulation of lithium-ion power battery thermal management**. [S.l.]: Springer, 2022.

LI, Ruihe; O'KANE, Simon, et al. A million cycles in a day: Enabling high-throughput computing of lithium-ion battery degradation with physics-based models. **Journal of Power Sources**, Elsevier, v. 598, p. 234184, 2024.

LIU, Lei et al. Vehicular edge computing and networking: A survey. **Mobile networks and applications**, Springer, v. 26, p. 1145–1168, 2021.

LUTSEY, Nic; NICHOLAS, Michael. Update on electric vehicle costs in the United States through 2030. **Int. Counc. Clean Transp**, v. 12, p. 1–12, 2019.

MAISEL, Franziska et al. A forecast on future raw material demand and recycling potential of lithium-ion batteries in electric vehicles. **Resources, Conservation and Recycling**, Elsevier, v. 192, p. 106920, 2023.

MARQUIS, Scott George. **Long-term degradation of lithium-ion batteries**. 2020. PhD thesis – University of Oxford.

MARTINEZ-LASERNA, Egoitz; GANDIAGA, Iñigo, et al. Battery second life: Hype, hope or reality? A critical review of the state of the art. **Renewable and Sustainable Energy Reviews**, Elsevier, v. 93, p. 701–718, 2018.

MARTINEZ-LASERNA, Egoitz; SARASKETA-ZABALA, Elixabet, et al. Technical viability of battery second life: A study from the ageing perspective. **IEEE Transactions on Industry Applications**, IEEE, v. 54, n. 3, p. 2703–2713, 2018.

MATHEWS, Ian et al. Technoeconomic model of second-life batteries for utility-scale solar considering calendar and cycle aging. **Applied energy**, Elsevier, v. 269, p. 115127, 2020.

MATHWORKS. **Drive Cycle Source**. [S.l.: s.n.], 2017. Available from: <https://www.mathworks.com/help/autoblks/ref/drivecyclesource.html>.

MIRI, Ilyès; FOTOUHI, Abbas; EWIN, Nathan. Electric vehicle energy consumption modelling and estimation—A case study. **International Journal of Energy Research**, Wiley Online Library, v. 45, n. 1, p. 501–520, 2021.

MOURA, Scott J et al. Battery state estimation for a single particle model with electrolyte dynamics. **IEEE Transactions on Control Systems Technology**, IEEE, v. 25, n. 2, p. 453–468, 2016.

MU, Hao et al. A novel fractional order model based state-of-charge estimation method for lithium-ion battery. **Applied Energy**, Elsevier, v. 207, p. 384–393, 2017.

MÜLLER, Daniel; DUFAUX, Thomas; BIRKE, Kai Peter. Model-based investigation of porosity profiles in graphite anodes regarding sudden-death and second-life of lithium ion cells. **Batteries**, MDPI, v. 5, n. 2, p. 49, 2019.

NEUBAUER, Jeremy. **Battery lifetime analysis and simulation tool (BLAST) documentation**. [S.l.], 2014.

NEUBAUER, Jeremy; SIMPSON, Mike. **Deployment of behind-the-meter energy storage for demand charge reduction**. [S.l.], 2015.

NEUBAUER, Jeremy; SMITH, K, et al. **Identifying and overcoming critical barriers to widespread second use of PEV batteries**. [S.l.], 2015.

NEUBAUER, Jeremy; WOOD, Eric. Thru-life impacts of driver aggression, climate, cabin thermal management, and battery thermal management on battery electric vehicle utility. **Journal of Power Sources**, Elsevier, v. 259, p. 262–275, 2014.

NEWMAN, John. Fortran Programs for the Simulation of Electrochemical Systems (DUALFOIL), 1998. Available at http//www.cchem.berkeley.edu/jsngrp.

NEWMAN, John; BALSARA, Nitash P. **Electrochemical systems**. [S.l.]: John Wiley & Sons, 2021.

NICOLAS, Romain. **The different driving cycles**. [S.l.: s.n.], 2013. Available from: <https://www.car-engineer.com/the-different-driving-cycles/>.

NING, Gang; POPOV, Branko N. Cycle life modeling of lithium-ion batteries. **Journal of The Electrochemical Society**, IOP Publishing, v. 151, n. 10, a1584, 2004.

NYKVIST, Björn; NILSSON, Måns. Rapidly falling costs of battery packs for electric vehicles. **Nature climate change**, Nature Publishing Group, v. 5, n. 4, p. 329–332, 2015.

NYMAN, Andreas; EKSTRÖM, Henrik; FONTES, Ed. **Modeling the Lithium-Ion Battery**. [S.l.], 2012.

NYMAN, Andreas; EKSTRÖM, Henrik; FONTES, Ed. Multiphysics Simulation for the Design of Lithium Ion Batteries. **IEEE Spectrum**, 2017.

O'KANE, Simon EJ et al. Lithium-ion battery degradation: how to model it. **Physical Chemistry Chemical Physics**, Royal Society of Chemistry, v. 24, n. 13, p. 7909–7922, 2022.

O'KANE, Simon EJ et al. Physical origin of the differential voltage minimum associated with lithium plating in Li-ion batteries. **Journal of The Electrochemical Society**, IOP Publishing, v. 167, n. 9, p. 090540, 2020.

OGUMI, Zempachi.; INABA, Minoru. Carbon Anodes. In: ADVANCES in Lithium-ion Batteries. [S.l.]: Kluwer Academic Publisher, 2002. chap. 2.

OLIVEIRA, Victor Manuel Riva de et al. Electric Vehicles Modeling: A Review. In: IEEE. 2023 15th IEEE International Conference on Industry Applications (INDUSCON). [S.l.: s.n.], 2023. P. 285–292.

OZPINECI, Burak. **Oak Ridge National Laboratory annual progress report for the electric drive technologies program**. [S.l.], 2015.

PAUL, Sebastian et al. Analysis of ageing inhomogeneities in lithium-ion battery systems. **Journal of Power Sources**, Elsevier, v. 239, p. 642–650, 2013.

PONTES, José. 22% of New Car Sales in China Were 100% Electric in 2022! **CleanTechnica**, Feb. 2023. Available from: <https://cleantechnica.com/2023/02/01/plugin-electric-vehicles-get-30-share-of-auto-market-in-another-record-month-in-china/>.

PRADA, Eric. **Aging modeling and lifetime optimization of Li-ion LiFePO4-graphite batteries according to the vehicle use.** 2012. PhD thesis – Université Pierre et Marie Curie.

PRADA, Eric et al. A simplified electrochemical and thermal aging model of LiFePO4-graphite Li-ion batteries: Power and capacity fade simulations. **Journal of The Electrochemical Society**, IOP Publishing, v. 160, n. 4, a616, 2013.

PREGER, Yuliya; TORRES-CASTRO, Loraine; MCDOWALL, Jim, et al. Lithium-ion Batteries. In: 2020 USDOE Energy Storage Handbook. [S.l.: s.n.], 2023.

PYBAMM. **Modelling coupled degradation mechanisms in PyBaMM**. [S.l.: s.n.], 2022. https://docs.pybamm.org/en/latest/source/examples/notebooks/models/coupled-degradation.html.

PYBAMM, Team. liionpack Documentation, 2024. Avaliable online: https://liionpack.readthedocs.io/en/latest/ (Accessed 07/07/2024).

PYBAMM, Team. PyBaMM documentation - version 24.1, 2024. Avaliable online: https://docs.pybamm.org/en/latest/index.html (Accessed 30/05/2024).

QIAN, Kun et al. State-of-health (SOH) evaluation on lithium-ion battery by simulating the voltage relaxation curves. **Electrochimica Acta**, Elsevier, v. 303, p. 183–191, 2019.

RAJ, Trishna et al. Investigation of path-dependent degradation in lithium-ion batteries. **Batteries & Supercaps**, Wiley Online Library, v. 3, n. 12, p. 1377–1385, 2020.

RALLO, Héctor et al. Economic analysis of the disassembling activities to the reuse of electric vehicles Li-ion batteries. **Resources, conservation and recycling**, Elsevier, v. 159, p. 104785, 2020.

RAMADESIGAN, Venkatasailanathan et al. Efficient reformulation of solid-phase diffusion in physics-based lithium-ion battery models. **Journal of The Electrochemical Society**, IOP Publishing, v. 157, n. 7, a854, 2010.

RAN, Aihua et al. Data-Driven Fast Clustering of Second-Life Lithium-Ion Battery: Mechanism and Algorithm. **Advanced Theory and Simulations**, Wiley Online Library, v. 3, n. 8, p. 2000109, 2020.

RAO, Lin; NEWMAN, John. Heat-generation rate and general energy balance for insertion battery systems. **Journal of the Electrochemical Society**, IOP Publishing, v. 144, n. 8, p. 2697, 1997.

RECHKEMMER, Sabrina Kathrin et al. Empirical Li-ion aging model derived from single particle model. **Journal of Energy Storage**, Elsevier, v. 21, p. 773–786, 2019.

REID, Gerard; JULVE, Javier. Second life-batterien als flexible speicher für erneuerbare energien. **Kurzstudie im Auftrag des Bundesverbandes Erneuerbarer Energien e. V. und der Hannover Messe**, 2016.

RENIERS, Jorn M; MULDER, Grietus; HOWEY, David A. Review and performance comparison of mechanical-chemical degradation models for lithium-ion batteries. **Journal of The Electrochemical Society**, The Electrochemical Society, v. 166, n. 14, a3189–a3200, 2019.

RENIERS, Jorn M; MULDER, Grietus; OBER-BLÖBAUM, Sina, et al. Improving optimal control of grid-connected lithium-ion batteries through more accurate battery and degradation modelling. **Journal of Power Sources**, Elsevier, v. 379, p. 91–102, 2018.

RICHARDSON, G. W. et al. Charge transport modelling of Lithium-ion batteries. **European Journal of Applied Mathematics**, Cambridge University Press, v. 33, p. 983–1031, 6 2022. ISSN 0956-7925. DOI: 10.1017/S0956792521000292. Available from: <https://www.cambridge.org/core/journals/european-journal-of-applied-mathematics/article/charge-transport-modelling-of-lithiumion-batteries/02E493C747DE30A4709615B71EF3E56D>.

RIFFONNEAU, Yann et al. Optimal power flow management for grid connected PV systems with batteries. **IEEE Transactions on sustainable energy**, IEEE, v. 2, n. 3, p. 309–320, 2011.

RITCHIE, Hannah. Cars, planes, trains: where do CO_2 emissions from transport come from? **Our World in Data**, 2020. https://ourworldindata.org/co2-emissions-from-transport.

RIVIERE, Elie et al. Innovative incremental capacity analysis implementation for C/LiFePO4 cell state-of-health estimation in electrical vehicles. **Batteries**, MDPI, v. 5, n. 2, p. 37, 2019.

ROBERTS, David; LASHOF, Daniel A. What's going on with biofuels? **Volts**, 2023. https://www.volts.wtf/p/whats-going-on-with-biofuels.

SAFARI, M et al. Multimodal physics-based aging model for life prediction of Li-ion batteries. **Journal of The Electrochemical Society**, IOP Publishing, v. 156, n. 3, a145, 2008.

SAMANTA, Akash; WILLIAMSON, Sheldon S. A survey of wireless battery management system: Topology, emerging trends, and challenges. **Electronics**, MDPI, v. 10, n. 18, p. 2193, 2021.

SANTHANAGOPALAN, Shriram et al. Review of models for predicting the cycling performance of lithium ion batteries. **Journal of power sources**, Elsevier, v. 156, n. 2, p. 620–628, 2006.

SATHRE, Roger et al. Energy and climate effects of second-life use of electric vehicle batteries in California through 2050. **Journal of Power Sources**, Elsevier, v. 288, p. 82–91, Aug. 2015. ISSN 0378-7753. DOI: 10.1016/J.JPOWSOUR.2015.04.097.

SAUER, Dirk Uwe; WENZL, Heinz. Comparison of different approaches for lifetime prediction of electrochemical systems—Using lead-acid batteries as example. **Journal of Power sources**, Elsevier, v. 176, n. 2, p. 534–546, 2008.

SCHUSTER, Simon F; BACH, Tobias, et al. Nonlinear aging characteristics of lithium-ion cells under different operational conditions. **Journal of Energy Storage**, Elsevier, v. 1, p. 44–53, 2015.

SCHUSTER, Simon F; BRAND, Martin J, et al. Lithium-ion cell-to-cell variation during battery electric vehicle operation. **Journal of Power Sources**, Elsevier, v. 297, p. 242–251, 2015.

SINGLE, Fabian; LATZ, Arnulf; HORSTMANN, Birger. Identifying the mechanism of continued growth of the solid–electrolyte interphase. **ChemSusChem**, Wiley Online Library, v. 11, n. 12, p. 1950–1955, 2018.

SMITH, Kandler; WANG, Chao Yang. Power and thermal characterization of a lithium-ion battery pack for hybrid-electric vehicles. **Journal of Power Sources**, Elsevier, v. 160, p. 662–673, 1 Sept. 2006. ISSN 0378-7753. DOI: 10.1016/J.JPOWSOUR.2006.01.038.

SRINIVASAN, Venkat; WANG, Chao-Yang. Analysis of electrochemical and thermal behavior of Li-ion cells. **Journal of The Electrochemical Society**, IOP Publishing, v. 150, n. 1, a98, 2002.

SUBRAMANIAN, Venkat R; DIWAKAR, Vinten D; TAPRIYAL, Deepak. Efficient macro-micro scale coupled modeling of batteries. **Journal of The Electrochemical Society**, IOP Publishing, v. 152, n. 10, a2002, 2005.

SUBRAMANIAN, Venkat R; RITTER, James A; WHITE, Ralph E. Approximate solutions for galvanostatic discharge of spherical particles I. Constant diffusion coefficient. **Journal of The Electrochemical Society**, IOP Publishing, v. 148, n. 11, e444, 2001.

SULZER, Valentin et al. Python battery mathematical modelling (PyBaMM). **Journal of Open Research Software**, Ubiquity Press, v. 9, n. 1, 2021.

TANIM, Tanvir R et al. Advanced diagnostics to evaluate heterogeneity in lithium-ion battery modules. **ETransportation**, Elsevier, v. 3, p. 100045, 2020.

TAYLOR, SR; GILEADI, E. Physical interpretation of the Warburg impedance. **Corrosion**, OnePetro, v. 51, n. 09, 1995.

THOMAS, Karen E; NEWMAN, John; DARLING, Robert M. Mathematical modeling of lithium batteries. In: ADVANCES in Lithium-ion Batteries. [S.l.]: Kluwer Academic Publisher, 2002. chap. 12.

TIMMS, Robert et al. Asymptotic reduction of a lithium-ion pouch cell model. **SIAM Journal on Applied Mathematics**, SIAM, v. 81, n. 3, p. 765–788, 2021.

TORCHIO, Marcello et al. Lionsimba: a matlab framework based on a finite volume model suitable for li-ion battery design, simulation, and control. **Journal of The Electrochemical Society**, IOP Publishing, v. 163, n. 7, a1192, 2016.

TRANTER, Thomas G. **PyBaMM Simulink integration example**. [S.l.: s.n.], 2021. https://github.com/FaradayInstitution/pybamm_simulink_example.

USABC; HUNT, Gary. Electric vehicle battery test procedures manual. **United States Department of Energy: Washington, DC, USA**, 1996.

VENKATAPATHY, Karthik; TAZELAAR, Edwin; VEENHUIZEN, Bram. A systematic identification of first to second life shift-point of lithium-ion batteries. In: IEEE. 2015 IEEE Vehicle Power and Propulsion Conference (VPPC). [S.l.: s.n.], 2015. P. 1–4.

VIRTANEN, Pauli et al. SciPy 1.0: fundamental algorithms for scientific computing in Python. **Nature methods**, Nature Publishing Group, v. 17, n. 3, p. 261–272, 2020.

VITALLI, Rogério Adas Pereira; MOREIRA, João Manoel Losada. Digital Twin of a Robotic Sytem for Measuring Pipe Wall Thickness in Nuclear Power Plants. In: IEEE. 2023 15th IEEE International Conference on Industry Applications (INDUSCON). [S.l.: s.n.], 2023. P. 1191–1194.

WAAG, Wladislaw; KÄBITZ, Stefan; SAUER, Dirk Uwe. Experimental investigation of the lithium-ion battery impedance characteristic at various conditions and aging states and its influence on the application. **Applied energy**, Elsevier, v. 102, p. 885–897, 2013.

WALDMANN, Thomas et al. Temperature dependent ageing mechanisms in Lithium-ion batteries–A Post-Mortem study. **Journal of power sources**, Elsevier, v. 262, p. 129–135, 2014.

WANG, A. A. et al. Review of parameterisation and a novel database (LiionDB) for continuum Li-ion battery models. **Progress in Energy**, IOP Publishing, v. 4, p. 032004, 3 May 2022. ISSN 2516-1083. DOI: 10.1088/2516-1083/AC692C. Available from: <https://iopscience.iop.org/article/10.1088/2516-1083/ac692c%20https://iopscience.iop.org/article/10.1088/2516-1083/ac692c/meta>.

WANG, Andrew; SULZER, V. **Liiondb**. [S.l.: s.n.], 2021. URL: https://liiondb.com/. Available from: <https://liiondb.com/>.

WANG, Limei et al. On-board state of health estimation of LiFePO4 battery pack through differential voltage analysis. **Applied energy**, Elsevier, v. 168, p. 465–472, 2016.

WANG, Shunli et al. **Battery system modeling**. [S.l.]: Elsevier, 2021.

WARNER, John T. **The handbook of lithium-ion battery pack design: chemistry, components, types and terminology**. [S.l.]: Elsevier, 2015.

WHAIDUZZAMAN, Md et al. A survey on vehicular cloud computing. **Journal of Network and Computer applications**, Elsevier, v. 40, p. 325–344, 2014.

WHITE, Annie. Here Are All the Promises Automakers Have Made about Electric Cars. **Car and Driver**, Feb. 2021. Available from: <https://www.caranddriver.com/news/g35562831/ev-plans-automakers-timeline/>.

WHITE HOUSE. Building a Clean Energy Economy: A guidebook to the Inflation Reduction Act's investments in clean energy and climate action. **White-House. U.S. government**, 2023. Available at https://www.whitehouse.gov/wp-content/uploads/2022/12/Inflation-Reduction-Act-Guidebook.

WORLD ECONOMIC FORUM. A Vision for a Sustainable Battery Value Chain in 2030 Report, Sept. 2019.

WU, Billy et al. Battery digital twins: Perspectives on the fusion of models, data and artificial intelligence for smart battery management systems. **Energy and AI**, Elsevier, v. 1, p. 10–16, 2020.

XU, Meng et al. A pseudo three-dimensional electrochemical–thermal model of a prismatic LiFePO4 battery during discharge process. **Energy**, Elsevier, v. 80, p. 303–317, 2015.

YANAMANDRA, Kaushik et al. Recycling of Li-ion and lead acid batteries: a review. **Journal of the Indian Institute of Science**, Springer, v. 102, n. 1, p. 281–295, 2022.

YANG, Xiao-Guang et al. Modeling of lithium plating induced aging of lithium-ion batteries: Transition from linear to nonlinear aging. **Journal of Power Sources**, Elsevier, v. 360, p. 28–40, 2017.

ZHANG, Qi; WHITE, Ralph E. Comparison of approximate solution methods for the solid phase diffusion equation in a porous electrode model. **Journal of power sources**, Elsevier, v. 165, n. 2, p. 880–886, 2007.

ZHANG, Xiongwen. Thermal analysis of a cylindrical lithium-ion battery. **Electrochimica Acta**, Elsevier, v. 56, n. 3, p. 1246–1255, 2011.

ZHOU, Yuliang Leon. **Modeling and simulation of hybrid electric vehicles**. [S.l.: s.n.], 2007.

ZHU, Juner et al. End-of-life or second-life options for retired electric vehicle batteries. **Cell Reports Physical Science**, Elsevier, v. 2, n. 8, 2021.

APPENDIX A − PyBaMM

Demonstrations and Examples

This section includes examples which demonstrate some of the PyBaMM functionalities which are relevant for this project. Listings A.1 through A.3 include snippets of executable code which can be used to replicate each example.

A.1   Basic PyBaMM modelling

In the first example experiment, shown in Listing A.1, a simple battery model is created and solved. In the first section of this code (lines 5 to 20), the model parameters are selected. The `model_options` dict is used to describe the mathematical model options. In this example; the 'quartic profile' setting in the 'particle' field causes the model to approximate electrode lithium concentration distribution using a polynomial – as per (3.8) (SUBRAMANIAN; DIWAKAR; TAPRIYAL, 2005) – as opposed to using the full 'Fickian' concentration distribution model – as per (DFN.4) and (3.6). Additionally, the 'SEI' and 'SEI porosity change' options indicates which of multiple equations which describe SEI growth to use and whether or not to account for change in porosity over time. For a full list of model options, see the 'Base Battery Model' page in the PyBaMM documentation (PYBAMM, T., 2024b). The 'nodes_opt' variable (line 12) is a dictionary object which determines the number of nodes each section of the battery is to be divided by once the model is discretized. The values for 'x_n', 'x_s' and 'x_p' represent the negative electrode, the separator, and the positive electrode regions; respectively; and the 'r_n' and 'r_p' represent the number of nodes in the negative and positive solid-phases. The command 'ParameterValues' (line 15) loads one of the pre-included parameter sets that are bundled with PyBaMM. In this case, the 'OKane2022' parameter set comes from (O'KANE et al., 2022); line 16 demonstrates one of the OKane2022 parameters values being manually changed – this is done for illustrative purposes. Finally, lines 18 and 19 specify the settings for the CasADi solver, including solving model ('safe' as opposed to 'fast'), relative tolerance and maximum time-step. Of note, properly tuning these solver settings is a way to significantly improve simulation times (LI; O'KANE, et al., 2024).

```
1  import pybamm
2
3  ## PREPARE MODEL ===
4  # Options ---
5  model_options = {
6      "particle": "quartic profile",
7      "thermal": "isothermal",
8      "SEI": "solvent-diffusion limited",
9      "SEI porosity change": "true",
10 }
11 # Discretization ---
12 nodes_opt = {"x_n": 20, "x_p": 20, "x_s": 10,
13              "r_n": 30, "r_p": 30}
14 # Set parameters ---
15 param = pybamm.ParameterValues("OKane2022")
16 param["Outer SEI solvent diffusivity [m2.s-1]"] = 2.5e-19
17 # Solver ---
18 cas_solver = pybamm.CasadiSolver(mode="safe", rtol=1e-5, dt_max=10,
19                                  return_solution_if_failed_early=True)
20
21 ## BUILD AND SOLVE MODEL ===
22 model = pybamm.lithium_ion.DFN(model_options)
23 sim = pybamm.Simulation(model, parameter_values=param,
24                                 var_pts=nodes_opt,
25                                 solver=cas_solver,
26                                 C_rate=1.5)
27 sol = sim.solve(t_eval=[0, 3600], initial_soc=0.95)
```

Listing A.1: PyBaMM Python code which sets up and runs a simple model.

Following the model preparation step, the second portion of the code – between lines 22 and 27 – actually builds and solves the model. The 'lithium_ion.DFN' command sets up the symbolic representation of a DFN model based off the model options input dict. The 'Simulation' command assigns the parameter values, solver options, and discretization instructions to the model. Finally, the 'sim.solve' command initializes the battery model and simulates it for a given period ('t_eval') or until it the model reaches a termination point (ie. voltage reaches a pre-established minimum). The resulting 'sol' object is a 'pybamm.Solution' instance that contains simulation data which can then be plotted, exported, or be used as the initial condition for another PyBaMM simulation.

Figure A.1 shows the evolution of two of cell outputs: voltage overtime (as a function of throughput capacity [Ah]) and the internal lithium electrolyte concentration [mol/m^3] over the course of the first three minutes. These are only two of the many simulation variables which can be plotted and exported, for a full list of the information that the model collects, see Tutorial 3 among the examples in the PyBaMM documentation (PYBAMM, T., 2024b).

Figure A.2 compares the voltage profile as a function of discharge capacity for different C-rates and models. The first image shows the voltage profile for a DFN model with Fickian diffusion for different values of C-rate. Second image shows the voltage profile for different models given a discharge current of 1.5 C-rate.
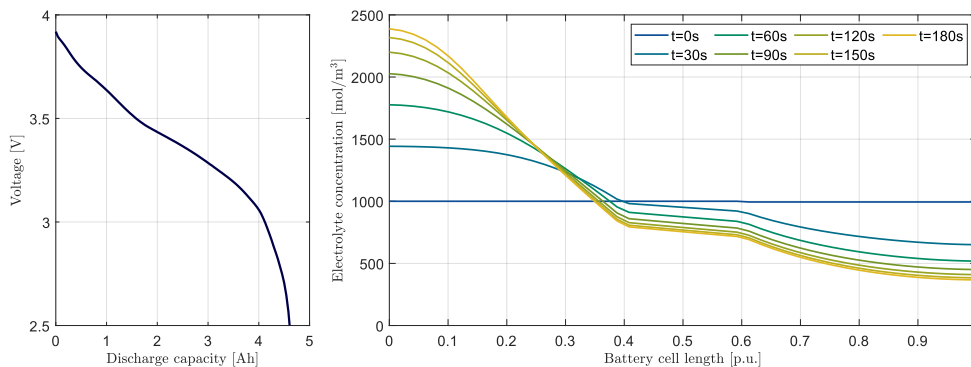

Figure A.1 – PyBaMM simulation output from code in Listing A.1. Voltage profile curve over discharge capacity and electrolyte lithium distribution overtime.
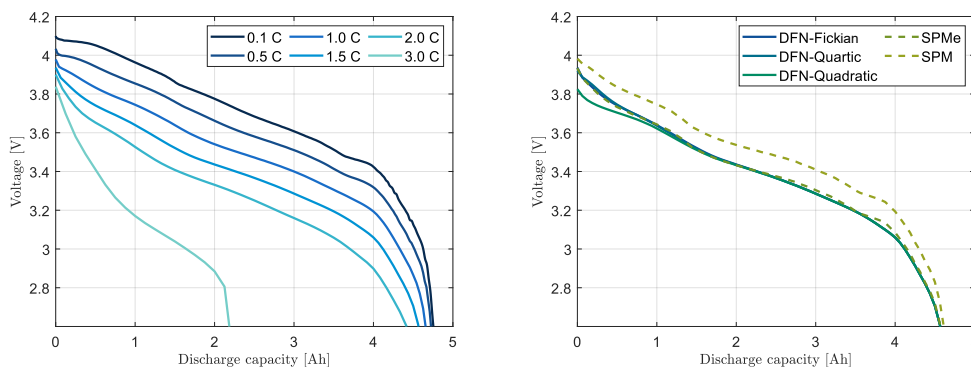
Figure A.2 – Comparison between PyBaMM simulation outputs. Comparison between different C-rates given DFN with Fickian diffusion model. Comparison between different models given 1.5 C-rate discharge.

A.2 Current and Temperature Drive-Cycles

Using the 'pybamm.Experiment' command, it is possible to construct more elaborate simulations. See Tutorial 5 in the Examples page of the PyBaMM documentation for a step by step guide in setting up multi-cycle constant charge and discharge simulation experiments (PYBAMM, T., 2024b). For the purposes of simulating electric vehicle drive-cycles, however, simpler constant charge and discharge cycling routines are insufficient. Listing A.2 shows an example were an arbitrary current and temperature profile are loaded from two csv files and used as inputs in a simulation.

```python
1  import pybamm
2  import numpy as np
3  import pandas as pd
4
5  # Solver and model options
6  cas_solver = pybamm.CasadiSolver("safe", rtol=1e-5, dt_max=10,
7              return_solution_if_failed_early=True)
8  model_options = {"particle": "quartic profile", "thermal": "isothermal",
9                   "SEI":"solvent-diffusion limited", "SEI porosity change":"
       true",}
10
11 # Load data and set-up current and temperature drive cycle
12 def temperature_function(y,z,t):
13     T_cycle = pd.read_csv("temperature_cycle.csv",header=None).to_numpy()
14     return pybamm.Interpolant(T_cycle[:,0], T_cycle[:,1], t)
15 drive_cycle = np.column_stack( pd.read_csv("drive_cycle.csv",
16                                    header=None).to_numpy().transpose() )
17
18 exp = pybamm.Experiment([pybamm.step.current(drive_cycle, termination="2.5
       V")])
19 param = pybamm.ParameterValues("OKane2022")
20 param["Ambient temperature [K]"] = temperature_function
21
22 # Build and solve model
23 model = pybamm.lithium_ion.DFN(model_options)
24 sim = pybamm.Simulation(model, parameter_values=param,
25                     experiment=exp, solver=cas_solver)
26 sol = sim.solve()
```

Listing A.2: PyBaMM code that loads and runs a custom current and temperature drive-cycle from a csv file.

In the Listing A.2 example, current and temperature data are loaded from csv files 'drive_cycle.csv' and 'temperature_cycle.csv', respectively. Both of these files are made up of two columns with no header: the first lists the time in seconds, the second lists the values of current in Ampère or temperature in Kelvin. Table A.1 shows an abridged section of both of these csv tables.

The current data is saved as a 'numpy.column_stack' object (line 15), this is then used to characterize a 'pybamm.Experiment' object (line 18) which determines the current behaviour for the simulation (line 24). Note that in this case the 'sim.solve' command doesn't require the 't_eval' (line 26) time interval variable to be explicitly declared, this is because the simulation object has been assigned a 'experiment' variable which comes to determine the simulation length and time-step.

The temperature data is encoded within a function as a 'pybamm.Interpolant' object (lines 12 to 14). During the parametrization stage, this function is directly assigned to the

relevant parameter variable – 'ambient temperature' in this case (line 20).

Table A.1 – Formatting of the current and temperature profiles csv tables, as used in code in Listing A.2. Values are merely illustrative.

`drive_cycle.csv`		`temperature_cycle.csv`	
0	0.0	0	300.00
1	5.0	5	303.75
2	-1.2	10	304.34
3	-2.4	15	306.00
4	3.1	20	305.80
5	4.2	25	305.95
...	...	...	...

In the example of Table A.1, the time-step for the current and temperature values are different. Here, the current drive cycle determines the solution time-step and the temperature is interpolated linearly to determine the values for the 'in-between' timestamps (hence '`Interpolant`'). This interpolation is done relative to the simulation objects internal timer value, this means that if the simulation outlasts the temperature timeline it results in critical errors. To ensure this doesn't happen, the temperature profile must be sufficiently long or the simulation timer must be reset at regular intervals. This second approach is briefly discussed in the Example of Section A.3.

A.3   Saving and Loading Battery Values

Lastly, Listing A.3 shows how to save and load PyBaMM battery data to file. This allows one to save "copies" of the battery at different stages of degradation. This is particularly useful to have in long-term degradation simulations. Also useful for debugging and restarting a long simulation in the case where it crashes or some kind of other error occurs. Unlike the two other examples, there is no specific page in the PyBaMM documentation that explains this practise, as it is not an official functionality.

After a PyBaMM simulation ('`sim.solve`' command in line 14), an instance of the '`Solution`' class is created within the '`Simulation`' class instance – in this case these are the '`sim.solution`' and '`sim`' variables respectively. The '`Solutions`' class contains attributes associated with the PyBaMM model along with the values of the simulation solution within internal variable '`all_ys`', accessed through the function '`solution.y.full()`'. This command returns a two dimensional array of size (m,n) where m is the number of values

```python
{python}
import os
import pybamm
import numpy as np
from scipy import io

def pybamm_model_values():
    op = {"particle": "quartic profile",
          "SEI": "solvent-diffusion limited",
          "SEI porosity change": "true", }
    return [pybamm.lithium_ion.DFN(op), pybamm.ParameterValues("OKane2022")
    ]

[model, param] = pybamm_model_values()
sim = pybamm.Simulation(model, parameter_values=param, C_rate=.75)
sim.solve(t_eval=[0, 1800])

# Save y0
y0 = sim.solution.last_state.y.full()[:, 0]
folder = os.getcwd()
io.savemat(os.path.join(folder, "y_0.mat"), {"y0": y0})

# Load y0
y_new = io.loadmat("y_0.mat")["y0"]
if np.shape(y_new)[1] > np.shape(y_new)[0]: y_new = y_new.transpose()

# Make new model
[new_model, new_param] = pybamm_model_values()
temp_sim = pybamm.Simulation(new_model, parameter_values=new_param)
temp_sim.solve([0, 1e-6]) # dummy solve (initialize model)
temp_solution = pybamm.Solution(all_ts=np.array([0,0]*2),
                                all_ys=y_new, all_inputs={},
                                all_models=temp_sim.solution.last_state.
    all_models)

newest_model = new_model.set_initial_conditions_from(temp_solution.
    last_state,
                                                     inplace=False)
new_sim = pybamm.Simulation(newest_model,parameter_values=new_param,C_rate
    =.75)
new_sim.solve(t_eval=[0, 1800])
```

Listing A.3: PyBaMM code that runs a model, saves the solution to file, then loads it later to continue the simulation.

needed to fully describe the battery model at any given moment and n is the number of time-steps in the preceding simulation. Though the values in this array do relate back to relevant physical properties of the battery, in this form the values are unlabelled and illegible for the end-user. For visualization purposes, the functionalities of the Solution class should be used instead. The value of m depends a lot on the type of model used, the sub-models included, the number of discretization nodes and other such model options demonstrated in Listing A.1; generally, the more complex the model, the more values are needed to describe it, the larger the m. Because

PyBaMM only needs the most recent solution values in order to calculate the next time-step, only the final column of 'y' values is needed; as such, 'solution.last_state.y' is used to ensure a size (m,1) solution vector (line 17).

The models internal variables can be saved to be loaded later; a '.mat' format is used but other formats such as '.csv' are also valid. The 'y' vector is a simple array of numerical values after all. After that, a new instance of the PyBaMM 'model' object is created (line 26); because the length of array 'y' (m) depends on model options, it is vital that this model be equal to the one which created vector 'y'. To ensure the consistency of the model throughout the execution of the code, a callable function is used (lines 6 to 10). A short 'dummy' simulation is done, simply to initialize the model (lines 27 and 28) and then an 'artificial' solution instance (initialized outside of a simulation) is created using the initialized model from the dummy simulation and the 'y' variable loaded from file as the input (lines 29 to 31). This command additionally resets the internal timer of simulation object ('all_ts'), which is important to ensure that the temperature interpolant timer (discussed in Section A.2) does not 'overflow' and crash the simulation.

Figure A.3 shows the cell output voltage and open-circuit voltage for both the simulations from the code in Listing A.3. Here, the continuity between both models results is noticeable.
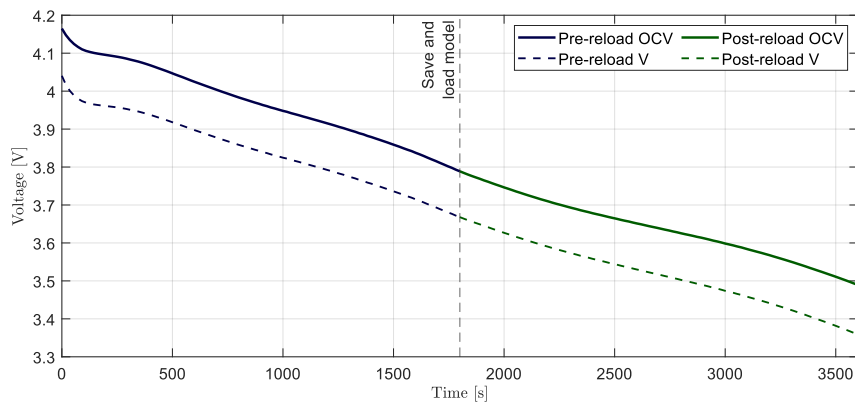

Figure A.3 – Comparison of battery cell output voltage and open-circuit voltage before and after saving and loading the PyBaMM model.

APPENDIX B − Battery CasADi Model Simulink Block

The code in Listing B.1 shows the Python code which extracts and saves the CasADi functions to file. This code is adapted from (TRANTER, 2021), with some changes to account for the updated version of PyBaMM. The CasADi objects are saved as two files, each one represents a specific function. The integrator function (lines 17 to 23) updates the internal state of the model (as represented by internal variable y, previously discussed in Section A.3) by solving the system of equations over a time-step dt. The output function (lines 26 to 44) translates the unsorted battery internal state vector (y) into pre-selected output variables. Both the integrator (F_{INT}) and the output (F_{OUT}) functions depend on the battery internal state (y) and input (u) for a given moment n – as shown in (B.1) and (B.2) – and are executed once per time-step.

$$y_n = F_{INT}(y_{n-1}, u_n) \tag{B.1}$$

$$o_n = F_{OUT}(y_n, u_n) \tag{B.2}$$

Now, on the MATLAB/Simulink side, Listing B.2 shows an abridged version of the code which sets up the CasADi battery Simulink block. On start up (lines 10 to 18), the relevant information is loaded from file; this includes the internal variables vectors ('y') – discussed in Section A.3 – and the two CasADi functions. In MATLAB, the internal y vector is divided in two component sub-vectors 'x' and 'z'. This distinction has to do with the implementation of CasADI code; basically, vector 'x' contains values which vary over time in accordance to differential equations and 'z' contains the variables which depend on algebraic equations (ANDERSSON; GILLIS, et al., 2019). The length of 'x' and 'z' vectors depends on PyBaMM model characteristics; the more complex the model, the bigger the vector needs to be. Then, during each simulation time-step, the function '`stepImpl`' (lines 20 to 30) runs both the CasADi functions and parses the output.

Finally, heat is calculated as a function of measured voltage, open-circuit voltage, and current in line 31 from Listing B.2. This implementation of the heat equation is in accordance to the thermal modeled in (3.20) (PRADA, 2012).

```python
1  import pybamm
2  import numpy as np
3
4  def pybamm_model_values():
5      # Returns relevant model variables
6      # Function hidden for sake of brevity
7      return [dfn_model, okane_param, casadi_solver]
8
9  [model, param, solver] = pybamm_model_values()
10 battery_inputs = {"Power function [W]": 0, "Ambient temperature [K]": 300}
11 sim = pybamm.Simulation(model, parameter_values=param, solver=casadi_solver
      )
12
13 # Dummy solve
14 sim.solve(t_eval=[0, 1], initial_soc=0.95, inputs=battery_inputs)
15
16 # Create CasADi INTEGRATOR
17 dt = 0.5   # Time-step size (in seconds)
18 t_eval_integrator = np.linspace(1, dt, 3)
19 casadi_integrator = casadi_solver.create_integrator(sim.built_model,
20                                                      inputs=battery_inputs,
21                                                      t_eval=
      t_eval_integrator)
22
23 casadi_integrator.save("integrator.casadi") # Save to file
24
25 # Create CasADi OUTPUT_VAR
26 model_ins = ["Power function [W]", "Ambient temperature [K]"]
27 model_out = ['Terminal voltage [V]',
28              'Surface open-circuit voltage [V]',
29              'Current [A]',
30              'X-averaged negative particle surface concentration [mol.m-3]'
      ,
31              'Loss of capacity to negative SEI [A.h]',
32              'Loss of capacity to negative lithium plating [A.h]',
33              'Negative electrode porosity']
34
35 casadi_outs = sim.built_model.export_casadi_objects(variable_names=
      model_out,
36                                                     input_parameter_order=
      model_ins)
37
38 variables = casadi_outs['variables']
39 t, x = casadi_outs["t"], casadi_outs["x"]
40 z, p = casadi_outs["z"], casadi_outs["inputs"]
41 variables_stacked = casadi.vertcat(*variables.values())
42 variables_fn = casadi.Function("variables", [t, x, z, p], [
      variables_stacked])
43
44 variables_fn.save("outputs.casadi") # Save to file
```

Listing B.1: PyBaMM code that creates and exports two CasADi functions. `Integrator` simulates the battery over a time-step, `Outputs` returns specific values for a given state (TRANTER, 2021).

```matlab
1  classdef casadi_battery < matlab.System & matlab.system.mixin.Propagates
2      properties(Access = private)
3          x0
4          z0
5          f_int
6          f_out
7      end
8
9      methods(Access = protected)
10         function setupImpl(obj)
11             temp = load('y0.mat'); nlim_y = 240;
12             obj.x0 = temp.y0(1 : nlim_y);
13             obj.z0 = temp.y0(nlim_y+1 : end);
14
15             import casadi
16             obj.f_int = casadi.Function.load('integrator.casadi');
17             obj.f_out = casadi.Function.load('outputs.casadi');
18         end
19
20         function [volt, ocv, curr, heat] = stepImpl(obj, power, temperature
    )
21             t_min = 1e-3;
22             inputs = [power, temperature];
23             % integrator
24             [xt, zt] = obj.f(obj.x0, obj.z0, horzcar(inputs,t_min),0,0,0,0)
    ;
25             obj.x0 = xt(:, end); obj.z0 = zt(:, end);
26             % output variable
27             temp = double(full(obj.f_out(0, obj.x0, obj.z0, inputs)));
28             volt = temp(1);
29             ocv = temp(2);
30             curr = temp(3);
31             heat = (ocv - volt) * curr;
32              % It is possible to define an arbitrary number of outputs...
33         end
34     end
```

Listing B.2: Simplified version of MATLAB code which create PyBaMM battery simulink block.

Using the code in listing B.2, a Simulink CasADi battery block is created. This block can now be used alongside the rest of the vehicle model in Simulink. A simplified diagram of the full model, including battery cell model, is shown as a simplified diagram in Figure 4.6.